ATLAS CONF Note

ATLAS-CONF-2018-051

November 7, 2018

Constraints on mediator-based dark matter models using $\sqrt{s} = 13$ TeV pp collisions at the LHC with the ATLAS detector

The ATLAS Collaboration

Constraints on selected mediator-based dark matter models using $\sqrt{s} = 13$ TeV pp collisions collected by the ATLAS detector during the years 2015-2016 are summarised in this note. The results of experimental searches in a variety of final states are interpreted in terms of a set of spin-1 and spin-0 single-mediator dark matter simplified models and a second set of models involving an extended-Higgs sector plus an additional vector or pseudo-scalar mediator.

ATLAS-CONF-2018-051
07 November 2018

1 Introduction

The existence of a non-luminous component of matter is one of the major unknowns in our current understanding of the universe.

The existence of dark matter (DM) is supported by a variety of astrophysical measurements, ranging from the rotational speed of stars in galaxies, over precision measurements of the cosmic microwave background [1, 2], to gravitational lensing measurements [3–5]. However, the nature and properties of DM remain largely unknown. Searches for particle DM are performed using different complementary approaches: the measurement of elastic scattering of DM with nuclei and electrons in a detector [6–14], the detection of Standard Model (SM) particles produced in the annihilations or decays of DM in the universe [15–19], the production of DM particles at colliders [20–34], and the study of the effect of DM interactions on astrophysical systems [35, 36].

In this note we consider the hypothesis that the DM is composed of a weakly-interacting massive particle (WIMP) [37]. Under some parameter choices and assumptions, WIMPs can account for the relic density of non-relativistic matter in the early universe [38] measured in data from the Planck [2] and WMAP [1] Collaborations. For benchmarking purposes we will assume, for all models considered in this note, WIMPs to be Dirac fermions. For these models, WIMPs can only be pair-produced in the LHC pp collisions. These particles, denoted with the symbol χ throughout this note, are stable over cosmological scales and do not interact with the detector. To identify events with DM, additional particle(s), X = jet, γ, W, Z, h, $(t)\bar{t}$, $(b)\bar{b}$, need to be produced in association with DM in a pp collision, in order to tag the event and measure the recoiling WIMPs as missing transverse momentum (with magnitude $E_{\mathrm{T}}^{\mathrm{miss}}$). If the DM candidates can be produced at the LHC via an s-channel exchange of a new particle, then this mediator could also decay back into SM final states: resonance searches can therefore also be used to constrain DM models. The interplay of resonance and $X + E_{\mathrm{T}}^{\mathrm{miss}}$ searches depends on the specific model choice and will be further outlined in this note. In the models considered, some of which are new with respect to previous ATLAS publications, one or more new particles mediate the interaction of DM with the SM particles. The first category considers simplified models mediated by a vector, axial-vector, scalar or pseudo-scalar mediator. In the case of simplified vector and scalar mediators, different types of interactions are explored (baryon-charged and coloured interactions). The second category considers less simplified models involving an extended-Higgs sector plus an additional mediator, either a vector or a pseudo-scalar particle. The assumptions and choices of models considered follow closely the work of the DM Forum/LHC DM Working Group [39–42].

Theories such as R-parity conserving supersymmetry [43–46] can also provide a viable WIMP DM candidate. These models are searched for using a wide range of experimental signatures [47–54] performed by the ATLAS Collaboration and are not discussed further in this note.

Furthermore, analyses focusing on signatures compatible with (unstable) long-lived particles decaying into the detector volume are also not considered in this note [55].

This note aims to provide an overview of the experimental programme of searches for mediator-based DM models performed to date using 13 TeV proton-proton collisions data delivered in the years 2015 and 2016 by the Large Hadron Collider (LHC) [56] and collected by the ATLAS experiment [57]. The studies presented in this note use published data analyses. Since no significant excess over the expected SM background processes was found in any of these analyses, the results are used to constrain the phase space for DM models.

The note is structured as follows. The DM models considered in this note are highlighted in Sec. 2, while the data and simulation samples are described in Sec. 3. The data analyses for each different signature are briefly described in Sec. 4, where the complementarity of different final states is also discussed. Finally, the dominant systematic uncertainties affecting the modelling of the signal samples are highlighted in Sec. 5 and the final results are presented in Sec. 6, followed by the conclusions (Sec. 7).

2 Theoretical framework

All DM results presented in this note are interpreted in the framework of simplified DM models [39, 42, 58–61], where a new particle (or set of particles) mediates the interaction of DM with the SM particles. These DM simplified models, which overcome some of the shortcomings of previous EFT-based DM models [60, 62–66], can be classified according to content and properties of the particles that mediate the interaction between DM and SM particles (mediator sector), giving rise to collider signatures of different kinematic characteristics and topologies.

Two classes of models are considered: the case where the mediator sector is composed of a single particle, either of spin-1 (Sec. 2.1) or of spin-0 (Sec. 2.2) and the case where the mediator sector is composed of an extended-Higgs sector plus an additional mediator, either a spin-1 (Sec. 2.3.1) or spin-0 (Sec. 2.3.2) particle.

All models described in this section are summarised in Table 1. For all models, the width of the mediator is always assumed to be the minimal width that can be calculated from all other parameters. Furthermore we will assume dark matter to be a Dirac fermion[1].

2.1 Vector or axial-vector dark matter models

The first category of models considered in this note consists of a set of simplified models with a single spin-1 particle that acts as the mediator. This category of models that assumes the existence of new gauge symmetries is among the most commonly studied extensions of the SM [67] and provides a convenient framework to describe the interaction between the SM and dark matter. Two types of simplified models involving a single spin-1 particle are investigated: a neutral mediator [66, 68–74] and a baryon-number charged mediator [75–78].

2.1.1 Neutral interaction

One vector or axial-vector simplified model (V/AV) [39] consists of a simple extension of the SM with an additional U(1) gauge symmetry under which the DM particles are charged. The new mediator (Z') is either a vector (Z'_V) or an axial-vector (Z'_A) boson. The model has five parameters [39]: the masses of the mediator and the DM particle ($m_{Z'_{V/A}}$ and m_χ, respectively), the flavour universal coupling of the Z' boson to all flavour quarks, g_q, the coupling to all lepton flavours, g_l, and the coupling to DM, g_χ. Representative diagrams for this model are shown in Fig. 1. The Z' mediator can decay to either a pair of quarks, a pair

[1] The assumption that DM is a Majorana fermion changes the set of allowed interactions, but also the total cross-section for the ones that are allowed. Aside from these, adjusting the choice of Dirac fermions, Majorana fermions, or scalars is expected to produce minor changes in the kinematic distributions of the visible particles in the final state. However, these assumptions have not been considered further in terms of simplified DM models [39]

Short description	Acronym	Symbol	JCP	Charge	Signatures	Results
Vector/axial-vector mediator	V/AV	Z'_V/Z'_A	$1^{\pm}$	-	jet/$\gamma/W/Z$+$E_{\mathrm{T}}^{\mathrm{miss}}$, di-fermion resonance	Sec.6.1.1
Vector baryon-charged mediator	VBC	Z'_B	1^+	baryon-number	$h + E_{\mathrm{T}}^{\mathrm{miss}}$	Sec.6.1.2
Scalar/pseudo-scalar mediator	S/PS	ϕ/a	$0^{\pm}$	-	jet+$E_{\mathrm{T}}^{\mathrm{miss}}$, $t\bar{t}/b\bar{b}$+$E_{\mathrm{T}}^{\mathrm{miss}}$	Sec.6.2.1
Scalar colour-charged mediator	SCC$_{q/b}$	$\eta_{q/b}$	0^+	colour, 2/3 electric-charge	jet+$E_{\mathrm{T}}^{\mathrm{miss}}$, $b + E_{\mathrm{T}}^{\mathrm{miss}}$	Sec.6.2.2
Two-Higgs-doublet plus vector mediator	2HDM+Z'_V	Z'_V	1^+	-	$h + E_{\mathrm{T}}^{\mathrm{miss}}$	Sec.6.3.1
Two-Higgs-doublet plus pseudo-scalar mediator	2HDM+a	a	0^-	-	$W/Z/h + E_{\mathrm{T}}^{\mathrm{miss}}$, $t\bar{t}/b\bar{b}$+$E_{\mathrm{T}}^{\mathrm{miss}}$, h(inv), $t\bar{t}t\bar{t}$	Sec.6.3.2

Table 1: Summary of the mediator-based simplified models considered in this note, along with the associated model acronym (2$^{\mathrm{nd}}$ column) and mediator symbol (3$^{\mathrm{rd}}$ column) used throughout. The 4$^{\mathrm{th}}$ and 5$^{\mathrm{th}}$ columns indicate the quantum numbers of the mediator, the 6$^{\mathrm{th}}$ column the final state signatures considered, and the 7th column gives the reference to the interpretation.

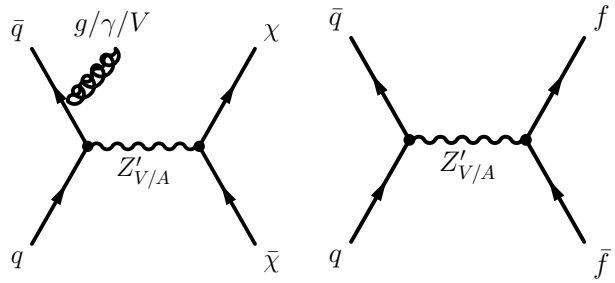

Figure 1: Schematic representation of the dominant production and decay modes for the V/AV model.

of leptons or a pair of DM particles. In the latter case, an additional visible object has to be produced in association with the mediator as initial state radiation (ISR), as shown in Fig. 1(a). The visible object can either be a jet, a photon or a W or Z boson. In order to highlight the complementarity of dedicated searches based on different final states [41], two coupling scenarios are considered for the interpretation of these models: the case of a leptophobic and the case of a leptophilic Z' mediator (see Sec. 6.1.1).

2.1.2 Baryon-charged interaction

The baryon-charged mediator simplified model [39, 78] (VBC) considers a vector mediator as in the V/AV model and additionally assumes that the charge of the U(1) symmetry coincides with the baryon number and it is spontaneously broken by a baryonic Higgs scalar. The DM candidate in this model is a stable

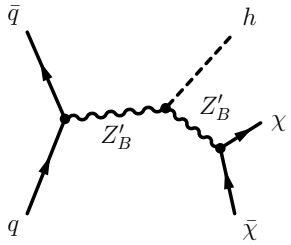

Figure 2: Schematic representation of the dominant production and decay modes for the VBC model.

baryonic state and it is neutral under the SM gauge symmetry. While the model can provide an ISR signature through a s-channel Z'_B-mediator production subsequently decaying into a pair of DM candidates as for the V/AV models described in the previous section (Fig. 1(a)), it can also display a distinctive $h + E_{\mathrm{T}}^{\mathrm{miss}}$ signature [78], as shown in Fig. 2. The model has 5 parameters [78], whose values are chosen to enhance the cross-section for $h + E_{\mathrm{T}}^{\mathrm{miss}}$ final states with respect to traditional ISR signatures. The mixing angle between the baryonic and the SM Higgs bosons, θ, is fixed to $\sin\theta = 0.3$ in order to comply with the Higgs boson coupling measurements. The coupling of the mediator Z'_B with the quarks, g_q, and the DM, g_χ, are set to $1/3$ and 1, respectively. The coupling of the mediator with the Higgs boson, $g_{Z'_B}$ is set to the ratio of the mediator mass to the vacuum-expectation-value (VEV) of the baryonic Higgs boson: $m_{Z'_B}/v_B$. The mediator is naturally leptophobic, thus evading the constraints coming from the dilepton resonance searches. Different mediator and DM masses are investigated.

2.2 Scalar or pseudo-scalar dark matter models

The second category of models considered in this note consists of a set of simplified models with a single spin-0 particle that composes the mediator sector. In simplified models the mediator couples to SM fermions proportionally to the Higgs Yukawa couplings. These models can therefore be easily included in the extended Higgs sectors of numerous ultraviolet (UV) complete theories. The various models considered can be grouped in two broad categories: colour-neutral [79–87] or colour-charged mediators [88–105]. The latter case is divided into three further models, which are specific realisations of colour-charged mediator models with different final states.

2.2.1 Colour-neutral interaction

In the scalar or pseudo-scalar simplified model (S/PS) a new spin-0 gauge singlet mediates the interaction, at tree level, with a singlet DM particle [39, 81]. The mediator is considered to be either a scalar (ϕ) or a pseudo-scalar (a). This model has four parameters [25]: the mass of the mediator m_ϕ or m_a, the DM mass, the DM-mediator coupling, g_χ, and the coupling of the mediator with the SM fermions. The latter is composed of a flavour universal term, g_q, which is a free parameter of the model that multiplies the SM-Yukawa coupling for each of the fermions [81]. This particular form of interaction, common to all models with spin-0 mediators considered in this note, is typically referred to as minimal flavour violation (MFV) ansatz and by construction relaxes the severe restrictions imposed on the coupling of new spin-0 colour-neutral particles to the SM-fermions imposed by precision flavour measurements [106–108]. Furthermore, it implies that these mediators are sizeably produced through loop-induced gluon fusion or in association with heavy-flavour quarks (see Fig. 3). According to whether the mediator decays into a pair of

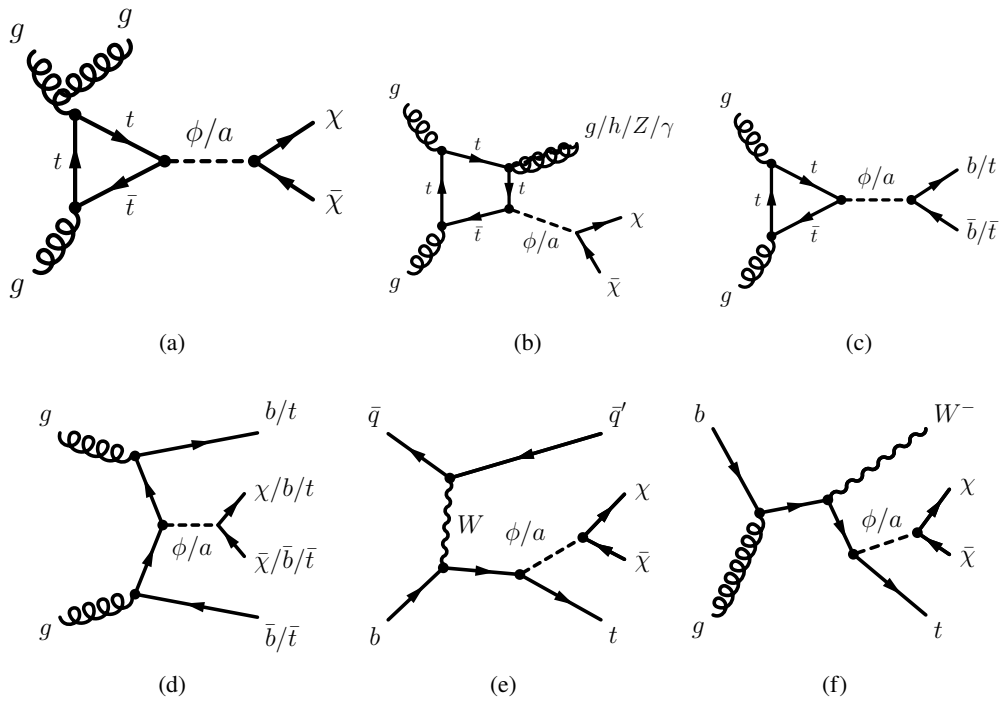

Figure 3: Schematic representation of the dominant production and decay modes for the S/PS model.

DM or SM particles, different final states are sensitive to these models. Due to the Yukawa-like structure of the couplings, visible final states with two or four top-quarks are particularly important signatures. Final states involving a single top quark and $E_{\mathrm{T}}^{\mathrm{miss}}$ may also play an important role to constrain these models [109–112]. Despite the absence of a dedicated parameter that regulates the relative importance of up-type and down-type quark couplings (otherwise present in UV completions of these models as in Sec. 2.3.2), it is also important to study final states involving bottom-quarks separately, which become a relevant signature if the up-type couplings are suppressed.

2.2.2 Colour-charged interaction

The colour-charged interaction model (SCC) assumes that the mediator couples to left or right-handed quarks, and it is a colour triplet. The DM is produced via a t-channel exchange of this mediator which leads to a different phenomenology with respect to colour-neutral interactions. These models have a strong connection with the minimal supersymmetric Standard Model (MSSM) [113, 114] with a neutralino DM and first and second generation squarks with universal masses, and share with it the same cross-sections and phenomenology when the mediator is pair produced via strong interaction. Nevertheless, additional production diagrams are considered in this scenario, due to the different values assumed for the couplings of the mediator to quarks and DM with respect to the MSSM.

As in the case of the MSSM, it is reasonable to decouple the first two generations from the third, considering the different mass scales. To this aim, two different models are considered[2]:

[2] These two scenarios provide benchmarks for each signature considered and do not aim to be representative of models involving colour-charged interactions.

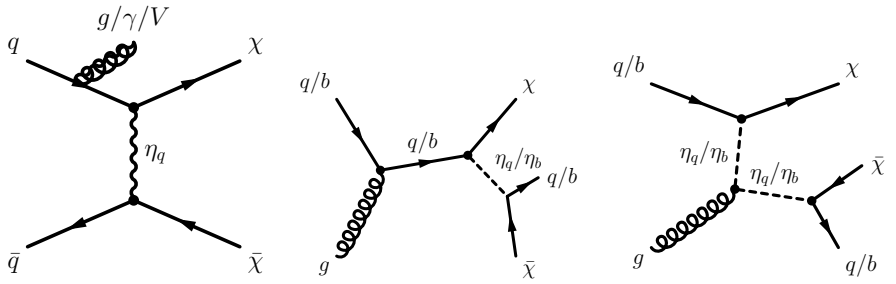

(a) (b) (c)

Figure 4: Schematic representation of the dominant production and decay modes for the SCC models.

1. In the SCC$_q$ model, the mediator, η_q, couples to the left-handed quarks of the first and second generation and is a SU(2) singlet under the SM. The mediator decays into a quark-DM pair, so that the strongest sensitivity for these models are provided by searches involving jets and missing transverse momentum. The three model parameters are the mediator mass, the DM mass and the flavour universal coupling to quarks and DM: λ_q. This model is described in detail in Refs. [26, 73] and representative diagrams are shown in Figs. 4(a), 4(b) and 4(c).

2. In the SCC$_b$ model, the mediator, η_b, couples to the right-handed bottom quark. Following previous publications [25, 115], the specific realisation of this model is obtained under the framework of "flavoured" DM, where the DM candidate is the lightest component of a flavour triplet [101]. Under these assumptions, the mediator always decays into a b-quark-DM pair. Of the three parameters of the model, the mediator and DM masses and the coupling, λ_b, only the first two are varied, while the last one is set to the value predicting a DM relic density compatible with astrophysical observations [106]. Representative diagrams for this models are presented in Figs. 4(b) and 4(c).

2.3 Extended Higgs sector dark matter models

The third category of models aims to extend the simplified DM mediator models by involving an extended two-Higgs-doublet sector (2HDM) [116–124], together with an additional mediator to DM, either a vector or a pseudo-scalar. This embeds the simplified models in a UV complete and renormalisable framework and allows the investigation of a broad phenomenology predicted by this type of models. In both models, the 2HDM sector has a CP-conserving potential and a softly broken $\mathbb{Z}_2$ symmetry [125], and the alignment limit is assumed, such that the lightest CP-even state, h, of the Higgs sector can be identified with the SM Higgs boson.

2.3.1 Two-Higgs-doublet models with a vector mediator

The first two-Higgs-doublet model [126], denoted for brevity 2HDM+Z'_V in the following, is based on a type-II 2HDM [125, 127] with an additional U(1) gauge symmetry, which gives rise to a new massive Z'_V gauge boson state. The Z'_V boson, which can mix with the Z boson, couples only to right-handed quarks and only to the Higgs doublet that couples to the up-type fermions. The CP-odd scalar mass eigenstate from the extended Higgs sector couples to DM particles and complies with electroweak precision measurement constraints. The phenomenology of this model is extended with respect to the simplified case due to

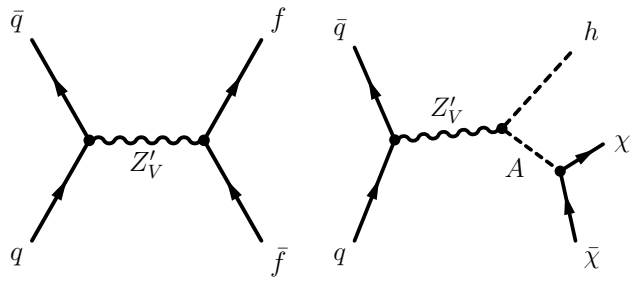

Figure 5: Schematic representation of the dominant production and decay modes for the 2HDM+Z'_V model.

the presence of a new decay mode $Z'_V \to hA$, as shown in Fig. 5, with A decaying into a pair of DM particles with a large branching ratio (when kinematically possible), as long as the decay into a pair of top-quarks is kinematically forbidden [31]. Additional signatures involving decays of the Z'_V boson into SM particles or the H and $H^\pm$ bosons are possible in the model. However, the model parameters are chosen to mitigate the impact of the constraints from resonance searches of heavy bosons on this model [128], and therefore these signatures are not considered further in the context of this interpretation. This model has 6 parameters [128]: $\tan\beta$, the ratio of the vacuum expectation values of the two Higgs doublets, is set to unity, m_χ, the DM mass, set to 100 GeV and g_Z, the couplings of the new Z'_V U(1) gauge symmetry, set to 0.8. The masses m_h and $m_H = m_{H^\pm}$ of the two CP-even and charged Higgs bosons are set to 125 GeV, and 300 GeV, respectively, while m_A, the mass of the CP-odd Higgs partner and $m_{Z'_V}$ are free parameters varied in the interpretation.

2.3.2 Two-Higgs-doublet models with a pseudo-scalar mediator

The second 2HDM model [120], 2HDM+a, includes an additional pseudo-scalar mediator, a. Also in this case, the 2HDM coupling structure is chosen to be of type-II, although many of the interpretations considered in this note hold for a type-I case too. The additional pseudo-scalar mediator of the model couples the DM particles to the SM and mixes with the pseudo-scalar partner of the SM Higgs boson. The physics of the model is fully captured by 14 parameters: the masses of the CP-even (h and H), CP-odd (a and A) and charged bosons ($H^\pm$), the mass of the DM particle (m_χ), the three quartic couplings between the scalar doublets and the a boson (λ_{P1}, λ_{P2} and λ_3) and the coupling between the a boson and the DM, y_χ, the electroweak VEV, v, the ratio of the VEVs of the two Higgs doublets, $\tan\beta$, and the mixing angles of the CP-even and CP-odd weak eigenstates, denoted α and θ, respectively. The alignment and decoupling limit ($\cos(\beta-\alpha) = 0$) is assumed, thus h is the SM Higgs boson and $v = 246$ GeV. The quartic coupling $\lambda_3 = 3$ is chosen to ensure the stability of the Higgs potential for our choice of the masses of the heavy Higgs bosons which are themselves fixed to equal values ($m_A = m_{H^\pm} = m_H$) to simplify the phenomenology and evade the constraints from electroweak precision measurements [120]. The other quartic couplings are chosen accordingly in order to maximise the trilinear couplings between the CP-odd and the CP-even neutral states, and are also set to 3. Finally, $y_\chi = 1$ is chosen, having a negligible effect on the kinematics in the final states of interest.

This model is characterised by a rich phenomenology. The production of the lightest pseudo-scalar is dominated by loop-induced gluon fusion, followed by associated production with heavy-flavour quarks or associated production with a Higgs or Z-boson (Fig. 3). Furthermore, according to the Higgs sector mass

hierarchy, Higgs and Z-bosons can be produced in the resonant decay of the heavier bosons into the lightest pseudo-scalar (Fig. 6). The pseudo-scalar mediator can subsequently decay either into a pair of DM or SM particles (dominantly top-quarks if kinematically allowed), giving rise to very different characteristic signatures. The four-top signature is particularly interesting in this model if the neutral Higgs partner masses are kept above the $t\bar{t}$ decay threshold, since, when kinematically allowed, all four neutral bosons can contribute to this final state, as depicted in the diagram of Fig. 6(c). Four benchmark scenarios [42] that are consistent with bounds from electroweak precision, flavour and Higgs observables are chosen to investigate the sensitivity to this model as a function of relevant parameters: m_a, m_A, $\tan\beta$, $\sin\theta$ and m_χ.

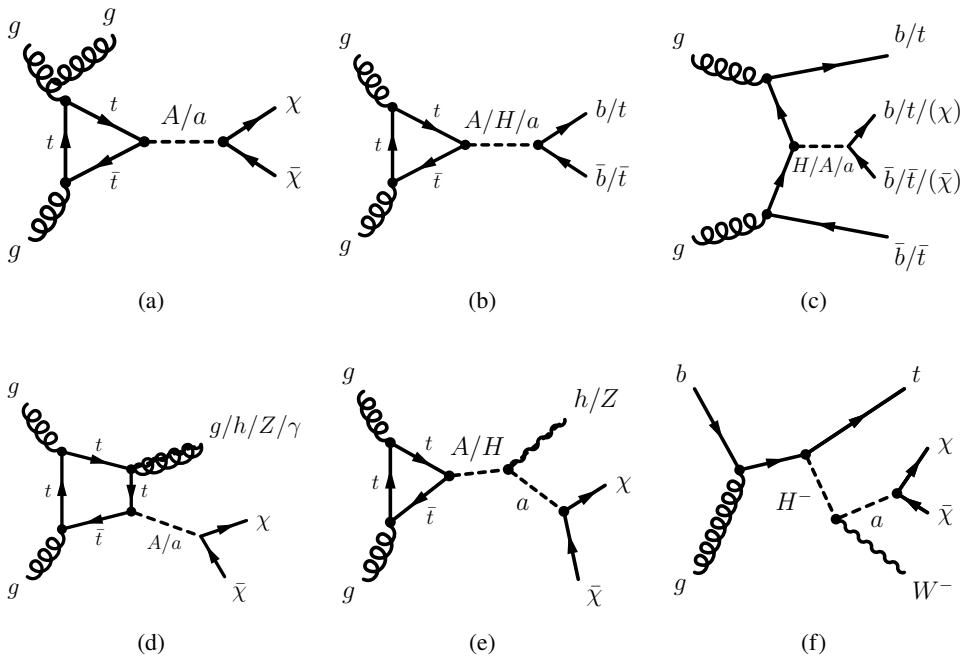

Figure 6: Schematic representation of the dominant production and decay modes for the 2HDM+a model.

3 Signal simulation and dataset

The dataset used in the analyses considered in this note consists of pp collision data recorded at a centre-of-mass energy of $\sqrt{s}$ = 13 TeV. The total integrated luminosity of the combined 2015 and 2016 dataset, after requiring that all detector subsystems were operational during data recording, is 36.1 fb^{-1}, unless otherwise specified for a given analysis. The uncertainty in the combined 2015 and 2016 integrated luminosity is 2.1%. It is derived, following a methodology similar to that detailed in Ref. [129], from a calibration of the luminosity scale using x-y beam-separation scans performed in August 2015 and May 2016.

Monte Carlo (MC) simulated event samples are used to aid in the estimation of the background from SM processes and to model the DM signals. Simulated events were processed either through an ATLAS detector simulation [130] based on Geant4 [131] or through a fast simulation [130] with a parameterisation of the calorimeter response and Geant4 for the other parts of the detector [132]. Either of these detector simulations are used for background processes (details in the specific analyses references) and some of the signal processes, as detailed in the following.

Two sets of samples are used for the modelling of the signal processes considered in this note. One set of samples is based on signal events processed through the ATLAS detector simulation, denoted as "reconstructed" samples. The second set of samples consists of signal events composed of particle-level objects, defined according to the guiding principles outlined in Ref. [133], and not including any resolution effect due to the ATLAS detector. These are denoted as "particle-level" samples. Particle-level samples are used to define a re-scaling procedure specifically designed to broaden the range of signal models and parameter choices considered in the interpretation of the results. This aims to provide a complete picture of the current experimental coverage for these models. This procedure also allows the reduction of the extensive computational resources which would be needed to provide a full detector simulation of the large set of considered signals. The re-scaling procedure consists of calculating a set of correction weights for a reference model as the ratio of the acceptance derived in a particle-level simulation for a baseline signal sample to the acceptance of the signal sample of interest, also derived in a particle-level simulation. These weights are then applied to the reconstructed baseline signal sample of the reference model, assuming similar detector effects for the two models. The same procedure is used in some cases to re-scale between signal samples of the same reference model but for different parameter choices which affect the kinematics of the final state. Closure-tests are used to determine the reliability of this procedure and assign specific re-scaling systematic uncertainties when needed. Further details about the re-scaling used in the V/AV and the 2HDM+a signal samples are found in Appendix A.

The generation setup for signal models considering a spin-1 mediator is summarised in Table 2. For each model the table indicates the Universal FeynRules Output (UFO) model [134] implementation, the matrix element (ME) generator, the parton shower (PS) and the cross-section normalisation, at QCD leading- or next-to-leading order accuracy (LO and NLO, respectively). Following the notation of the previous section, the simplified models are indicated with $Z'_{V/A}$, while the baryon-charged is indicated as Z'_B. The 2HDM model with additional vector mediator is indicated as 2HDM+Z'_V. When relevant for the generations settings, each separate final state considered in this note is indicated for each model.

The generation settings for signal models considering a spin-0 mediator are summarised in Table 3. Following the notation of the previous section, the colour-neutral (colour-charged) simplified models are indicated with ϕ/a (η). The 2HDM with additional pseudo-scalar mediator is indicated as 2HDM+a.

The model implementations, settings and parameter scans follow the prescriptions of the DM Forum/LHC DM Working Group [39–42].

4 Experimental signatures

Dark matter searches are an important component of the ATLAS physics programme. Several final state signatures are targeted to maximise the discovery potential. The experimental analyses summarised below are used to constrain the models introduced in Sec. 2. The following analyses summaries serve to illustrate the main components of the selection and analysis strategy, rather than being exhaustive. More details are available in the reference papers.

Electrons, muons, photons and jets are reconstructed combining the signals from the different components of the ATLAS detector[3] [149–154]. Leptons (ℓ) in the following refers to electrons or muons. In several

[3] ATLAS uses a right-handed coordinate system with its origin at the nominal interaction point (IP) in the centre of the detector and the z-axis along the beam pipe. The x-axis points from the IP to the centre of the LHC ring, and the y-axis points upwards. Cylindrical coordinates (r, ϕ) are used in the transverse plane, ϕ being the azimuthal angle around the z-axis. The pseudorapidity

Model and Final State	UFO	Generator and Parton Shower	Cross-section	Additional details
$Z'(\chi\bar{\chi}) + j$	DMV [26, 135]	POWHEG-BOX v2 [136] + PYTHIA 8.205 [137]	NLO	Particle-level re-scaling of leptophobic Z'_A scenario of [26] (see Sec. A.1)
$Z'(\chi\bar{\chi}) + \gamma$	DMSimp [84, 138]	MG5_aMC@NLO 2.4.3 (NLO) [139] + PYTHIA 8.212	NLO	Leptophobic Z'_A scenario simulated, other scenarios obtained by cross-section re-scaling (see Sec. A.1)
$Z'(\chi\bar{\chi}) + V$	DMSimp	MG5_aMC@NLO 2.5.3 (NLO) + PYTHIA 8.212	NLO	Particle-level re-scaling of LO samples of [20] to each of the four NLO scenarios (see Sec. A.1)
$Z'(qq)$ or $Z'(qq)$+ISR	DMSimp	MG5_aMC@NLO 2.2.3 (NLO) + PYTHIA 8.210	NLO	Leptophobic Z'_A scenario simulated, other scenario obtained by Gaussian resonance limits and cross-section re-scaling [140]
$Z'(b\bar{b})$	DMSimp	MG5_aMC@NLO 2.2.3 (NLO) + PYTHIA 8.210	NLO	Leptophobic Z'_A scenario simulated, other scenario obtained by Gaussian resonance limits and cross-section re-scaling [140]
$Z'(\ell\ell)$	DMSimp	MG5_aMC@NLO 2.2.3 (NLO)	NLO	Gaussian resonance limits and cross-section re-scaling [140]
$Z'(t\bar{t})$	DMSimp	MADGRAPH 2.4.3 (LO) + PYTHIA 8.186	LO	Particle-level re-scaling of the topcolour-assisted technicolour samples of [141] (see Sec. A.1)
$Z'_B(\chi\bar{\chi}) + h$	Higgs_scalar [78, 142]	MADGRAPH 2.2.3 (LO) +PYTHIA 8.186	LO	[22], simulated for $h(b\bar{b}) + E_{\mathrm{T}}^{\mathrm{miss}}$
2HDM+Z'_V	Zp2HDM [126, 143]	MADGRAPH 2.2.3 (LO) +PYTHIA 8.186	LO	[22, 23]

Table 2: Details of the generation setup used for the spin-1 mediator simplified models, for each signature considered in this note.

Model and Final State	UFO	Generator and Parton Shower	Cross-section	Additional details
$a(\chi\bar{\chi}) + j$	DMS_tloop [81, 144]	POWHEG-BOX v2 + PYTHIA 8.205	NLO	[26]
$\phi(\chi\bar{\chi}) + t\bar{t}$	DMScalarMed_loop [81, 145]	MADGRAPH 2.3.3 (LO) + PYTHIA 8.186	NLO	[25]
$\phi(\chi\bar{\chi}) + b\bar{b}$	DMScalarMed_loop	MADGRAPH 2.3.3 (LO) + PYTHIA 8.186	NLO	[25]
η_q	dmS_T [73, 146]	MADGRAPH 2.3.3 (LO) + PYTHIA 8.186	LO	[26, 73]
η_b	DM_Bflavored [101, 147]	MADGRAPH 2.3.3 (LO) + PYTHIA 8.186	LO	[25]
2HDM+a: $\chi\bar{\chi} + t\bar{t}/b\bar{b}$	Pseudoscalar_2HDM [120, 148]	MADGRAPH 2.3.3 (LO)	LO	Cross-section based re-scaling from simplified model samples of Ref. [25]
2HDM+a: $\chi\bar{\chi} + Z$	Pseudoscalar_2HDM	MG5_aMC@NLO 2.4.3 (LO) + PYTHIA 8.212	LO	Only gluon initiated production considered [120]
2HDM+a: $\chi\bar{\chi} + h$	Pseudoscalar_2HDM	MG5_aMC@NLO 2.4.3 (LO) + PYTHIA 8.212	LO	b-quark initiated production considered only for $\tan\beta \geq 10$
2HDM+a: $4t$	Pseudoscalar_2HDM	MADGRAPH 2.4.3 (LO) + PYTHIA 8.212	LO	[120]

Table 3: Details of the generation setup used for the spin-0 mediator models, for each signature considered in this note.

analyses, events with identified leptons are rejected from the signal region selection. This is referred to as lepton veto. Each analysis may implement slightly different lepton and photon selection criteria for particle identification [149, 151, 152, 155], isolation [149, 151, 156] and kinematic requirements (p_{T}, η). Small-R and large-R jets are reconstructed from energy deposits in the calorimeters using the anti-k_t jet algorithm [157, 158] and using a radius parameter of $R = 0.4$ and $R = 1.0$, respectively. Reclustered large-R jets are reconstructed using a radius parameter of either $R = 0.8$ or $R = 1.2$ from small-R jets instead. Multivariate algorithms (b-tagging) are used to identify small-R jets with $p_{\mathrm{T}} > 20$ GeV containing b-hadrons (b-jets) [159, 160]. For large-R jets, b-tagging is applied to their associated track-jets, which are defined using tracks reconstructed in the inner detector using the anti-k_t jet algorithm with $R = 0.2$. The missing transverse momentum $\vec{p}_{\mathrm{T}}^{\,\mathrm{miss}}$ (with magnitude $E_{\mathrm{T}}^{\mathrm{miss}}$) is calculated from the negative vector sum of transverse momenta (p_{T}) of electrons, muons, photons and jet candidates and an additional soft term [161] which includes activity in the tracking system originating from the primary vertex but not associated with any reconstructed particle.

4.1 Searches for invisible final states

Searches for WIMP candidates at the LHC are characterised by the requirement of large $E_{\mathrm{T}}^{\mathrm{miss}}$ since WIMPs escape detection. Therefore, final states with additional visible particles are considered in the selection of the events. These additional particles may come from initial state radiation or from associated production. Several signatures that are listed in the following are exploited and optimised to enhance the sensitivity to different DM models.

Jet +$E_{\mathrm{T}}^{\mathrm{miss}}$ The jet+$E_{\mathrm{T}}^{\mathrm{miss}}$ analysis [26], commonly referred to as the monojet analysis, is characterised by the presence of an energetic jet and large $E_{\mathrm{T}}^{\mathrm{miss}}$. The analysis selects events with $E_{\mathrm{T}}^{\mathrm{miss}} > 250$ GeV, at least one jet with $p_{\mathrm{T}} > 250$ GeV and at most three additional jets with $p_{\mathrm{T}} > 30$ GeV. Events are required to pass a lepton veto. To reduce the contribution from multi-jet background where large $E_{\mathrm{T}}^{\mathrm{miss}}$ can originate from jet energy under-measurement, a minimal separation in the azimuthal angle between each selected jet and the $E_{\mathrm{T}}^{\mathrm{miss}}$ direction is also required: $\Delta\phi(\mathrm{jet}, \vec{p}_{\mathrm{T}}^{\,\mathrm{miss}}) > 0.4$. The W+jets, Z+jets, and top-quark-related backgrounds are constrained using MC event samples normalised to data in selected control regions containing leptons. In the case of W+jets and Z+jets events, MC predictions are first reweighted to account for higher-order QCD and electroweak corrections as a function of vector-boson p_{T} [162]. The normalisation factors for these backgrounds are extracted simultaneously using a binned likelihood fit of the $E_{\mathrm{T}}^{\mathrm{miss}}$ distributions of all control and signal regions that includes systematic uncertainties, to properly take into account correlations. The remaining SM backgrounds from di-boson processes are determined using MC simulated samples, while the multi-jet background contribution is extracted from data.

***h*(inv)** Searches for invisible Higgs boson decays have been performed using multiple production and decay channels at a centre-of-mass energy of $\sqrt{s} = 8$ TeV [29]. Searches in the vector-boson fusion (VBF), associated production of a Higgs boson with a W/Z boson and measured production and decay rates of the observed Higgs boson in the $\gamma\gamma$, ZZ, WW, $Z\gamma$, bb, $\tau\tau$ and $\mu\mu$ channels are statistically combined to set an upper limit on the Higgs boson invisible branching ratio of 0.23 at 95% CL. This combined limit is used in

is defined in terms of the polar angle θ as $\eta = -\ln\tan(\theta/2)$. Angular distance is measured in units of $\Delta R \equiv \sqrt{(\Delta\eta)^2 + (\Delta\phi)^2}$. The rapidity is defined at $y = 1/2\ln[(E + p_z)/(E - p_z)]$, where E is the energy and p_z is the component of its momentum along the z-axis. The rapidity difference between two jets is defined as $y^* = (y_1 - y_2)/2$.

the results quoted in Sec. 6. Among these searches, the VBF production of Higgs bosons decaying into invisible particles [163] is the most sensitive, setting an upper limit on the invisible branching ratio of 0.28. The VBF+$E_{\mathrm{T}}^{\mathrm{miss}}$ analysis requires $E_{\mathrm{T}}^{\mathrm{miss}} > 150$ GeV and two jets with $p_{\mathrm{T}} > 35$ GeV. Three orthogonal signal regions are defined by varying the threshold on the leading jet p_{T} and the invariant mass of the two jets. Additional requirements on the angular separation of the two jets are applied to enhance the sensitivity to VBF production. In particular, the two leading jets are required to be well separated in pseudorapidity. Lepton and b-jet vetoes are applied to reduce contamination from $W(\tau\nu)$+jets and top-quark backgrounds, respectively. Dedicated control regions with one and two leptons in the final state are used to constrain the contributions from dominant Z/W+jets backgrounds, through a simultaneous fit together with the signal region. The multi-jet background is estimated using a data-driven technique. Zh(inv) [24] and Vh(inv) [20] searches have been performed at centre-of-mass energy $\sqrt{s} = 13$ TeV. Furthermore, a new VBF+$E_{\mathrm{T}}^{\mathrm{miss}}$ analysis is also available using $\sqrt{s} = 13$ TeV pp collision data [164]. However, the 8 TeV combination gives more stringent limits, thus it is used here.

$\gamma + E_{\mathrm{T}}^{\mathrm{miss}}$ Events in the $\gamma + E_{\mathrm{T}}^{\mathrm{miss}}$ analysis [21] are required to pass the lepton veto and to have a photon with $E_{\mathrm{T}} > 150$ GeV. Events with more than one jet ($p_{\mathrm{T}} > 30$ GeV) or with a jet fulfilling $\Delta\phi(\text{jet}, \vec{p}_{\mathrm{T}}^{\,\mathrm{miss}}) < 0.4$ are further rejected. Three exclusive signal regions, with $E_{\mathrm{T}}^{\mathrm{miss}}$ in different ranges are defined: 150 GeV $< E_{\mathrm{T}}^{\mathrm{miss}} <$ 225 GeV, 225 GeV $< E_{\mathrm{T}}^{\mathrm{miss}} <$ 300 GeV and $E_{\mathrm{T}}^{\mathrm{miss}} > 300$ GeV. The $W\gamma$, $Z\gamma$ and γ+jets backgrounds are normalised in control regions using a likelihood fit of all $E_{\mathrm{T}}^{\mathrm{miss}}$ regions simultaneously. These normalisation parameters are treated as uncorrelated across the three signal regions. The backgrounds due to photons from the misidentification of electrons or jets in processes such as W/Z+jets, di-boson and multi-jet events are estimated using data-driven techniques.

$Z(\ell\ell) + E_{\mathrm{T}}^{\mathrm{miss}}$ The event selection criteria in this analysis [24] are defined by large $E_{\mathrm{T}}^{\mathrm{miss}}$ and a pair of high-p_{T} leptons. Two opposite-sign, same flavour leptons satisfying $p_{\mathrm{T}} > 30$ GeV and $p_{\mathrm{T}} > 20$ GeV are required. The lepton pair is required to have an invariant mass between 76 GeV and 106 GeV, to be consistent with originating from a Z boson. Events with an additional lepton with $p_{\mathrm{T}} > 7$ GeV or a b-jet with $p_{\mathrm{T}} > 20$ GeV are vetoed. To target events consistent with a boosted Z boson produced in the direction opposite to $\vec{p}_{\mathrm{T}}^{\,\mathrm{miss}}$, additional requirements on the azimuthal angle between the dilepton system and $\vec{p}_{\mathrm{T}}^{\,\mathrm{miss}}$ and the angular distance between leptons are applied. A single inclusive $E_{\mathrm{T}}^{\mathrm{miss}}$ signal region is defined with $E_{\mathrm{T}}^{\mathrm{miss}} > 90$ GeV for each of the ee and $\mu\mu$ channels. The dominant background in this analysis, ZZ production, is estimated from MC simulation. The WZ background is normalised to data in a three-leptons control region. The contribution from Z+jets and non-resonant-$\ell\ell$ backgrounds are estimated using data-driven techniques. A statistical combination of both decay channels is used for the final results.

$W(qq')/Z(q\bar{q}) + E_{\mathrm{T}}^{\mathrm{miss}}$ The $W/Z(qq') + E_{\mathrm{T}}^{\mathrm{miss}}$ analysis [20] selects events with $E_{\mathrm{T}}^{\mathrm{miss}} > 150$ GeV and a hadronically decaying W/Z-boson candidate. The vector boson candidate is defined with one large-R jet with $p_{\mathrm{T}} > 250$ GeV in a boosted topology ($E_{\mathrm{T}}^{\mathrm{miss}} > 250$ GeV) or with two small-R jets with $p_{\mathrm{T}} > 20$ GeV in a resolved topology. In both cases, a lepton veto is applied. Additional requirements are applied on the invariant mass of the W/Z-boson candidate. Multiple signal regions are defined according to the b-jet multiplicity. Similarly, multiple control regions are defined based on lepton and b-jet multiplicity. The normalisation of the $t\bar{t}$ and W/Z+jets background processes are constrained using a simultaneous fit of all control and signal regions of the $E_{\mathrm{T}}^{\mathrm{miss}}$ distribution. The subdominant contribution from di-boson and

single-top-quark production is obtained from simulation. Multi-jet contributions are estimated with a data-driven technique.

$h(b\bar{b}) + E_{\mathrm{T}}^{\mathrm{miss}}$ The $h(b\bar{b}) + E_{\mathrm{T}}^{\mathrm{miss}}$ analysis [23] is defined by the requirement of $E_{\mathrm{T}}^{\mathrm{miss}} > 150$ GeV, a lepton veto and the presence of a Higgs boson candidate with invariant mass, m_h. Events with fake $E_{\mathrm{T}}^{\mathrm{miss}}$ are rejected by imposing constrains on $\Delta\phi(\text{jet}, \vec{p}_{\mathrm{T}}^{\,\mathrm{miss}})$. Two distinctive sets of signal regions are defined targeting moderate (resolved) and high (boosted) momentum Higgs boson candidates. In each case, the regions are further split according to whether there are one or two b-jets. The resolved regime, defined in three exclusive $E_{\mathrm{T}}^{\mathrm{miss}}$ regions between 150 GeV and 500 GeV, selects a Higgs boson candidate reconstructed from the two leading b-tagged small-R jets (or from a b-tagged and a non-b-tagged small-R jet) with $p_{\mathrm{T}} > 20$ GeV. In the boosted regime, defined as $E_{\mathrm{T}}^{\mathrm{miss}} > 500$ GeV, the leading large-R jet with $p_{\mathrm{T}} > 200$ GeV is the Higgs boson candidate. The b-jet multiplicity is defined by the number of b-tagged track-jets associated to the large-R jet. Backgrounds involving the production of W/Z bosons in association with heavy flavour quarks or top-pairs are normalised in dedicated control regions distinctive from the signal regions by requiring one or two leptons. A simultaneous binned likelihood fit to the m_h observable is performed in all signal and control regions. The multi-jet background is obtained with a data driven technique. Other subdominant backgrounds are estimated from simulation.

$h(\gamma\gamma) + E_{\mathrm{T}}^{\mathrm{miss}}$ The $h(\gamma\gamma) + E_{\mathrm{T}}^{\mathrm{miss}}$ events in this analysis [22] are selected by requiring at least two photons with $p_{\mathrm{T}} > 25$ GeV. The two leading photons are chosen to reconstruct the Higgs candidate, and satisfy 105 GeV $< m_{\gamma\gamma} <$ 160 GeV. The leading (sub-leading) photon is also required to have $E_{\mathrm{T}}^{\gamma}/m_{\gamma\gamma} >$ 0.35(0.25). Events with leptons are vetoed. Events with $p_{\mathrm{T}}(\gamma\gamma) > 90$ GeV and $E_{\mathrm{T}}^{\mathrm{miss}}/\sqrt{\sum E_{\mathrm{T}}} > 7$ GeV$^{1/2}$ in Ref. [22] are used for the interpretation of DM models, where $\sum E_{\mathrm{T}}$ is the scalar sum of the transverse momentum of all reconstructed objects. The backgrounds are extracted by fitting an analytic function to the di-photon invariant mass distribution. In the case of the non-resonant background, the normalisation and shape is obtained by fitting the invariant mass distribution in data to an exponential function. The SM Higgs boson background shape is modelled with a double-sided Crystal Ball function and fitted to the MC simulation.

$b(\bar{b}) + E_{\mathrm{T}}^{\mathrm{miss}}$ The $b + E_{\mathrm{T}}^{\mathrm{miss}}$ analysis [25] selects events with two energetic jets ($p_{\mathrm{T}} > 160$ GeV), at least one of which is b-tagged, $E_{\mathrm{T}}^{\mathrm{miss}} > 650$ GeV and an additional total hadronic energy restricted to be less than 100 GeV. This last requirement rejects top background. The dominant background for this analysis, Z+jets events, is constrained from data in a dedicated control region, which is fitted together with the signal region to extract the final results. The $b\bar{b} + E_{\mathrm{T}}^{\mathrm{miss}}$ analysis [25] instead exploits a selection with at least two b-jets and a considerably lower $E_{\mathrm{T}}^{\mathrm{miss}}$ requirement, $E_{\mathrm{T}}^{\mathrm{miss}} > 180$ GeV. The azimuthal separations between the b-jets and $\vec{p}_{\mathrm{T}}^{\,\mathrm{miss}}$ are exploited to enhance the separation between the signal and the irreducible background in this channel ($Z(\nu\bar{\nu})$+$b\bar{b}$), which is constrained from data in a dedicated control region. The final results are extracted by fitting an observable that relies on the pseudorapidity difference between the two b-jets: $\cos\theta^*_{bb} = \left|\tanh\left(\frac{\Delta\eta_{bb}}{2}\right)\right|$.

$t\bar{t} + E_{\mathrm{T}}^{\mathrm{miss}}$ The $t\bar{t} + E_{\mathrm{T}}^{\mathrm{miss}}$ analysis [25, 27, 28] is split into three channels according to the decays of the W-bosons from the top-quark decays: 0-lepton, where both W bosons decay hadronically, 1-lepton, where one of the two W bosons decays leptonically and 2-leptons where both W bosons decay leptonically. The

Analysis	Models targeted	Final state signature	Key Characteristics	Results
Jet $+E_{\mathrm{T}}^{\mathrm{miss}}$ [26]	V/AV(∗), S/PS(∗), $\mathrm{SCC}_q(*)$	1-4 jets, $E_{\mathrm{T}}^{\mathrm{miss}}$, 0 ℓ.	Binned likelihood fit of $E_{\mathrm{T}}^{\mathrm{miss}}$.	Sec. 6.1.1, 6.2.1, 6.2.2
h(inv) [29, 163]	2HDM+a	2 jets, $E_{\mathrm{T}}^{\mathrm{miss}}$, m_{jj}, $\Delta\eta_{jj}$.	Single-bin likelihood fit.	Sec. 6.3.2
$\gamma + E_{\mathrm{T}}^{\mathrm{miss}}$ [21]	V/AV(∗)	1 photon, 0-1 jets, $E_{\mathrm{T}}^{\mathrm{miss}}$, 0 ℓ.	Binned likelihood fit of $E_{\mathrm{T}}^{\mathrm{miss}}$.	Sec. 6.1.1
$Z(\ell\ell) + E_{\mathrm{T}}^{\mathrm{miss}}$ [24]	V/AV, 2HDM+a	2 ℓ, $E_{\mathrm{T}}^{\mathrm{miss}}$, $m_{\ell\ell} \sim m_Z$.	Binned likelihood fit of $E_{\mathrm{T}}^{\mathrm{miss}}$	Sec. 6.1.1, 6.3.2
$W/Z(qq') + E_{\mathrm{T}}^{\mathrm{miss}}$ [20]	V/AV, 2HDM+a	$E_{\mathrm{T}}^{\mathrm{miss}}$, W/Z candidate (resolved and boosted topologies).	Binned likelihood fit of $E_{\mathrm{T}}^{\mathrm{miss}}$.	Sec. 6.1.1, 6.3.2
$h(b\bar{b}) + E_{\mathrm{T}}^{\mathrm{miss}}$ [23]	VBC, 2HDM+Z'_V(∗), 2HDM+a	$E_{\mathrm{T}}^{\mathrm{miss}}$, h candidate (resolved and boosted topologies).	Binned likelihood fit of m_h in bins of $E_{\mathrm{T}}^{\mathrm{miss}}$.	Sec. 6.1.2, 6.3.1, 6.3.2
$h(\gamma\gamma) + E_{\mathrm{T}}^{\mathrm{miss}}$ [22]	VBC, 2HDM+Z'_V(∗), 2HDM+a	2 photons, $m_{\gamma\gamma} \sim m_h$, $E_{\mathrm{T}}^{\mathrm{miss}}$.	Analytic function fit of $m_{\gamma\gamma}$.	Sec. 6.1.2, 6.3.1, 6.3.2
$b(\bar{b}) + E_{\mathrm{T}}^{\mathrm{miss}}$ [25]	S/PS(∗), SCC_b(∗), 2HDM+a	1-2 b-jets, $E_{\mathrm{T}}^{\mathrm{miss}}$, 0 ℓ.	Binned likelihood fit of $\cos\theta^*_{bb}$.	Sec. 6.2.1, 6.2.2, 6.3.2
$t\bar{t} + E_{\mathrm{T}}^{\mathrm{miss}}$ [25, 27]	S/PS(∗), SCC_t(∗), 2HDM+a	0-2ℓ, 1-2 b-jets, ≥ 4 jets, $E_{\mathrm{T}}^{\mathrm{miss}}$, $m_{\mathrm{T2}}^{\ell\ell}$.	Binned likelihood fit.	Sec. 6.2.1, 6.2.2, 6.3.2

Table 4: Summary of searches for invisible final states used to constrain the different DM models defined in Sec. 2. The (∗) indicates models which have been already presented in the original publication, all others are either new or updated.

0-lepton analysis is characterised by a set of signal regions which select events with at least four energetic jets, at least two of which b-tagged, and relatively high $E_{\mathrm{T}}^{\mathrm{miss}}$. Requirements on the invariant mass of re-clustered large-R jets are imposed to identify events where a W boson or a top quark are boosted. The dominant backgrounds (Z+jets, top processes and $t\bar{t} + Z$) are constrained in dedicated control regions. The analysis targeting the 1-lepton channel selects events with at least four energetic jets, at least one of which b-tagged, one isolated lepton and high $E_{\mathrm{T}}^{\mathrm{miss}}$. The events are also required to have at least one hadronic top candidate with invariant mass loosely compatible with the one of the top-quark. Requirements on the transverse and asymmetric stransverse masses [27] are used to suppress semi-leptonic and di-leptonic $t\bar{t}$ events, respectively. Requirements on the azimuthal angle between the lepton and the $\vec{p}_{\mathrm{T}}^{\,\mathrm{miss}}$ and the $\Delta\phi(\text{jets}, \vec{p}_{\mathrm{T}}^{\,\mathrm{miss}})$ are also exploited to further suppress the background contamination of the signal regions. All top background processes are estimated in dedicated control regions. Finally, the analysis targeting the 2-lepton channel selects events with two opposite-sign leptons which are inconsistent with being produced in the decay of a Z-boson. At least one b-jet is also required in the selections. The $E_{\mathrm{T}}^{\mathrm{miss}}$ and the stransverse mass ($m_{\mathrm{T2}}^{\ell\ell}$ [25]) requirements are such that $m_{\mathrm{T2}}^{\ell\ell} + 0.2 \cdot E_{\mathrm{T}}^{\mathrm{miss}} > 170$ GeV. The dominant backgrounds in this analysis ($t\bar{t}$ and $t\bar{t} + Z$) are estimated in dedicated control regions.

Table 4 summarises the DM searches for invisible final states. None of these analyses shows a significant deviation from the expected SM background, and thus exclusion limits can be set for the relevant models. These limits are discussed in Sec. 6. The observed $E_{\mathrm{T}}^{\mathrm{miss}}$ distributions compared to the background predictions are shown in Fig. 7 for the $h(b\bar{b}) + E_{\mathrm{T}}^{\mathrm{miss}}$ and $Z(\ell\ell) + E_{\mathrm{T}}^{\mathrm{miss}}$ analyses, with representative 2HDM+a signal distributions shown in each case. These two analyses have the strongest sensitivity for this model, as discussed in Section 6.3.2.

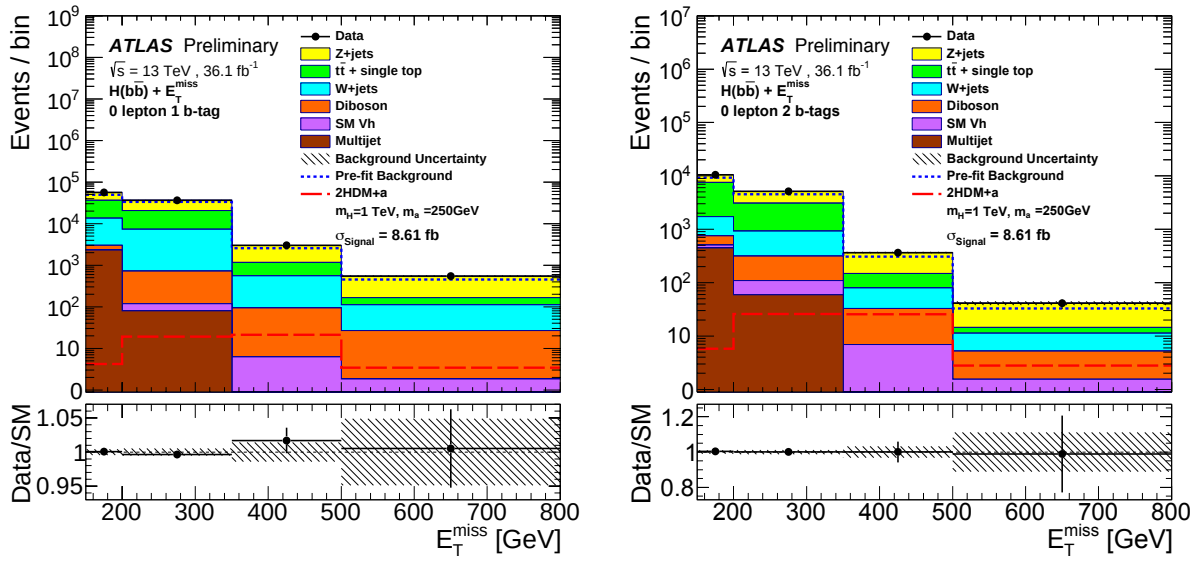

(a) (b)

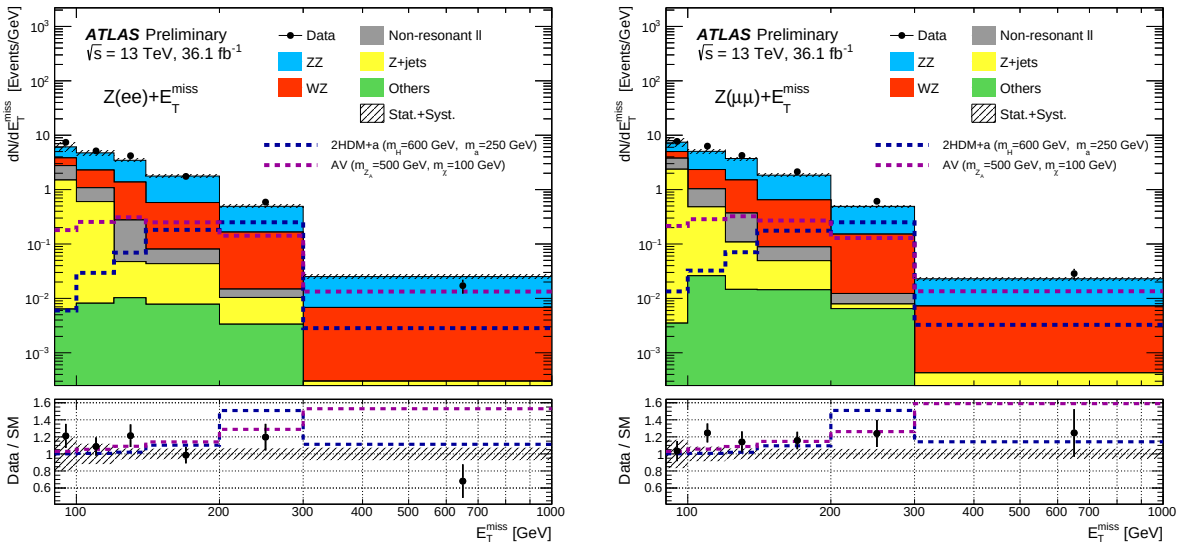

(c) (d)

Figure 7: Observed $E_{\mathrm{T}}^{\mathrm{miss}}$ distribution in the $h(b\bar{b}) + E_{\mathrm{T}}^{\mathrm{miss}}$ analysis in the (a) 1 b-tag and (b) 2 b-tag signal regions compared to the background predictions. The error bands show the total statistical and systematic uncertainties on the background predictions. The expected $E_{\mathrm{T}}^{\mathrm{miss}}$ distribution for a representative signal model is shown. This corresponds to a 2HDM+a signal with $m_a = 250$ GeV, $m_H = m_{H^\pm} = m_A = 1000$ GeV, $\tan\beta = 1.0$, $\sin\theta = 0.35$, $g_\chi = 1.0$ and $m_\chi = 10$ GeV. Observed $E_{\mathrm{T}}^{\mathrm{miss}}$ distribution in the $Z(\ell\ell) + E_{\mathrm{T}}^{\mathrm{miss}}$ analysis in the (c) ee and (d) $\mu\mu$ signal regions compared to the background predictions. The expected $E_{\mathrm{T}}^{\mathrm{miss}}$ distribution for representative signal models are shown. This corresponds to a 2HDM+a signal with $m_a = 250$ GeV, $m_H = m_{H^\pm} = m_A = 600$ GeV, $\tan\beta = 1.0$, $\sin\theta = 0.35$, $g_\chi = 1.0$ and $m_\chi = 10$ GeV, and an AV signal with $m_{Z'_A} = 500$ GeV, $m_\chi = 100$ GeV, $g_q = 0.25$, $g_\ell = 0$, and $g_\chi = 1.0$.

4.2 Searches for visible final states

Multiple searches for narrow resonances are interpreted in terms of the DM models described in Sec. 2. These searches explore several final state signatures by selecting different visible particles, thus requiring the presence of reconstructed objects such as jets or leptons, covering a variety of kinematic regions. In some of the analyses described below, further identification techniques are employed to select final states with top quarks.

Dijet For this analysis [165] events with at least two small-R jets are selected if the p_{T} of the leading (sub-leading) jet is greater than 440(60) GeV. The dijet selection imposes $|y^*| < 0.6$ and the invariant mass of the dijet system to be $m_{jj} > 1.1$ TeV. The final background estimation is obtained by fitting the falling m_{jj} distribution. Bins widths are chosen to approximate the m_{jj} resolution, and thus are wider for higher masses. A sliding-window fitting technique is used, where restricted regions of the spectrum are fitted with a functional form. The background is constructed bin-by-bin by performing a likelihood fit to the data in each window and using the fit value in the central bin for the background estimation. The values from the full set of windows are then combined to create the background estimate for the full mass range. The BumpHunter algorithm [166] is used to quantify the statistical significance of any localised excess in the m_{jj} distribution. Model independent limits on the visible cross-section for a hypothetical signal that produces a Gaussian contribution to the m_{jj} distribution (for multiple signal widths) are provided for this analysis (see Appendix A of [167]).

Dijet angular A dijet selection can also be exploited to search for deviations in angular distributions, characteristic of wider resonances where the nominal dijet search would lose sensitivity. A dijet angular analysis [165] is performed in events with two jets following the p_{T} requirements of the dijet search, but relaxing the $|y^*|$ cut to 1.7. Due to different kinematics in this loosened selection, the mass of the dijet pair is required to be $m_{jj} > 2.5$ TeV. The analysis makes use of the variable $\chi_{jj} = e^{2|y^*|} \sim (1+\cos\theta^*)/(1-\cos\theta^*)$, constructed such that, in the limit of massless parton scattering and when only the t-channel scattering contributes to the partonic cross-section, the angular distribution $dN/d\chi_{jj}$ is approximately independent of χ_{jj}. MC events from multijet production are modelled at LO in QCD, and reweighted to NLO predictions of NLOJET++ [168, 169] using mass- and angle-dependent correction factors. Additional electroweak mass- and angle-dependent correction factors are applied. using an angle- and mass-dependent correction factors. Additional electroweak correction factors The data is compared to a SM template in different m_{jj} ranges, and different χ_{jj} bins.

Trigger-object-level dijet For the dijet analysis described before, the high p_{T} threshold imposed in the leading jet is limited by the high-level trigger selection driven by the bandwidth available for single jet triggers, thus it only targets $m_{jj} > 1.5$ TeV. This limitation is overcome by recording only high-level trigger jet information, rather than the full detector readout, to a dedicated data stream, reducing the storage needs per event. This strategy allows higher event rate with minimal bandwidth, meaning that all events passing the single jet L1 trigger (lower threshold than high-level trigger) can be recorded to this stream. The dataset collected corresponds to an integrated luminosity of 29.3 fb^{-1} This trigger-object-level dijet analysis (TLA dijet) [170] selects events with at least two trigger-level jets with $p_{\mathrm{T}} > 85$ GeV. Two selection criteria are used: $|y^*| < 0.6$ in the mass range 700 GeV $< m_{jj} <$ 1800 GeV and $|y^*| < 0.3$ for 450 GeV $< m_{jj} <$ 700 GeV. The leading trigger-level jet is required to have a $p_{\mathrm{T}} > 185$ GeV and

$p_T > 220$ GeV for the $|y^*| < 0.3$ and $|y^*| < 0.6$ selections, respectively, to ensure full efficiency for the L1 triggers. The search is then interpreted in terms of resonances with a mass between 450 GeV and 1800 GeV. The background strategy used in the dijet search is also used here.

Resolved dijet + ISR Another alternative strategy to search for low mass dijet resonances is to select events with a pair of jets recoiling against a photon or an additional jet from ISR. The resolved dijet + ISR analysis [171] selects events with a high p_T ISR object (γ or jet) and a relatively low mass dijet resonance. Dijet+γ events contain at least one photon with $p_\gamma > 150$ GeV and at least two jets with $p_T > 25$ GeV. The two leading jets should satisfy $|y^*| < 0.8$, which allows to probe dijet invariant masses between 170 GeV and 1.5 TeV. The three jet selection requires at least one jet with $p_T > 430$ GeV as well as two additional jets with $p_T > 25$ GeV. The leading jet is chosen as the ISR candidate, and the second and third highest p_T jets are required to satisfy $|y^*| < 0.6$. This selection probes a mass range between about 300 GeV and 600 GeV. The background contribution is estimated by fitting a parametric function to the m_{jj} distribution. This analysis was performed in 13 TeV collision data corresponding to an integrated luminosity of 15.5 fb^{-1}.

Boosted dijet + ISR In the case of a dijet+ISR selection, if the associated ISR photon or jet has large transverse momentum, the dijet resonance candidate is reconstructed as a large-R jet [172] of radius 1.0. To enhance the sensitivity to quark pair decays, jet substructure techniques are used to discriminate between a two-particle jet from a decay of a boosted resonance and a single-particle jet [173]. Events are required to have a large-R jet, the resonance candidate, and at least one ISR object candidate. The azimuthal angular separation between the resonance candidate and the ISR object satisfies $\Delta\phi > \pi/2$. $p_T > 2 \times m$ is required to ensure sufficient collimation of the resonance candidate. In the ISR jet (photon) channel, the large-R jet satisfies $p_T > 450(200)$ GeV and the ISR jet (photon) has $p_T > 450(155)$ GeV. A data-driven technique is used to model the expected background in the signal region via a transfer factor that extrapolates from a control region with inverted jet substructure requirements.

Dibjet The dibjet search [174] targets dijet resonances with one or two jets identified as b-jets. Two different analyses are defined to cover both low and high invariant mass regions. The high invariant mass region events are selected with at least two jets, one of which has $p_T > 430$ GeV and passes an inclusive jet trigger. The rapidity difference is required to be $|y^*| < 0.8$. This analysis covers the region with $m_{jj} > 1.2$ TeV. The low invariant mass region uses a trigger targeting events with two jets containing b-hadrons, which allows to reach lower dibjet invariant masses (m_{jj}) compared to the single jet trigger: 570 GeV $< m_{jj} <$ 1.5 TeV. The rapidity difference requirement is tightened to $|y^*| < 0.6$. In this case, only the two b-tags selection is considered. Because the double b-jet trigger was not available during the full data taking period, the total integrated luminosity used for the low mass analysis corresponds to 24.3 fb^{-1} of 13 TeV collision data. A similar background estimation strategy to that of the dijet analysis is used in these analyses, separately.

Dilepton The dilepton analysis [175] selects events with at least two same-flavour leptons. The pair of electrons (muons) with highest E_T (p_T) are chosen as the resonance candidate. Only in the muon channel candidates are required to have opposite charge, due to higher charge mis-identification for high-E_T electrons and the p_T mis-reconstruction associated to wrongly measured charge in muons. Background processes with two real leptons are modelled using MC samples. The $Z/\gamma^* \to \ell\ell$ background is smoothed

for 120 GeV $< m_{\ell\ell} <$ 1 TeV. This is done by fitting the spectrum in MC and the resulting fitted function is used to set the expected event yields in that mass range. A data-driven method is employed to estimate backgrounds with at least one misidentified lepton. The $m_{\ell\ell}$ distribution is explored between 80 GeV and 6 TeV .

$t\bar{t}$ resonance The $t\bar{t}$ resonance analysis [141] selects events with two top-quark candidates. Events are required to have a leptonic top-quark decay, selected by requiring a charged lepton and $E_{\mathrm{T}}^{\mathrm{miss}}$ consistent with a leptonic decay of a W boson, and a small-R jet close-by. Events are classified as boosted or resolved based on their hadronic activity. In the boosted selection, events contain one large-R jet passing top-tagging requirements. In the resolved selection, events have at least four small-R jets and fail the boosted selection. The $t\bar{t}$ invariant mass, $m_{t\bar{t}}$, is constructed from the decay products of the two top-quark candidates in the event. The b-jet multiplicity is used for further categorisation. The SM $t\bar{t}$ production is estimated using MC samples and fixed-order theory calculations. The multi-jet and W+jets background contribution is estimated using data driven techniques.

$t\bar{t}t\bar{t}$ The $t\bar{t}t\bar{t}$ analysis [176] searches for events characterised by a single lepton and high jet multiplicity. Events are categorised by their jet multiplicity, which is defined based on three p_{T} thresholds: 40 GeV, 60 GeV and 80 GeV. Events are further classified in five bins corresponding to the b-jet multiplicity. The $t\bar{t}$+jets and W/Z+jets backgrounds production is estimated using a combined fit to these jet and b-jet multiplicity bins. The normalisation of these backgrounds is extrapolated from lower to higher jet multiplicity, while the b-jet multiplicity shape is taken from a parameterised extrapolation from data (simulation) for the $t\bar{t}$ (W/Z+jets) background.

Table 5 summarises the searches for visible final states. As in the case of the searches for invisible final states, these analyses found no significant deviation from the expected SM backgrounds. Therefore, exclusion limits on the allowed phase space of the corresponding signal models are placed, as discussed in Sec. 6.

Analysis	Models targeted	Final state signature	Key Characteristics	Results
Dijet [165]	V/AV	2 jets, m_{jj}, y^*.	Sliding-window fit of the m_{jj} distribution.	Sec. 6.1.1
Dijet angular [165]	V/AV	2 jets, m_{jj}, y^*.	Binned likelihood fit of χ_{jj}.	Sec. 6.1.1
TLA dijet [170]	V/AV	2 trigger-level jets, m_{jj}, y^*.	Sliding-window fit of the m_{jj} distribution.	Sec. 6.1.1
Resolved dijet+ISR [171]	V/AV	3 jets (or 2jets and 1 photon), m_{jj}, y^*.	Parametric function fit of the m_{jj} distribution.	Sec. 6.1.1
Boosted dijet+ISR [172]	V/AV(∗)	1 large-R jet, 1 jet or photon, m_J.	Data driven extrapolation from control region via transfer factor.	Sec. 6.1.1
Dibjet [174]	V/AV	2 jets (1 and 2 b-jets), m_{jj}, y^*.	Sliding-window parametric fit of the m_{jj} distribution.	Sec. 6.1.1
Dilepton [175]	V/AV	2 e or 2 μ.	$Z/\gamma^* \to \ell\ell$ from fitted MC spectrum.	Sec. 6.1.1
$t\bar{t}$ resonance [141]	V/AV	1 ℓ, hadronic t candidate (resolved and boosted topologies), $E_{\mathrm{T}}^{\mathrm{miss}}$.	$t\bar{t}$ bkg from MC and fixed-order theory calculations.	Sec. 6.1.1
$t\bar{t}t\bar{t}$ [176]	2HDM+a	1 ℓ, high jet multiplicity.	Parameterised extrapolation from low to high jet multiplicity.	Sec. 6.3.2

Table 5: Summary of searches for visible final states used to constrain the different DM models defined in Sec. 2. The (∗) indicates models which have been already presented in the original publication, all others are either new or updated.

4.3 Complementarity and combination of signatures

It can be seen from Tables 4 and 5 that often several analyses are sensitive to a given model. In cases like the $X + E_{\mathrm{T}}^{\mathrm{miss}}$ final states searches, X originating from initial state radiation or associated production, a variety of final states are considered: $X = \mathrm{jet}, \gamma, W, Z, h, t\bar{t}, (b)\bar{b}$. Since the mediator couples DM to SM particles, it is also possible to reinterpret results from multiple resonance searches targeting directly the mediator. The complementarity will depend on the choice of model as well as coupling values. For the V/AV model we consider $\mathrm{jet}/\gamma/V + E_{\mathrm{T}}^{\mathrm{miss}}$, dijet, dibjet and $t\bar{t}$ resonance final states. All results for this model are new or have been updated from previous publications, except for the $\mathrm{jet}/\gamma + E_{\mathrm{T}}^{\mathrm{miss}}$ interpretations. For the VBC and 2HDM+Z'_V models, we consider in this note only $h + E_{\mathrm{T}}^{\mathrm{miss}}$, which is the dominant signature for these models within the considered choice of parameters. Only invisible final states, $t\bar{t}/b\bar{b}/\mathrm{jet} + E_{\mathrm{T}}^{\mathrm{miss}}$, are instead considered so far for the S/PS model. The SCC_q and SCC_b models are each addressed with a specific signature: $\mathrm{jet} + E_{\mathrm{T}}^{\mathrm{miss}}$ and $b + E_{\mathrm{T}}^{\mathrm{miss}}$, respectively and all results were already presented in each specific analysis paper. Various final states are considered to present the first constraints to the 2HDM+a model by ATLAS searches: $Z/h + E_{\mathrm{T}}^{\mathrm{miss}}$, $t\bar{t}/b\bar{b} + E_{\mathrm{T}}^{\mathrm{miss}}$, $h(\mathrm{inv})$ and $t\bar{t}t\bar{t}$.

Complementarity can also be found in studying different SM decay channels of a given final state signature. Two natural candidates from the analyses discussed here are the $h + E_{\mathrm{T}}^{\mathrm{miss}}$ $(b\bar{b}, \gamma\gamma)$ searches and the $t\bar{t} + E_{\mathrm{T}}^{\mathrm{miss}}$ (fully hadronic, semi-leptonic and fully leptonic).

The results from the $h + E_{\mathrm{T}}^{\mathrm{miss}}$ searches presented in Sec. 6.3.1 correspond to a statistical combination of the $h(b\bar{b}) + E_{\mathrm{T}}^{\mathrm{miss}}$ and $h(\gamma\gamma) + E_{\mathrm{T}}^{\mathrm{miss}}$ searches. The $h(b\bar{b}) + E_{\mathrm{T}}^{\mathrm{miss}}$ analysis has a larger reach in mediator masses, however its sensitivity it is limited at lower masses by the threshold requirement of the $E_{\mathrm{T}}^{\mathrm{miss}}$ trigger used to record the events for this analysis. The $h(\gamma\gamma) + E_{\mathrm{T}}^{\mathrm{miss}}$ covers a lower masses region given its selection based on a photon trigger. For the combination the luminosity uncertainty, the experimental uncertainties and signal modelling uncertainties were correlated between the two channels. In the $h(\gamma\gamma) + E_{\mathrm{T}}^{\mathrm{miss}}$ analysis the systematic uncertainties are not significantly constrained by the fit. This is mainly due to the use of a single signal region and no control regions used. In the case of $h(b\bar{b}) + E_{\mathrm{T}}^{\mathrm{miss}}$ the systematics uncertainties

can be constrained due to the use of dedicated control regions. It is observed, however, that the results from the combination and the individual $h(b\bar{b}) + E_{\mathrm{T}}^{\mathrm{miss}}$ results are very similar. While the $h(b\bar{b}) + E_{\mathrm{T}}^{\mathrm{miss}}$ channel dominates the sensitivity, searches in different decay channels are of interest to probe different kinematic regions defined by different analyses strategies.

For this note, the $t\bar{t} + E_{\mathrm{T}}^{\mathrm{miss}}$ exclusion limits discussed in Sec. 6 are combined based on the best expected exclusion for each signal model, unless separate contours are shown. In cases where the sensitivity is comparable between different decay channels there is a potential gain for a statistical combination, but it is not considered in this work.

5 Systematic uncertainties

Systematic uncertainties for both the background and signal models are considered in each of the analyses presented in Sec. 4. These uncertainties, as well as statistical uncertainties, are highly dependent on the event selection, the phase space covered by a given analysis and its background estimation strategy. The systematic uncertainties include both experimental and theoretical uncertainties. Experimental uncertainties may include uncertainties on the absolute jet and $E_{\mathrm{T}}^{\mathrm{miss}}$ energy scales and resolutions, uncertainties related to jet quality requirements, pile-up corrections, b-tagging efficiencies and uncertainties on the soft contributions to $E_{\mathrm{T}}^{\mathrm{miss}}$. Uncertainties on lepton identification and reconstruction efficiencies, energy/momentum scale and resolution are considered for events with selected or vetoed leptons. Additionally uncertainties on the luminosity are considered. Uncertainties due to the finite statistics of the background MC samples and others related to the modelling of the background processes are also included in the analyses. The detailed description and in depth discussion of the systematic uncertainties on the background estimation are found in the individual papers.

The signal modelling is subject to both experimental and theoretical uncertainties. The experimental uncertainties are the same as for the background processes. In general, theoretical uncertainties affecting the production cross-section (normalisation) and the acceptance are considered separately. The systematic uncertainties strategy for those signal models studied in this note that are not discussed in previous publications are outlined below.

The results for the 2HDM+a signal model consider theoretical systematic uncertainties due to parton distribution functions (PDFs), evaluated following the PDF4LHC recommendations [177]. The choice of different PDFs results in up to 2% uncertainty in the acceptance and up to a 10% uncertainty in the cross-section. Uncertainties related to the choice of the renormalisation and factorisation scales are derived by varying such scales by a factor of 2.0 and 0.5 with respect to the nominal values used for the MC generation. They account for an uncertainty on the acceptance below 5% for the different analyses. Uncertainties in initial and final state radiation due to the parton shower modelling are estimated estimated by generating MC samples with alternative tunes and parameters choices, resulting in uncertainties between 5% and 15% in the signal acceptance, typically increasing at higher mediator masses. In the very large jet multiplicity phase space of the $t\bar{t}t\bar{t}$ analysis they reach values of 50%.

In some cases, additional uncertainties are included to account for non-closure effects of the re-scaling procedure described in Sec. 3. These uncertainties include a contribution from the statistical uncertainty associated with the acceptance ratios determined from the baseline signal sample. For the $h(\gamma\gamma) + E_{\mathrm{T}}^{\mathrm{miss}}$ ($Z(\ell\ell) + E_{\mathrm{T}}^{\mathrm{miss}}$) analysis this translates in up to 7% (8%) uncertainties to the final 2HDM+a signal yields.

6 Interpretation of the results

This section summarises the exclusion limits placed by ATLAS experimental searches, all already published and briefly outlined in Sec. 4, on the various signal models described in Sec. 2 (following the notation in Table 1). The analyses and corresponding signal regions are referred to by their analysis labels defined in Tables 4 and 5. The final combined observed and expected 95% confidence level (CL) exclusion limits are obtained from the signal region or combination of regions of each contributing analysis using the CL_s [178] method. In Sec. 6.3.1 a statistical combination of the $h + E_T^{miss}$ final states is used to derive the final results.

6.1 Vector or axial vector dark matter models

6.1.1 Neutral interaction

The V/AV simplified model is strongly constrained by searches for a high-mass resonance decaying into a pair of fermions and searches for associated production of DM particles with an ISR object.

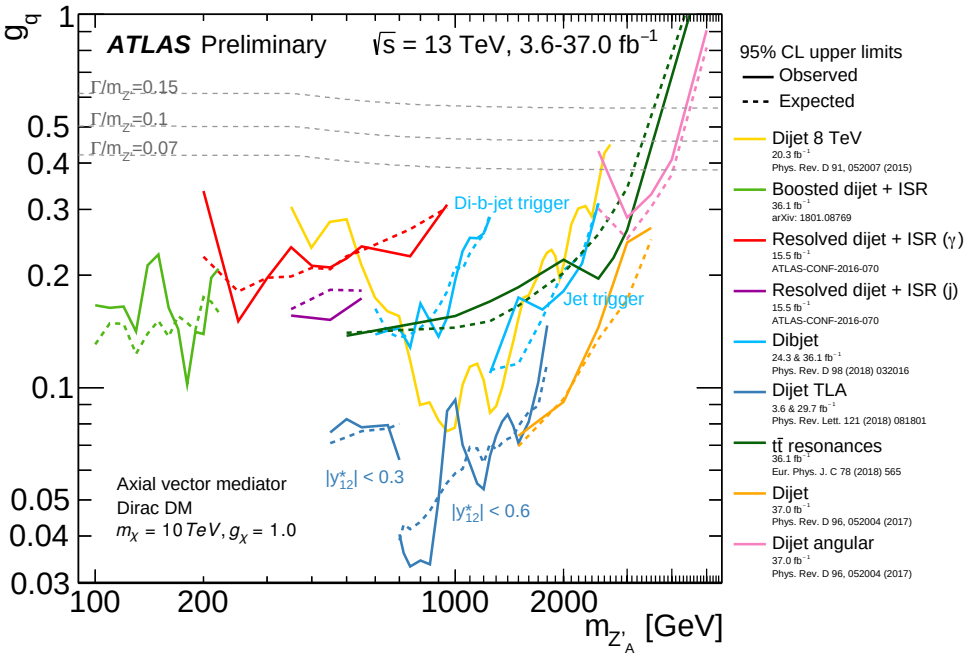

Figure 8: 95% CL upper limits in the coupling-mediator mass plane from dijet searches on coupling g_q as a function of the resonance mass $m_{Z'_A}$ for the leptophobic axial-vector Z'_A model. The expected limits from each search are indicated by dotted lines. The TLA dijet analysis has two parts, employing different datasets with different selections in the rapidity difference y^* as marked. The yellow contour shows the results of the dijet search using 20.3 fb^{-1} of 8 TeV data. Coupling values above the solid lines are excluded, as long as the signals are narrow enough to be detected using these searches. The TLA dijet with $|y^*| < 0.6$ is sensitive up to $\Gamma/m_{Z'} = 7\%$, the TLA dijet with $|y^*| < 0.3$ and dijet + ISR are sensitive up to $\Gamma/m_{Z'} = 10\%$, and the dijet and dibjet analyses are sensitive up to $\Gamma/m_{Z'} = 15\%$. Finally, dijet angular is sensitive up to $\Gamma/m_{Z'} = 50\%$. No limitation in sensitivity arises from large width resonances for the $t\bar{t}$ resonance analysis. Benchmark width lines are indicated in the canvas.

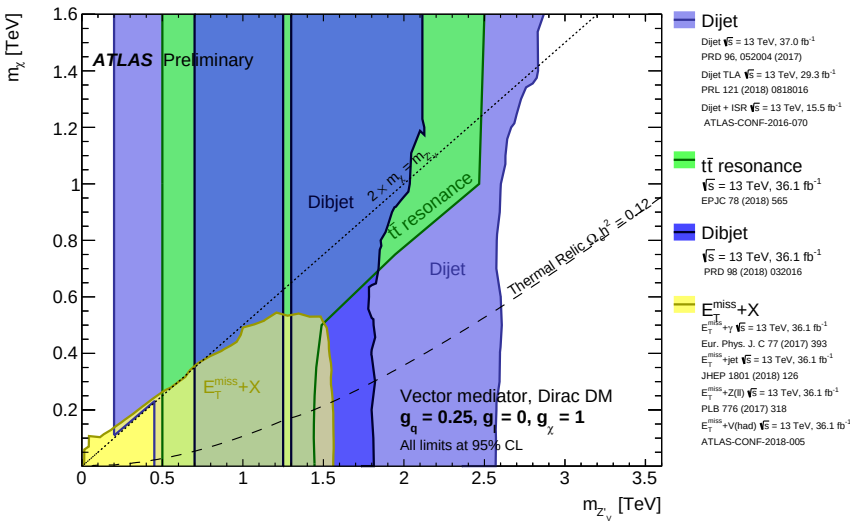

(a)

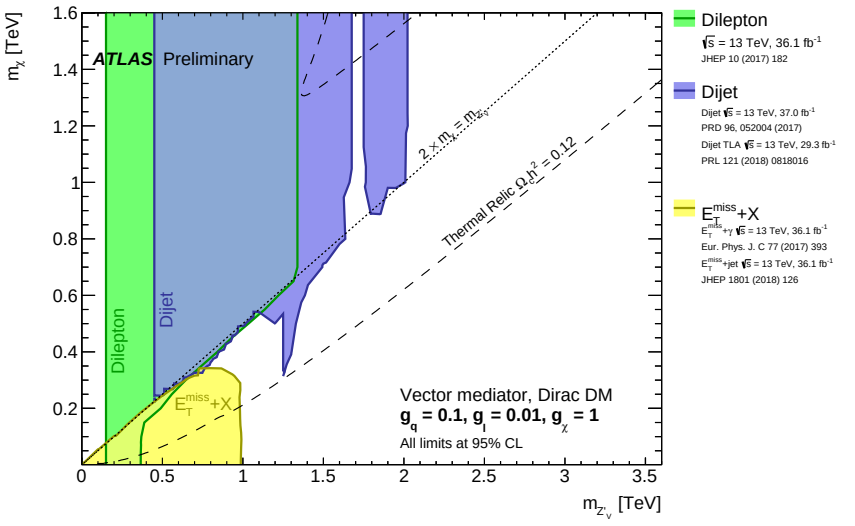

(b)

Figure 9: Regions in a DM mass-mediator mass plane excluded at 95% CL by dijet, dilepton and $E_{\mathrm{T}}^{\mathrm{miss}}+X$ searches, for vector mediator simplified models described in Sec. 2.1.1. The exclusions are computed for a DM coupling g_χ, quark coupling g_q, universal to all flavours, and lepton coupling g_ℓ as indicated in each case. Dashed curves labeled "thermal relic" indicate combinations of DM and mediator mass that are consistent with a DM density of $\Omega h^2 = 0.12$ and a standard thermal history, as computed in MadDM [41, 179]. To the left of the curve in (a) annihilation processes described by the simplified model deplete Ωh^2 below 0.12. In (b), this occurs between the two dashed curves. A dotted line indicates the kinematic threshold where the mediator can decay on-shell into DM.

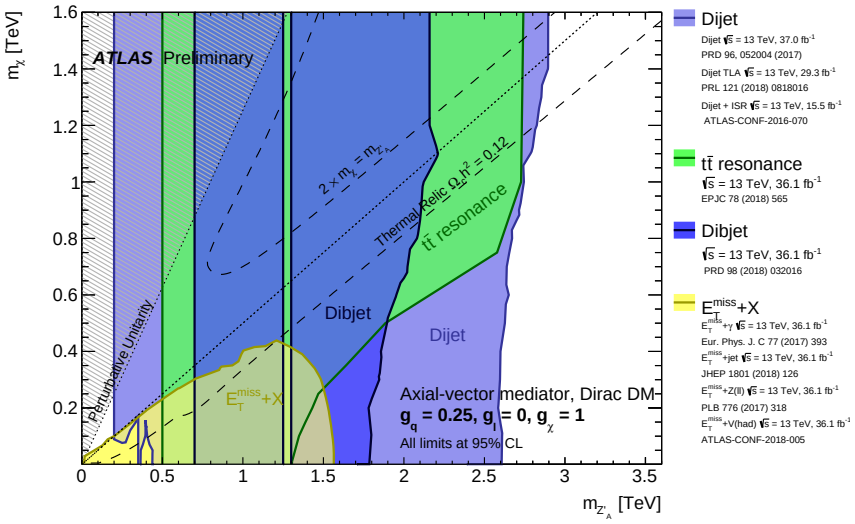

(a)

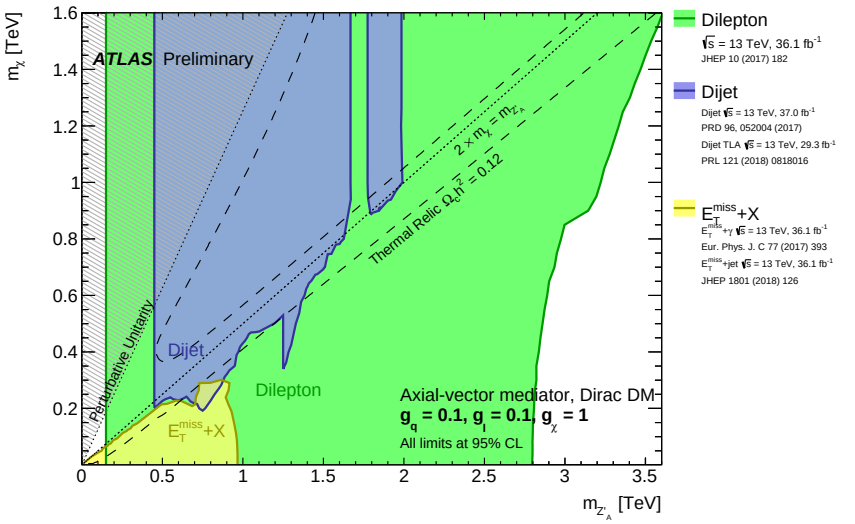

(b)

Figure 10: Regions in a DM mass-mediator mass plane excluded at 95% CL by dijet, dilepton and $E_{\mathrm{T}}^{\mathrm{miss}}+X$ searches, for axial-vector mediator simplified models described in Sec. 2.1.1. The exclusions are computed for a DM coupling g_χ, quark coupling g_q, universal to all flavours, and lepton coupling g_ℓ as indicated in each case. Dashed curves labeled "thermal relic" indicate combinations of DM and mediator mass that are consistent with a DM density of $\Omega h^2 = 0.12$ and a standard thermal history, as computed in MadDM [41, 179]. Between the two curves, annihilation processes described by the simplified model deplete Ωh^2 below 0.12. A dotted line indicates the kinematic threshold where the mediator can decay on-shell into DM. Excluded regions that are in tension with the perturbative unitary considerations of [180] are indicated by shading in the upper left corner.

As presented in Fig. 8 for the case of an axial-vector mediator, each resonance search analysis is sensitive to complementary regions of the mass-coupling parameter space. Couplings above the exclusion line are excluded, as long as the width predicted by the model is smaller than the maximal width over mediator mass ($\Gamma/m_{Z'}$) to which the analysis is sensitive. This limitation arises where the background model is estimated via a sliding-window fit of the m_{jj} distribution. Specifically, the TLA dijet analysis assuming $|y^*| < 0.6$ is sensitive up to $\Gamma/m_{Z'} = 7\%$, the TLA dijet assuming $|y^*| < 0.3$ and the boosted dijet+ISR analyses are sensitive up to $\Gamma/m_{Z'} = 10\%$, while the dijet and dibjet analyses are sensitive up to $\Gamma/m_{Z'} = 15\%$. Finally, the dijet angular analysis is sensitive up to $\Gamma/m_{Z'} = 50\%$. No limitation in sensitivity arises from large width resonances for the $t\bar{t}$ resonance analysis, as the background is constrained in dedicated control regions. The different dijet analyses (see Sec. 4.2 for details) are sensitive to different mass regimes as well as coupling values. The boosted dijet+ISR analyses has the best reach for low masses, excluding Z'_A mediator masses between 100 GeV and 220 GeV. Two new interpretations, for the dibjet and $t\bar{t}$ resonance analyses, are presented for these models. The dibjet ($t\bar{t}$ resonance) analysis places constraints for Z'_A mediators of masses between 500 GeV and 2.5(2) TeV, in the same region of sensitivity of the dijet, TLA dijet, boosted dijet+ISR analyses.

To illustrate the complementarity of dedicated searches to these different final states [39, 41], three different coupling scenarios are also considered in the interpretation of the results:

Scenario 1 $g_q = 0.25$, $g_\ell = 0$, $g_\chi = 1$ (leptophobic Z'_V/Z'_A);

Scenario 2 $g_q = 0.1$, $g_\ell = 0.01$, $g_\chi = 1$ (leptophilic Z'_V);

Scenario 3 $g_q = 0.1$, $g_\ell = 0.1$, $g_\chi = 1$ (leptophilic Z'_A).

In particular, the lower lepton coupling value is chosen to highlight the dilepton search sensitivity even for very small values of this parameter.

The exclusions from the resonance searches (dijet, dibjet, dilepton) in the $(m_{Z'_{V/A}}, m_\chi)$ plane are derived from the limits provided on resonances reconstructed with a Gaussian-shape, while the limits from the $E_{\mathrm{T}}^{\mathrm{miss}}+X$ and $t\bar{t}$ resonance analyses are derived using a mixture of simulated signal samples and re-scaling procedures as described in Sec. 3. For each scenario in Figs. 9 and 10, dashed curves labeled "thermal relic" indicate combinations of DM and mediator mass that are consistent with a DM density of $\Omega h^2 = 0.12$ and a standard thermal history, as computed in MadDM [41, 179]. Between the two curves, annihilation processes described by the simplified model deplete the relic density below the thermal value. A dotted line indicates the kinematic threshold where the mediator can decay on-shell into DM particles. Excluded regions that are in tension with the perturbative unitary considerations of Ref. [180] are indicated by shading.

The sensitivity reach of the various experimental signatures for the leptophobic vector mediator scenario as a function of the DM and mediator masses is summarised in Fig. 9(a). Due to the relatively high choice for the universal quark coupling with respect to other benchmarks, the strongest limits are obtained from the resonance searches. These analyses are sensitive to mediator masses between 200 GeV and 2.5 TeV with little dependence on the DM mass. A reduction in the exclusion reach is observed at high mediator masses and for $200 < m_{Z'_V} < 450$ GeV when $m_{Z'_V} > 2m_\chi$, due to the opening of the $Z'_V \to \chi\bar{\chi}$ decay channel. The boosted dijet + ISR search is not reinterpreted here but has sensitivity in this region. The lower mass limit is determined by the trigger requirements of the resolved dijet + ISR analysis. For $m_{Z'_V} < 2m_\chi$, masses up to 2.9 TeV are excluded by the resolved dijet + ISR, dijet TLA and dijet searches. Compared to the dijet searches, the $t\bar{t}$ resonance analysis is particularly sensitive to the change in effective cross-section due to reduction in branching ratio, as it can be inferred from the coupling reach of Fig. 8. Conversely,

the sensitivity of the $E_{\mathrm{T}}^{\mathrm{miss}}+X$ signatures is highest in the region $m_{Z'_V} > 2m_\chi$, up to mediator masses of 1.5 TeV and providing a unique coverage for masses below 500 GeV. The sensitivity of these analyses is strongly decreased for $m_{Z'_V} < 2m_\chi$, where the DM particles are produced off-shell, with a consequent strong reduction of the production cross-section. For this reason only the jet+$E_{\mathrm{T}}^{\mathrm{miss}}$ and $\gamma + E_{\mathrm{T}}^{\mathrm{miss}}$ analyses can probe the off-shell regime for this benchmark scenario, and only in the case of very low mediator and DM masses. It is important to highlight that if the value chosen for g_q were reduced, the relative interplay between the dijet and the $E_{\mathrm{T}}^{\mathrm{miss}}+X$ searches would change, as exemplified by the change of the dijet limit in the different couplings scenarios described in the following.

The experimental limits for the leptophilic vector-mediator model are summarised in Fig. 9(b). In this case, the mediator decay rates to quarks are reduced in favour of a higher branching ratio to DM particles, reducing the sensitivity of dijet searches to this scenario, whereas the leptonic branching ratio allows dilepton searches to also impose constraints for a wide range of mediator masses. This benchmark highlights the complementarity between dijet, dilepton and $E_{\mathrm{T}}^{\mathrm{miss}}+X$ final states. In this case, dibjet and $t\bar{t}$ resonance searches are not included in the final result. The resonant searches exclude mediator masses between 150 GeV and 2 TeV (except for a small gap around 1.7 TeV), if $m_{Z'_V} < 2m_\chi$ and between 150 and 350 GeV for all DM masses. Complementarily, the $E_{\mathrm{T}}^{\mathrm{miss}}+X$ final states exclude mediator masses up to 1 TeV for $m_{Z'_V} > 2m_\chi$.

Similar considerations can be made for the axial-vector mediator models, presented in Figs. 10(a) and 10(b), with the exception that in the presence of non-vanishing coupling to leptons (leptophilic scenario), chosen higher than the vector case, the dilepton resonance search becomes by far the most sensitive analysis for this model, excluding the mass range 150 GeV $< m_{Z'_V} <$ 2.8 TeV for any DM mass. Also in this case, the sensitivity of this analysis increases when the $Z'_V \to \chi\bar{\chi}$ is kinematically forbidden and becomes independent of the DM mass above threshold. For $m_{Z'_V} < 2m_\chi$, masses up to 3.5 TeV are excluded.

Collider experiments represent a complementary approach to DM searches with respect to direct and indirect detection experiments [40]. It is therefore interesting and informative, though model-dependent, to compare the V/AV limits with the results from other DM searches . Figure 11 shows the translation of the V/AV model limits into limits on the spin-dependent χ-proton and spin-independent χ-nucleon scattering cross-sections as a function of the DM mass. The direct detection experiments dominate the sensitivity by few orders of magnitude for DM masses above 10 GeV, thanks to the fact that due to a coherence effect, the spin-independent interaction cross-section with heavy nuclei is enhanced by A^2, where A is the number of nucleons in a nucleus, and dominates the interaction in this model. However, with the assumed coupling strengths, the analyses presented in this note allow to complement direct detection limits in the low DM mass range where the direct DM search experiments have less sensitivity due to the very low-energy recoils that such low-mass DM particles would induce. The lower edge of the sensitivity contour for all analyses in Fig. 11(a) (Fig. 11(b)) is driven by the high-mass reach of each analysis in Fig. 9(a) (10(b)), the scattering cross-section limit is inversely proportional to the mediator mass reach (raised to the fourth power). Conversely the upper edge of the scattering cross-section contour for the dijet and dilepton analyses is driven by their low-mass sensitivity limit due to the trigger requirements employed in these analyses. Further details on this comparison are discussed in Appendix B.

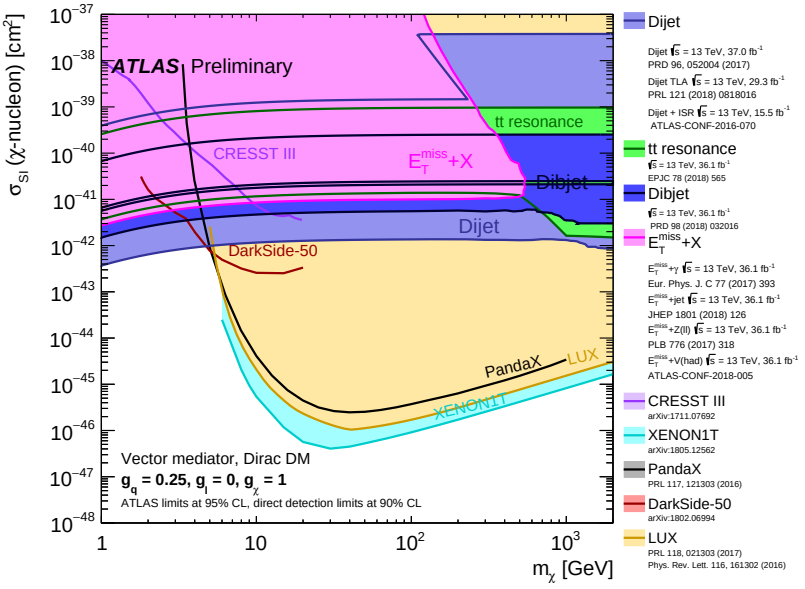

(a)

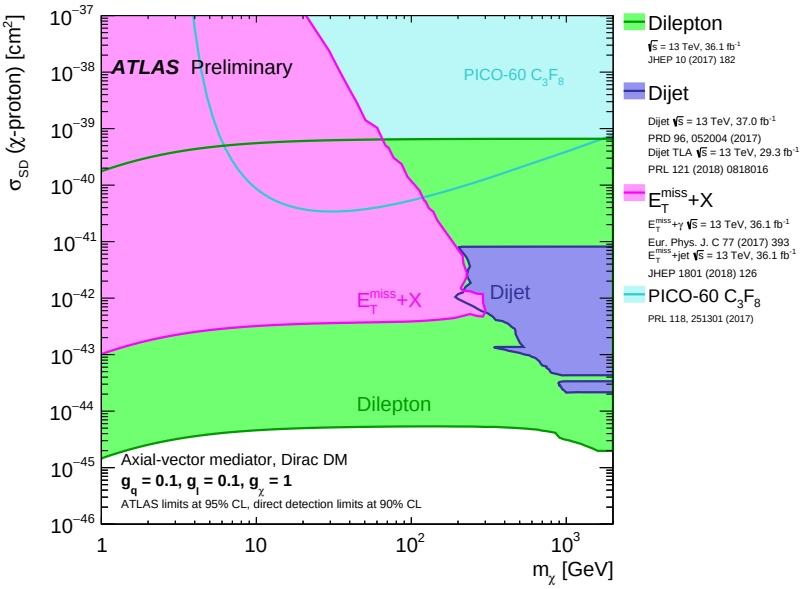

(b)

Figure 11: A comparison of the inferred limits to the constraints from direct detection experiments on the spin-dependent WIMP-proton scattering cross-section in the context of the vector leptophobic model (a) and on the spin-independent WIMP-nucleon scattering cross-section in the context of the axial-vector leptophilic model (b). The results from this analysis, excluding the region inside or to the left of the contour, are compared with limits from direct detection experiments. ATLAS limits are shown at 95% CL and direct detection limits at 90% CL. ATLAS searches and direct detection experiments exclude the shaded areas. Exclusions beyond the canvas are not implied for the ATLAS results. The dijet and $E_{\mathrm{T}}^{\mathrm{miss}}$ +X exclusion regions represent the union of exclusions from all analyses of that type.

6.1.2 Baryon-charged interaction

In the context of the VBC model, the results from the $h(\gamma\gamma) + E_{\mathrm{T}}^{\mathrm{miss}}$and the $h(b\bar{b}) + E_{\mathrm{T}}^{\mathrm{miss}}$ analysis are interpreted in the plane formed by the Z'_B and DM masses, due to the characteristic signature of this model involving Higgs-strahlung from the Z'_B mediator. The $h(b\bar{b}) + E_{\mathrm{T}}^{\mathrm{miss}}$ interpretation is new with respect to the original publication [23]. The results are shown in Fig. 12 in the $(m_{Z'_B}, m_\chi)$ plane for $g_q = 1/3$, $g_\chi = 1$ and $\sin\theta = 0.3$. The dashed lines indicate the expected exclusion contours from the two separate channels and their combination (based on best expected limits), while the black solid line shows the observed exclusion, presented only for the combined result. The green band around the expected combined contour shows the effect of one σ variation of the total systematic uncertainties. The $h(b\bar{b}) + E_{\mathrm{T}}^{\mathrm{miss}}$ analysis sets the strongest bounds in this model, excluding mediator masses up to 1900 GeV for all DM mass hypotheses such that the mediator invisible decay is kinematically allowed. Due to the lower branching ratio, the $h(\gamma\gamma) + E_{\mathrm{T}}^{\mathrm{miss}}$ is less sensitive to this model for high-mediator masses, despite this, it recovers some sensitivity for $m_{Z'_B} < 50$ GeV.

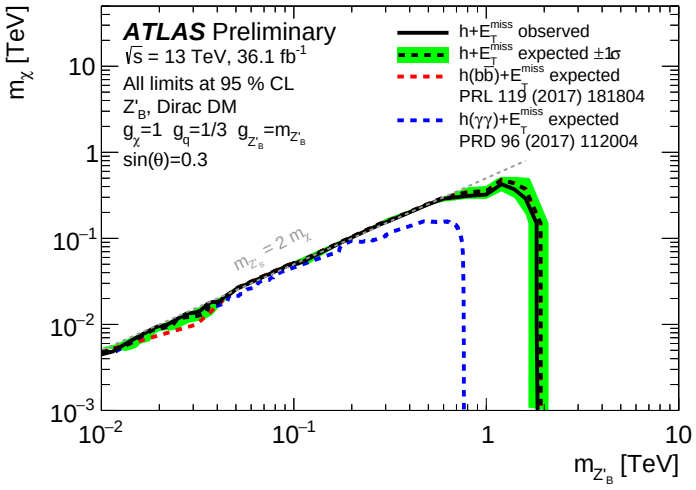

Figure 12: Exclusion contours for the VBC model in the $(m_{Z'_B}, m_\chi)$ plane for $g_q = 1/3$, $g_\chi = 1$ and $\sin\theta = 0.3$. The blue, red and black dashed lines indicate the expected exclusion contours from the two separate channels and their combination, while the black solid line shows the observed exclusion, presented only for the combined result. The green band around the expected combined contour shows the effect of a one σ variation of the total systematic uncertainties on the background and on the signal acceptance.

6.2 Scalar or pseudo-scalar dark matter models

6.2.1 Colour-neutral interaction

The most stringent limits on S/PS models are obtained from $t\bar{t} + E_{\mathrm{T}}^{\mathrm{miss}}$ final states, which are studied in three channels assuming fully-hadronic, semi-leptonic and fully-leptonic top pair decays, respectively. The fully-leptonic channel excludes scalar-mediator models with unitary couplings $g_\chi = g_q = g = 1$ up to mediator masses of 45 GeV, setting in this mass range the strongest upper limits on the ratio of the signal production cross-section to the nominal cross-section (signal strength or $\sigma/\sigma(g = 1.0)$), as shown in Fig. 13(a). In the case of pseudo-scalar mediator models (Fig. 13(b)), similar sensitivity is obtained by all

channels and mediator masses in the range 15–25 GeV are excluded. In all cases, a DM mass of 1 GeV is assumed, but the results are valid for all DM mass choices such that the mediator decay into a pair of DM particles is kinematically allowed ($m_{\phi/a} > 2m_{\chi}$). Pseudo-scalar mediator models can also be constrained by jet+$E_{\mathrm{T}}^{\mathrm{miss}}$ final states, where the mediator is produced through loop-induced gluon fusion. Although the limits obtained by this signature are not competitive with the $t\bar{t}$ +$E_{\mathrm{T}}^{\mathrm{miss}}$ final state, except in the mass range above 300 GeV, they provide a complementary constraint, that would become particularly important in the case of a discovery. For the scalar model, the jet+$E_{\mathrm{T}}^{\mathrm{miss}}$ final states cross-section is instead too small to be probed. Ditop resonance searches in final states with two and four tops can also constrain this parameter space for $m_{\phi/a} > 2m_t$. However, $t\bar{t}$ production through a spin-0 resonance presents a strong interference pattern with SM top pair production [181], which needs to be treated with care. On the other hand, four top final states are characterised by relatively low event yields with the current available integrated luminosity. For these reasons the study of these final states is not considered here. Finally, $b\bar{b}$ +$E_{\mathrm{T}}^{\mathrm{miss}}$ final states are also used to set constraints on these simplified models, resulting in upper limits on the signal strength between 200 and 300. These results quantify the sensitivity to these models if up-type couplings are suppressed.

6.2.2 Colour-charged interaction

The strongest exclusion limits on colour charged mediators η_q that couple to first and second generations left-handed quarks are set by the jet+$E_{\mathrm{T}}^{\mathrm{miss}}$ analysis. Assuming a unitary coupling, η_q mediator masses up to 1.7 TeV are excluded for $m_{\chi} = 50$ GeV. Furthermore, η_q mediator masses below 600 GeV are excluded for all DM masses such that the decay $\eta_q \rightarrow q\chi$ is kinematically allowed. The strongest exclusion limits on colour charged mediators η_b that couple to third generation right-handed b-quarks are set by the $b + E_{\mathrm{T}}^{\mathrm{miss}}$ analysis. Assuming a coupling set to the value that yields a relic density value consistent with astrophysical observations, masses up to 1.4 TeV are excluded for $m_{\chi} = 1$ GeV.

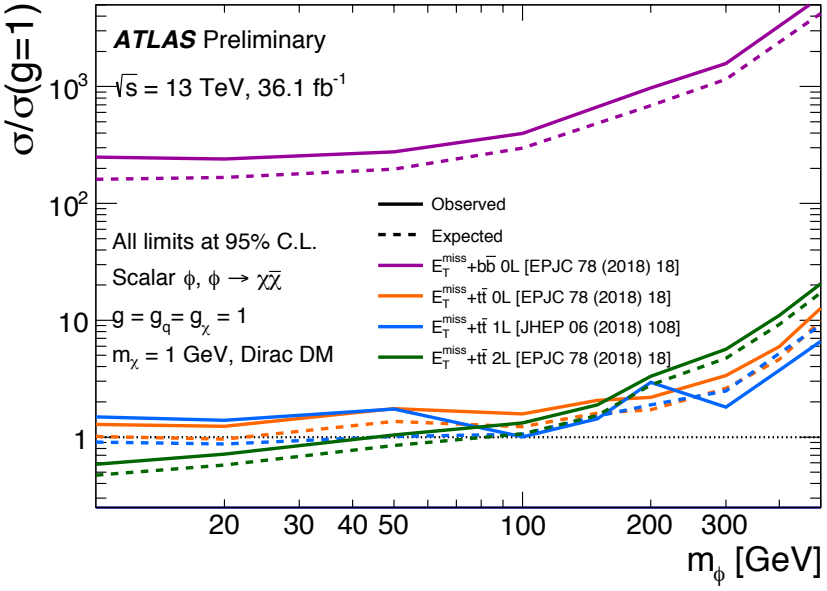

(a)

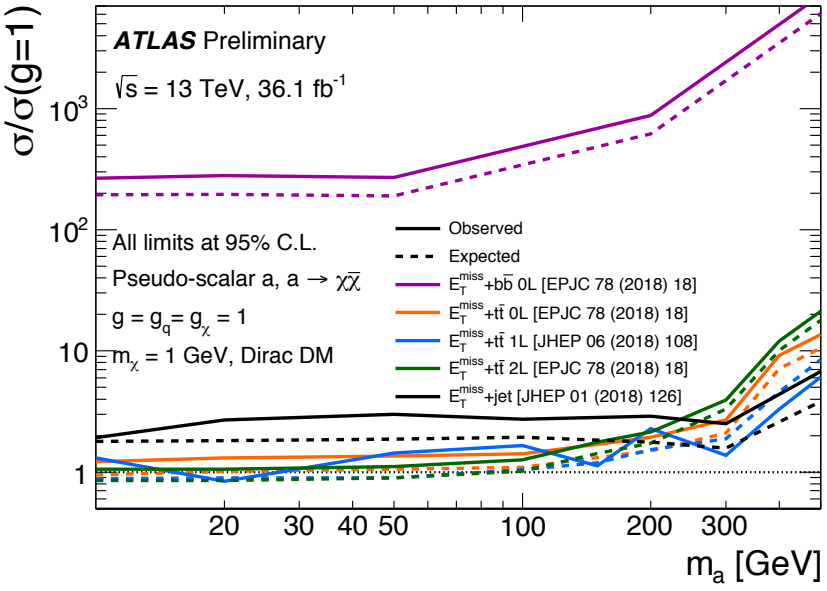

(b)

Figure 13: Exclusion limits for colour-neutral scalar (a) or pseudo-scalar (b) mediator models as a function of the mediator mass for a DM mass of 1 GeV. The limits are calculated at 95% CL and are expressed in terms of the ratio of the excluded cross-section to the nominal cross-section for a coupling assumption of $g = g_q = g_\chi = 1$. The solid (dashed) lines show the observed (expected) exclusion limits for each channel.

6.3 Extended Higgs sector dark matter models

6.3.1 Two-Higgs-doublet models with a vector mediator

The 2HDM+Z'_V model is constrained by the $h(b\bar{b}) + E_{\mathrm{T}}^{\mathrm{miss}}$ and $h(\gamma\gamma) + E_{\mathrm{T}}^{\mathrm{miss}}$ analyses. The results are interpreted in terms of exclusion limits in the $(m_A, m_{Z'_V})$ plane, shown in Fig. 14. The statistical combination of the two analyses is also presented. Masses of the pseudo-scalar A in the range 200 – 600 GeV are excluded for $m_{Z'_V} = 1.5$ TeV. The limit in sensitivity is driven by the fact that the $A \to \chi\bar{\chi}$ branching ratio decreases with increasing m_A due to decay channels involving top quarks or other heavy bosons of the extended Higgs sector becoming accessible ($t\bar{t}$, HZ and $W^{\pm}H^{\mp}$). At higher $m_{Z'_V}$ the loss in branching ratio is combined with the smaller production cross-section such that the reach of the analysis is limited to smaller pseudo-scalar masses. For $m_A < 2m_t$ and $m_A > 2 \times m_\chi$, there are no more competing decay channels and the reach of the analysis does not depend anymore on m_A. This creates the turn in the exclusion contour for $m_{Z'_V} = 2.5$ GeV.

The two $h + E_{\mathrm{T}}^{\mathrm{miss}}$ decay signatures are highly complementary at low Z'_V masses, as it can be observed in the zoomed inset in the figure, while the $h(b\bar{b}) + E_{\mathrm{T}}^{\mathrm{miss}}$ analysis dominates the sensitivity at high Z'_V masses. Due to this complementarity, the gain obtained by the statistical combination of the two signatures is limited to the low mass region for this model.

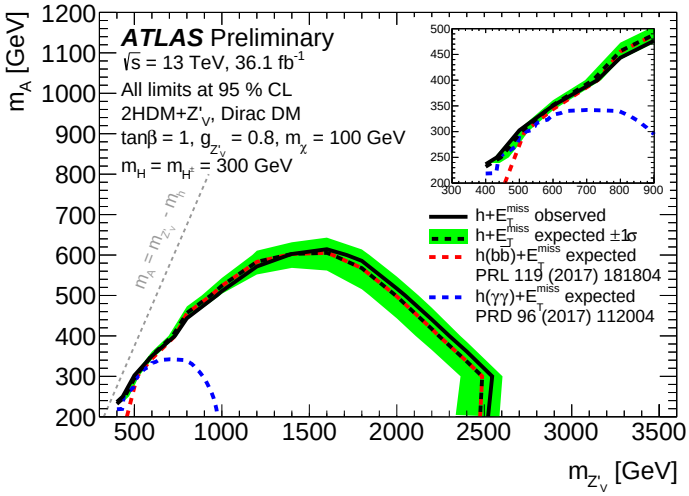

Figure 14: Exclusion contours for the Z'-2HDM scenario in the $(m_{Z'_V}, m_A)$ plane for $\tan\beta = 1$, $g_{Z'_V} = 0.8$ and $m_\chi = 100$ GeV. The blue, red and black dashed lines indicate the expected exclusion contours from the two separate channels and their statistical combination, while the black solid line shows the observed exclusion, presented only for the combined result. The green band around the expected combined contour shows the effect of a one σ variation of the total systematic uncertainties. The sharp turn in the exclusion contour for $m_{Z'_V} = 2.5$ GeV is given by the opening of decay channels of the A-boson competing with the considered final state for $m_A > 2m_t$. For this reason the exclusion sensitivity does not depend on m_A below threshold. The inset in the top-right side of the panel shows a zoomed version of the result for low $m_{Z'_V}$ masses to highlight the complementarity between the $h(b\bar{b}) + E_{\mathrm{T}}^{\mathrm{miss}}$ and the $h(\gamma\gamma) + E_{\mathrm{T}}^{\mathrm{miss}}$ analyses in this parameter region.

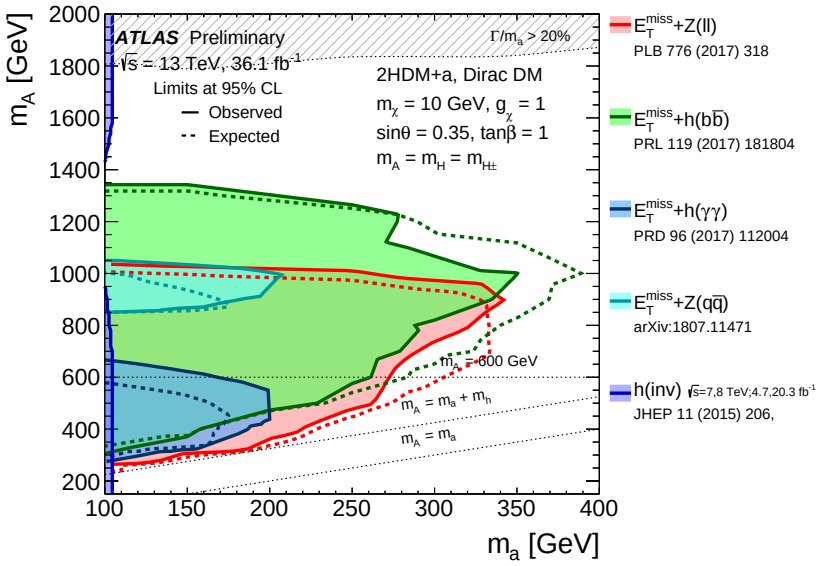

(a)

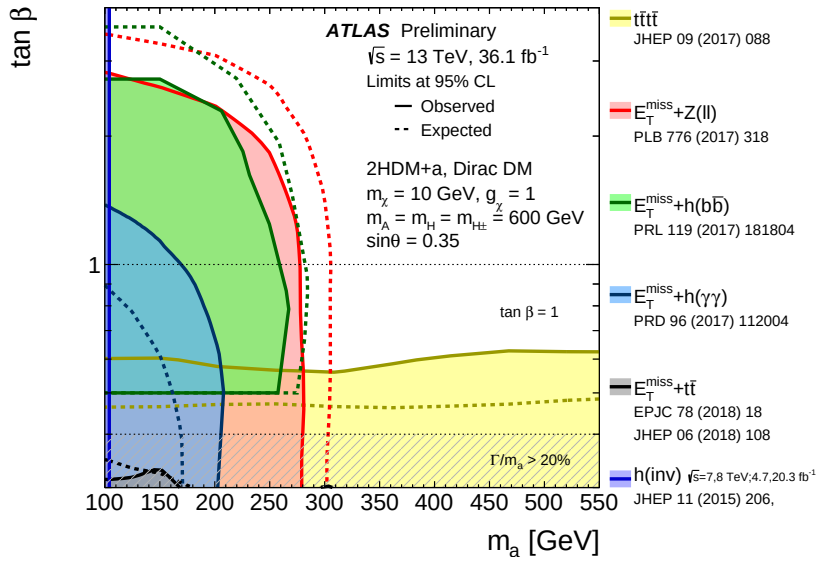

(b)

Figure 15: Regions in a (m_a, m_A) (a) and $(m_a, \tan\beta)$ (b) planes excluded by data at 95% CL by $X + E_{\mathrm{T}}^{\mathrm{miss}}$ and four top analyses, following the parameter choices of scenarios 1 and 2 of the 2HDM+a model. The dashed grey regions at the top of (a) and the bottom of (b) indicate the region where the width of any of the Higgs bosons exceeds 20% of its mass. The exclusion limits presented above conservatively neglect the contribution from $b\bar{b}$ initiated production, which might be sizeable for $\tan\beta \geq 3$ for the $Z + E_{\mathrm{T}}^{\mathrm{miss}}$ channel and, to a lesser extend, for the $h + E_{\mathrm{T}}^{\mathrm{miss}}$ one.

6.3.2 Two-Higgs-doublet models with a pseudo-scalar mediator

As highlighted in Sec. 2.3.2, the 2HDM+a model is characterised by a rich phenomenology. Constraints on this model from ATLAS searches are presented for the first time in this note. Four different benchmark scenarios are used to evaluate the sensitivity to this model of the $Z/h + E_{\mathrm{T}}^{\mathrm{miss}}$, $t\bar{t}/b\bar{b}$+$E_{\mathrm{T}}^{\mathrm{miss}}$, h(inv), and $t\bar{t}t\bar{t}$ analyses. These four benchmark scenarios [42] are consistent with bounds from electroweak precision, flavour and Higgs observables and are chosen to highlight the complementary importance of the various final states. These scenarios represent two-dimensional and one-dimensional scans of a five-dimension parameter space, used to present the exclusion limits.

Scenario 1 (m_a, m_A) exclusion plane assuming $\tan\beta = 1$ and $\sin\theta = 0.35$;

Scenario 2 $(m_a, \tan\beta)$ exclusion plane assuming $m_A = 600$ GeV and $\sin\theta = 0.35$;

Scenario 3 $\sin\theta$ exclusion scan assuming

a) $m_A = 600$ GeV , $m_a = 200$ GeV and $\tan\beta = 0.5$, 1 or 50.

b) $m_A = 1000$ GeV , $m_a = 350$ GeV and $\tan\beta = 0.5$ or 1

Scenario 4 m_χ exclusion scan assuming $m_A = 600$ GeV, $m_a = 250$ GeV, $\tan\beta = 1$, $\sin\theta = 0.35$.

In all cases, the masses of the heavy pseudoscalar, heavy scalar, and charged bosons are kept equal ($m_A = m_H = m_{H^\pm}$). As visible in the results presented in Fig. 15(a), the exclusion sensitivity is vastly dominated by the $h(b\bar{b}) + E_{\mathrm{T}}^{\mathrm{miss}}$ and the $Z(\ell\ell) + E_{\mathrm{T}}^{\mathrm{miss}}$ analyses in the first scenario. These analyses are mostly sensitive to the production diagrams of Figs. 6(d) and 6(e) and their sensitivity depends on both pseudo-scalar mediator masses. The maximum reach is obtained for light pseudo-scalar m_a up to 340 GeV, if the A boson mass is set to 1 TeV, while for $m_a = 150$ GeV A boson masses between 280 GeV and 1.35 TeV are excluded. The combined contours of the $h(b\bar{b}) + E_{\mathrm{T}}^{\mathrm{miss}}$ and $Z(\ell\ell) + E_{\mathrm{T}}^{\mathrm{miss}}$ analyses include the $h(\gamma\gamma) + E_{\mathrm{T}}^{\mathrm{miss}}$ and $Z(q\bar{q}) + E_{\mathrm{T}}^{\mathrm{miss}}$ exclusion areas, although $h(\gamma\gamma) + E_{\mathrm{T}}^{\mathrm{miss}}$ analysis still complements $h(b\bar{b}) + E_{\mathrm{T}}^{\mathrm{miss}}$ at low (m_a, m_A) values. Finally, the h(inv) branching ratio limit constrains very low values of m_a for m_A mass below 900 GeV and above 1.4 TeV, being only sensitive to the a boson production cross-section.

In the context of 2HDM models, it is customary to investigate the sensitivity in terms of the $\tan\beta$ parameter. This is achieved in the second scenario presented in Fig. 15(b). Although the exclusion reach is dominated also in this case by the $h(b\bar{b}) + E_{\mathrm{T}}^{\mathrm{miss}}$ and $Z(\ell\ell) + E_{\mathrm{T}}^{\mathrm{miss}}$ analyses, two additional signatures contribute at $\tan\beta \sim 0.5$: the $t\bar{t}$ +$E_{\mathrm{T}}^{\mathrm{miss}}$ and the $t\bar{t}t\bar{t}$ analyses. The sensitivity of the former analysis is driven by the production cross-section of the a mediator in association with a top-pair and it decreases when the decay of the light pseudo-scalar into a top-quark pair is kinematically allowed and competes with $a \to \chi\bar{\chi}$. On the other hand the sensitivity of the latter analysis is fairly independent on m_a due to the contribution to the total four top production cross-section of the heavy bosons $H/A \to t\bar{t}$, both of which have masses fixed to 600 GeV in this scenario. In the case of the $h(b\bar{b}) + E_{\mathrm{T}}^{\mathrm{miss}}$ analysis, the exclusion was not investigated below $\tan\beta = 0.5$. Given the non trivial dependency of the width with respect to $\tan\beta$ in this channel, it is not possible to do an extrapolation beyond the area explored.

Figures 16(a) and 16(b) present the exclusion limits dependence on the mixing angle, $\sin\theta$, for a low-mass and high-mass a assumption, as considered in the third scenario. The limits are expressed in terms of the ratio of the excluded cross-section to the nominal cross-section of the model. For scenario 3a (Fig. 16(a)), the lowest cross-section values are excluded by the $Z(\ell\ell) + E_{\mathrm{T}}^{\mathrm{miss}}$ and $h(b\bar{b}) + E_{\mathrm{T}}^{\mathrm{miss}}$ analyses. The sensitivity of both $Z + E_{\mathrm{T}}^{\mathrm{miss}}$ analyses monotonically improves as a function of $\sin\theta$, as the cross-section

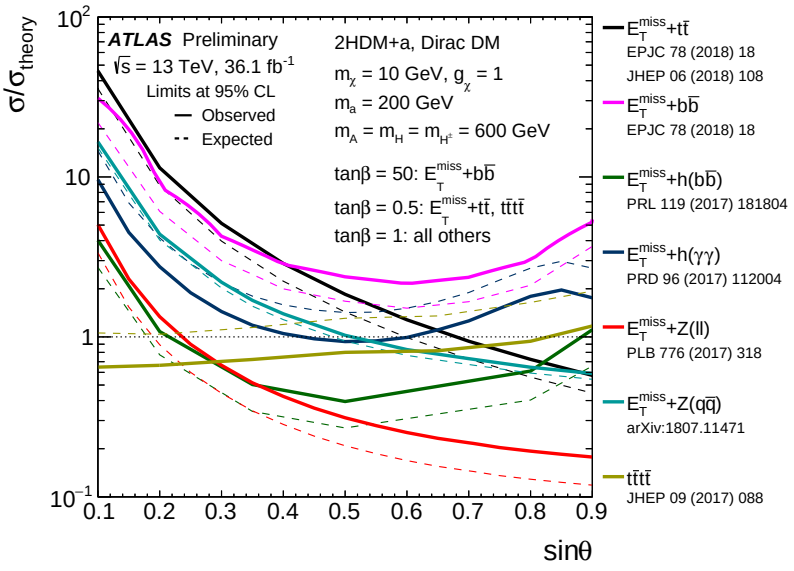

(a)

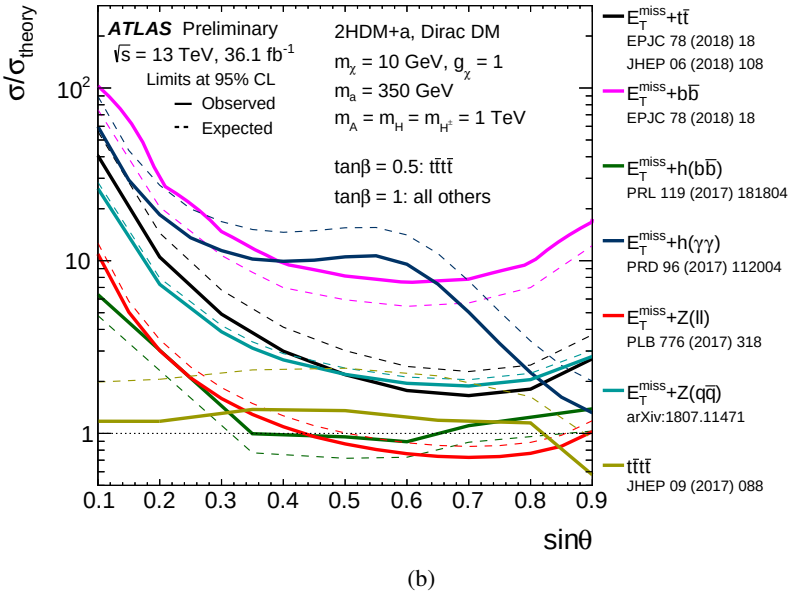

(b)

Figure 16: Observed exclusion limits for the 2HDM+a model as a function of $\sin\theta$, following the two parameter choices of scenario 3. The limits are calculated at 95% C.L. and are expressed in terms of the ratio of the excluded cross-section to the nominal cross-section of the model.

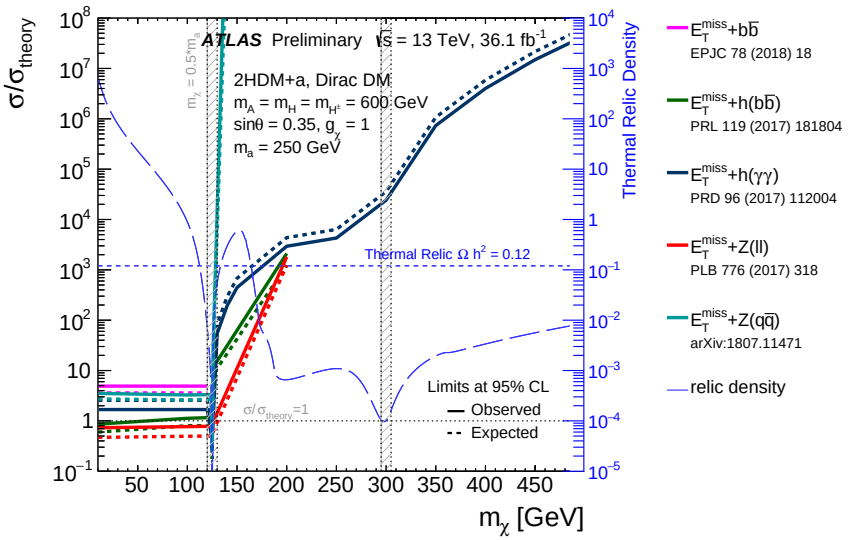

Figure 17: Observed exclusion limits for the 2HDM+a model as a function of m_χ, following the parameter choices of scenario 4. The limits are calculated at 95% C.L. and are expressed in terms of the ratio of the excluded cross-section to the nominal cross-section of the model. The relic density for each m_χ assumption is superimposed in the plot (long-dashed blue line) and described by the right y-axis. For DM mass values where the relic density line is below $\Omega h^2 = 0.12$, the model depletes the relic density below the thermal value. The two valleys at $m_\chi = 125$ GeV and $m_\chi = 300$ GeV determine the two a-funnel and A-funnel regions [42, 182, 183] where the predicted relic density is depleted by the resonant enhancement of the processes $\chi\bar{\chi} \to A/a \to$ SM.

of non-resonant and resonant production diagrams, in Figs. 6(d) and 6(e) respectively, increase with $\sin\theta$. Conversely, the same production diagrams for the $h + E_{\mathrm{T}}^{\mathrm{miss}}$ signatures have very different dependence on the mixing angle [120] in the two m_a regimes explored here. The contribution of each diagram is also affected by the different $h(b\bar{b}) + E_{\mathrm{T}}^{\mathrm{miss}}$ and $h(\gamma\gamma) + E_{\mathrm{T}}^{\mathrm{miss}}$ analyses selections. For this scenario, both analyses have maximum of sensitivity around $\sin\theta \sim 0.5$. The three heavy flavour signatures, $b\bar{b} + E_{\mathrm{T}}^{\mathrm{miss}}$, $t\bar{t} + E_{\mathrm{T}}^{\mathrm{miss}}$ and $t\bar{t}t\bar{t}$, are presented for different $\tan\beta$ assumptions. A value of $\tan\beta = 50$ is considered for $b\bar{b} + E_{\mathrm{T}}^{\mathrm{miss}}$, with the aim to probe the parameter space where the coupling of the a mediator to down-type quarks is enhanced. However, the $t\bar{t} + E_{\mathrm{T}}^{\mathrm{miss}}$ and $t\bar{t}t\bar{t}$ signatures are presented for $\tan\beta = 0.5$ as they are not yet able to probe $\tan\beta$ values near unity. The $t\bar{t}t\bar{t}$ signature, in particular, shows a $\sin\theta$ dependence complementary to the other signatures due to the combined contribution of all neutral bosons decay to top-pairs and is particularly sensitive very small mixing angles. Scenario 3b, presented in Fig. 16(b) sets the mass of the light pseudo-scalar such that the $a \to t\bar{t}$ decay is kinematically allowed, which introduces an additional θ dependence to the $X + E_{\mathrm{T}}^{\mathrm{miss}}$ analyses interpreted in this scenario. For this reason, the highest sensitivity for each analysis is found to be broadly around (or slightly below) the maximal mixing condition ($\theta = \frac{\pi}{4}$), except for the $t\bar{t}t\bar{t}$ and $h + E_{\mathrm{T}}^{\mathrm{miss}}$ signatures. The $t\bar{t}t\bar{t}$ signature shows a flat sensitivity as a function of $\sin\theta$ (with an increase for very high value) due to the mass assumptions of this scenario ($m_a = 350$ GeV and $m_{A/H} = 1$ TeV) which cause the $t\bar{t}t\bar{t}$ production cross-section to be completely dominated by the $t\bar{t} + a(tt)$ process. The $h + E_{\mathrm{T}}^{\mathrm{miss}}$ signatures have a complex dependence on the mixing angle. This is due to the different contributions of resonant and non-resonant processes to the final selection of the two analyses. In this case it is possible to observe that the $h(b\bar{b}) + E_{\mathrm{T}}^{\mathrm{miss}}$ analysis presents a maximum in sensitivity around the maximal mixing condition. The $h(\gamma\gamma) + E_{\mathrm{T}}^{\mathrm{miss}}$ analysis instead shows a local minimum around $\sin\theta \sim 0.55$.

Finally, Fig. 17 presents the reach of the various experimental searches in a cosmological perspective,

following the prescription of the fourth benchmark scenario. In this case, the observed exclusion limits in terms of of the ratio of the excluded cross-section to the nominal cross-section of the model are investigated as a function of the DM mass, which is the parameter with the strongest impact on the relic density predicted by the 2HDM+a. The region beyond $m_\chi = 200$ GeV was not explored by the $h(b\bar{b}) + E_{\mathrm{T}}^{\mathrm{miss}}$ and $Z(\ell\ell) + E_{\mathrm{T}}^{\mathrm{miss}}$ analyses, thus exclusions are not shown. For the same reason, the $b\bar{b} + E_{\mathrm{T}}^{\mathrm{miss}}$ exclusion is not shown beyond $m_\chi = 125$ GeV. The blue solid line indicates the computed relic density for the 2HDM+a model as a function of the DM mass. The two valleys at $m_\chi = 125$ GeV and $m_\chi = 300$ GeV determine the two a-funnel and A-funnel regions [42, 182, 183] where the predicted relic density is depleted by the resonant enhancement of the processes $\chi\bar{\chi} \to A/a \to$ SM. The plateau around and above $m_\chi \sim 200$ GeV is determined by the increase in annihilation cross-section of the DM particles close to threshold for $\chi\bar{\chi} \to ha \to$ SM and $\chi\bar{\chi} \to t\bar{t}$. For DM masses around $\frac{1}{2}m_a$ or $m_\chi > 170$ GeV the model predicts a relic density which is equal or below the thermal value, $\Omega h^2 = 0.12$. As the DM mass increases further, annihilation via single s-channel diagrams is more and more suppressed and the observed DM relic density can again be reproduced. At low values of m_a this happens around $m_\chi \sim 10$ TeV and is outside the range considered in Fig. 17. For all $X + E_{\mathrm{T}}^{\mathrm{miss}}$ signatures considered, the sensitivity is independent of the DM mass as long as the lightest pseudo-scalar mediator, whose mass is fixed at 250 GeV in this scenario, is allowed to decay into a $\chi\bar{\chi}$-pair. The $Z(\ell\ell) + E_{\mathrm{T}}^{\mathrm{miss}}$ analysis excludes this parameter space. For higher DM masses, the sensitivity of all analyses quickly decreases and no exclusion is observed. For $m_\chi > \frac{1}{2}m_a$ all parameter choices that fulfil or deplete the relic density value are still unconstrained.

7 Conclusions

This note summarises the lively experimental programme of searches for mediator-based particle dark matter performed by the ATLAS Collaboration. The analyses presented are based on up to 37 fb^{-1} of proton-proton collisions data at a centre of mass energy of $\sqrt{s} = 13$ TeV collected by the ATLAS detector in 2015 and 2016. The h(inv) analysis considers up to 4.7 fb^{-1} at centre of mass energy of $\sqrt{s} = 7$ TeV and 20.3 fb^{-1} at centre of mass energy of $\sqrt{s} = 8$ TeV. The measurements from those searches are in agreement with the Standard Model predictions, thus results are translated into exclusion limits on several mediator-based dark matter models.

Simplified models with the exchange of a vector or axial-vector mediator in the s-channel with Dirac fermions as dark matter candidates are studied. Leptophobic (leptophilic) vector and axial-vector mediator masses between 200 GeV and 2.5 TeV (3.5 TeV), for coupling values $g_q = 0.25$ and $g_\chi = 1$, and $m_\chi = 1$ TeV, are excluded at 95% CL. In the context of a baryon-charge interaction, masses of the Z'_B boson are excluded up to 1.9 TeV for $m_\chi = 1$ GeV and coupling values of $g_\chi = 1$ and $g_q = 1/3$.

A simplified model of dark matter production including a colour-neutral scalar (pseudo-scalar) mediator is considered, and mediator masses below 45 GeV (in the range 15 – 25 GeV) are excluded for dark matter particles with $m_\chi = 1$ GeV and $g_\chi = 1$. Masses for colour-charged mediators, coupling to first and second generation left-handed quarks, are excluded up to 1.7 TeV, for $m_\chi = 50$ GeV for $g_\chi = 1$. Colour-charged mediators that couple to right-handed b-quarks are excluded for masses up to 1.4 TeV for light dark matter masses.

Finally, an extended two-Higgs-doublet model with an additional pseudo-scalar, a, which couples the dark matter particles to the Standard Model is used to exploit the broad phenomenology with diverse final state signatures predicted by this type of model. Masses of the pseudo-scalar mediator, a, are excluded up to 350 GeV for $m_A = m_H = m_{H^\pm} = 1$ TeV, $\sin\theta = 0.35$ (mixing angle between a and A bosons)

and $\tan\beta = 1.0$. $Z(\ell\ell) + E_{\mathrm{T}}^{\mathrm{miss}}$ and $h(b\bar{b}) + E_{\mathrm{T}}^{\mathrm{miss}}$ searches are the most sensitive analyses in this high mediator mass region. Previously published limits on a two-Higgs-doublet model with an additional vector mediator are improved by the statistical combination of the two decay channels studied: $h(b\bar{b}) + E_{\mathrm{T}}^{\mathrm{miss}}$ and $h(\gamma\gamma) + E_{\mathrm{T}}^{\mathrm{miss}}$. Mediator masses between 400 GeV and 2.5 TeV are excluded for dark matter masses of 100 GeV.

Appendix

A Re-scaling details for signal models

A.1 Re-scaling details for V/AV models

For all V/AV models reconstructed samples were produced only for a specific reference scenario (either a vector or an axial-vector leptophobic mediator model). Re-scaling factors for the acceptance ($w_{\mathcal{A}}$) and the cross-section (w_{σ}) were calculated to match the acceptance and cross-section of each of the other scenarios with respect to the reference. The acceptance weights were calculated for each $(m_{Z'}, m_{\chi})$ mass pair point assumption as the ratio of the particle-level acceptance for each of the NLO benchmark models considered ($\mathcal{A}^{\text{NLO}}_{\text{truth}}$) to the particle-level acceptance of the analysis for the reference NLO scenario in a fiducial region ($\mathcal{A}^{\text{ref}}_{\text{truth}}$):

$$w_{\mathcal{A}}(m_{Z'}, m_{\chi}) = \frac{\mathcal{A}^{\text{NLO}}_{\text{truth}}(m_{Z'}, m_{\chi})}{\mathcal{A}^{\text{ref}}_{\text{truth}}(m_{Z'}, m_{\chi})} \tag{1}$$

The cross-section weights were calculated for each $(m_{Z'}, m_{\chi})$ mass assumptions in a similar way as the ratio of the reference cross-section at NLO to each cross-section of the four NLO benchmark models. The acceptance re-scaling weights were found to be consistent with unity for the $Z'(\chi\bar{\chi}) + j$ and $Z'(\chi\bar{\chi}) + \gamma$ signatures.

A few specific exceptions apply to this treatment. In case of the $Z'(\chi\bar{\chi}) + j$ signature, the cross-section re-scaling factors were calculated from LO samples (DMSimp [84] generated with MadGraph 2.4.3 (LO) [139]) and applied to the samples described in Table 2. In the specific case of the $Z'(\chi\bar{\chi}) + V$ signature, the baseline samples were generated at LO and re-scaled at particle-level to match the next-to-leading (NLO) samples described in the table. Finally, the exclusions from the resonance searches (dijet, dilepton, dibjet) as a function of the $(m_{Z'}, m_{\chi})$ interpretations are derived from the limits calculated for Gaussian-shaped resonances [140], and the samples in Table 2 are only used to derive the cross-section normalisation for the final results and the limits for the leptophobic Z'_A mediator models as a function of the universal coupling strength. The $Z'(t\bar{t})$ samples were obtained from the topcolour-assisted technicolour samples of [141] re-scaled at particle-level to match the DMSimp models described in Table 2. The correction weights between the two samples were calculated from the bin-by-bin ratio of the invariant mass distributions of the $t\bar{t}$ system for the two samples at particle-level. An additional uncertainty is assigned to account for this procedure as described in Sec. 5.

A.2 Re-scaling details for 2HDM+a models with heavy flavour final states

The $\chi\bar{\chi} + t\bar{t}/b\bar{b}$ signature of the $2HDM + a$ model can be successfully described [42] as the superposition of the associated production of two heavy flavour quarks with either the light or the heavy pseudo-scalar mediator, which subsequently decays into a $\chi\bar{\chi}$ pair. When the masses of the two pseudo-scalar mediators are sufficiently apart, the contributions of the two processes can be factorised, and the $2HDM + a$ model can be described in terms of two sets of colour-neutral pseudo-scalar simplified models, each corresponding to the desired choice for m_a and m_A.

The acceptance $\mathcal{A}$ of the analysis for each point of interest in the 2HDM+a parameter space is therefore derived as:

$$\mathcal{A}_{\text{2HDM}}(m_A, m_a) = \frac{\sigma_a \times \mathcal{A}_{\text{simp}}(m_a) + \sigma_A \times \mathcal{A}_{\text{simp}}(m_A)}{\sigma_a + \sigma_A}, \tag{2}$$

where $\mathcal{A}_{\text{simp}}$ is the acceptance of the analysis for the colour-neutral pseudo-scalar simplified model for a certain mass choice of the $A(a)$-boson, and σ_a and σ_A are the production cross-sections for $pp \to t\bar{t}a(\to \chi\bar{\chi})$ and $pp \to t\bar{t}A(\to \chi\bar{\chi})$, respectively[4]. This re-scaling is valid in the on-shell region, $m_a(m_A) > 2m_\chi$ [42].

B Comparison with direct and indirect searches

Searches for weakly-interactive massive particles (WIMPs) [37] represent the current paradigm for searches for particle dark matter (DM). Within this paradigm, understanding the nature of DM requires to measure its interaction cross-section with Standard Model particles. This can be achieved using three complementary methods [184], schematically depicted in Figure 18 and briefly outlined in the following.

Direct Searches These searches aim to measure the elastic scattering of DM with nuclei in low background underground detectors such as CRESST-II [6], LUX [7], PICO [8], DEAP [9], PandaX [10], XENON [11, 12], SuperCDMS [13, 14]. These direct detection experiments ultimately measure the strength of the interactions between WIMPs and the parton composing protons and neutrons and are sensitive to the properties of the DM halo around Earth.

Indirect Searches These searches aim to measure the annihilations or decays of DM particles in astrophysical systems, by means of neutrino detectors such as SuperKamiokande [15] or IceCube [16] or by means of either ground or space telescopes, as for example H.E.S.S. Cherenkov telescope [17, 18] and Fermi-LAT [19]. This measurement closely relates to the processes that set the abundance of DM in the early universe and the interpretation of the results depends on the DM distribution in the Universe as well as what SM particles the DM preferentially annihilates or decays into.

Collider Searches These searches aim to measure the DM production cross-section through collisions of high-energy particles. The most stringent results to date on WIMPs are provided by the ATLAS [20–29], CMS [30–34] and LHCb [185, 186] experiments at the LHC. Sub-GeV DM candidates are also constrained by the MiniBooNE experiment at Fermilab [187]. The interpretation of these results closely depends on the underlying mechanisms that couples DM to SM particles. In the simplified model framework considered in this note this underlying mechanism is assumed to be the production of new mediator(s) state(s) which consequently decay into DM.

Our current understanding of the DM puzzle is encompassed in the summary and comparison of the experimental results of these three approaches. Likewise, the discovery of DM as an elementary particle will require to measure its interaction cross-section with SM particles via each of these methods. It is convenient and customary to compare these different approaches in terms of spin-dependent (spin-independent)

[4] The procedure is also valid for $pp \to b\bar{b}a/A$ production. However the impact of the correction was found to be minimal [42] and is neglected in this paper.

χ-nucleon scattering cross-sections as a function of the DM mass. In this note, we convert the ATLAS exclusion limits into bounds on the χ-nucleon scattering cross-sections for the following models considered in this note:

- Vector and axial-vector neutral (V/AV) mediator models (two coupling scenario, see Sec. 6.1.1 for details).
- Vector baryon-charged (VBC) mediator model.
- Scalar colour-neutral mediator model.

For each given mediator model, the translation procedure to convert and compare these limits is well defined and described in Ref. [40]. The interpretation in the spin-dependent (SD) and spin-independent (SI) cross-sections, σ_{SD} and σ_{SI}, respectively, depends on the mediator mass and the couplings assumptions. Each comparison is valid solely in the context of the specific model and couplings assumptions. The ATLAS limits are always shown at 95% confidence level (CL) and the direct detection limits at 90% CL.

ATLAS exclusion limits for pseudo-scalar colour-neutral mediator models should be compared against indirect search experiments in terms of the DM annihilation cross-section $\langle\sigma v_{\text{rel}}\rangle$, as the rate for direct searches experiments is suppressed by additional velocity-dependent terms entering the cross-section. However, the observed exclusion limits for pseudo-scalar mediator models with unitary coupling assumption are limited to a very narrow mass range, due to a small data excess in the analysis (Fig. 13(b)). For this reason, we defer this comparison to the results with the full Run-2 dataset.

The observed limits for the V/AV, VBC and scalar mediator models are compared with direct search experiments in Figures 19-21. The excluded regions are indicated by shaded areas inside the contours. Each combined contour summarises the ATLAS results on each considered model, obtained by using the best expected limit for each parameter point in the figure. When the contour does not close inside the plotted area, the exclusion of smaller scattering cross-section does not imply that larger scattering cross-section (beyond the y-axis range) are also excluded.

The spin-dependent WIMP-neutron (WIMP-proton) scattering cross-section in the context of the leptophobic Z'_A mediator model are shown in the upper (lower) panel of Fig. 19. The difference between the WIMP-proton and the WIMP-neutron cross-section is negligible. The ATLAS exclusion curves are therefore identical in the two panels. The collider searches for this specific leptophobic axial-vector model complement and extend the direct searches reach, being particularly sensitive in the low DM mass parameter space,

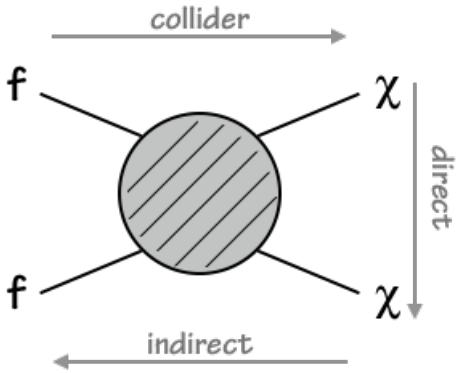

Figure 18: Schematic summary of the complementary approaches used in searches for WIMP DM.

where the LUX and PICO experiments have less sensitivity due to the very low-energy recoils that such low-mass dark matter particles would induce. As in the case of the interpretation of the results in terms of mediator and DM masses (Sec. 6.1.1), if the values chosen for the couplings is reduced, the relative interplay between direct and collider searches changes. This is exemplified by the change of lepton and quark couplings in the leptophilic Z'_A mediator model shown in Figure 20, where the reach of resonant di-quark final states is greatly reduced in favour of dilepton searches (differently for the two scenario) and limited to mediator masses above 200 GeV. The sensitivity of the $E_{\mathrm{T}}^{\mathrm{miss}} + X$ searches between the model in Figs. 19 and 20(b) is the same. This is a coincidental result of two opposite effects [40]: the fact that the scattering cross-section limit is inversely proportional to the mediator mass reach (raised to the fourth power), which is higher in the leptophobic mediator model (Fig. 10(a)), and the fact that the σ_{SD} limit is proportional to g_q^2, which is lower in the leptophilic mediator model. These two effect happen to balance each others for the two couplings assumptions we consider in this note, resulting in similar σ_{SD} exclusion limits.

The spin-independent WIMP-nucleon scattering cross-section results for leptophobic, leptophilic or baryon-charged vector mediator Z' and scalar color-neutral mediator ϕ are compared with the most stringent direct detection limits to date from the LUX, CRESST-II, XENON1T, SuperCDMS and PandaX Collaborations in Figure 21. One contour for each model is presented in the figure and it includes the combination, based on the best expected limit for each parameter point, of every analysis considered for each model and presented in Sec. 6. The excluded regions are indicated by shaded areas inside the contour. When the contour does not close inside the plotted area, the exclusion of smaller scattering cross-section does not imply that larger scattering cross-section (beyond the y-axis range) are also excluded. The collider searches in this case complement the direct searches reach for $m_\chi \lesssim 5$ GeV. By comparing the exclusion reach of the ATLAS searches for each of the four models considered in Fig. 21, it is possible to gauge the importance of the production mechanism assumptions on the collider limits, which will always represent a complementary and not exclusive approach to DM searches with respect to direct and indirect searches.

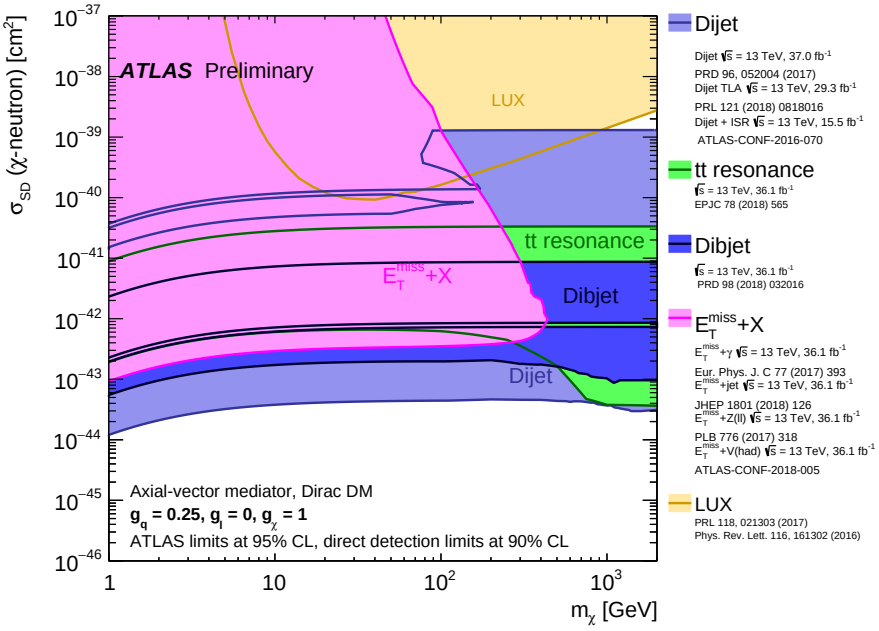

(a)

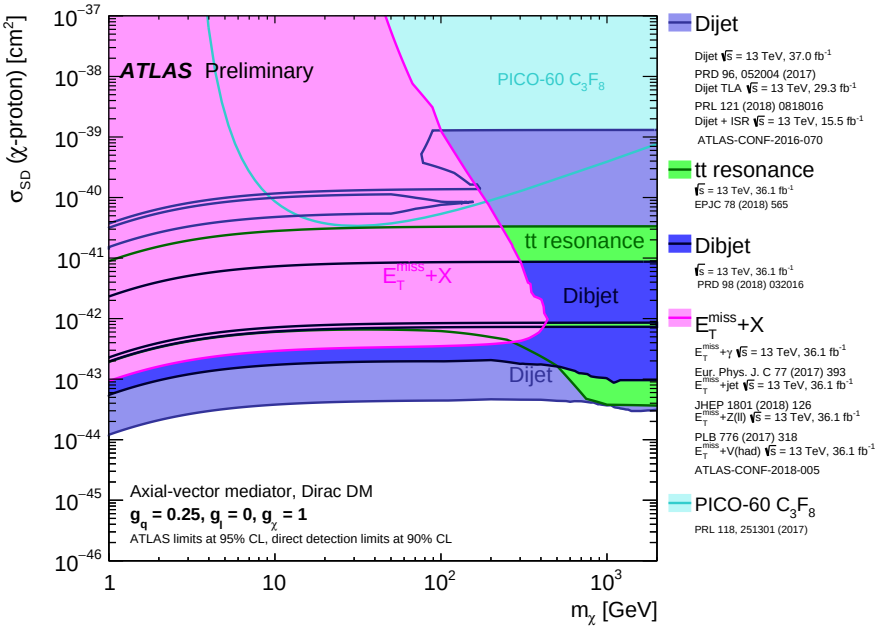

(b)

Figure 19: A comparison of the inferred limits to the constraints from direct detection experiments on the spin-dependent WIMP-neutron (a) or WIMP-proton (b) scattering cross-section in the context of the Z'-like simplified model with axial-vector couplings. The results from this analysis, excluding the region to the left of the contour, are compared with limits from direct detection experiments. LHC limits are shown at 95% CL and direct detection limits at 90% CL. The comparison is valid solely in the context of this model, assuming a mediator width fixed by the dark matter mass and coupling values $g_q = 0.1, g_\ell = 0.1$, and $g_\chi = 1$. LHC searches and direct detection experiments exclude the shaded areas. Exclusions of smaller scattering cross-sections do not imply that larger scattering cross-sections are also excluded. The resonance and $E_{\mathrm{T}}^{\mathrm{miss}}$+X exclusion region represents the union of exclusions from all analyses of that type.

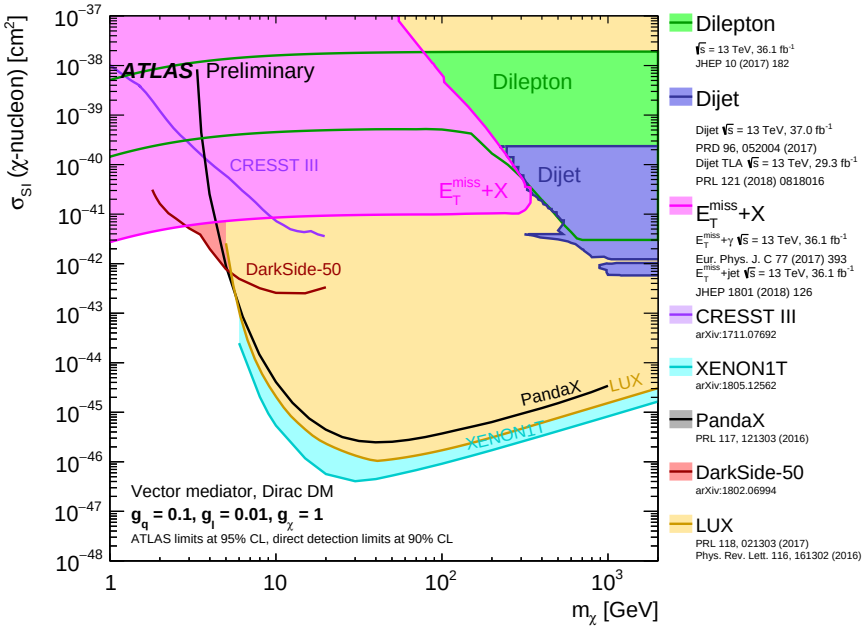

(a)

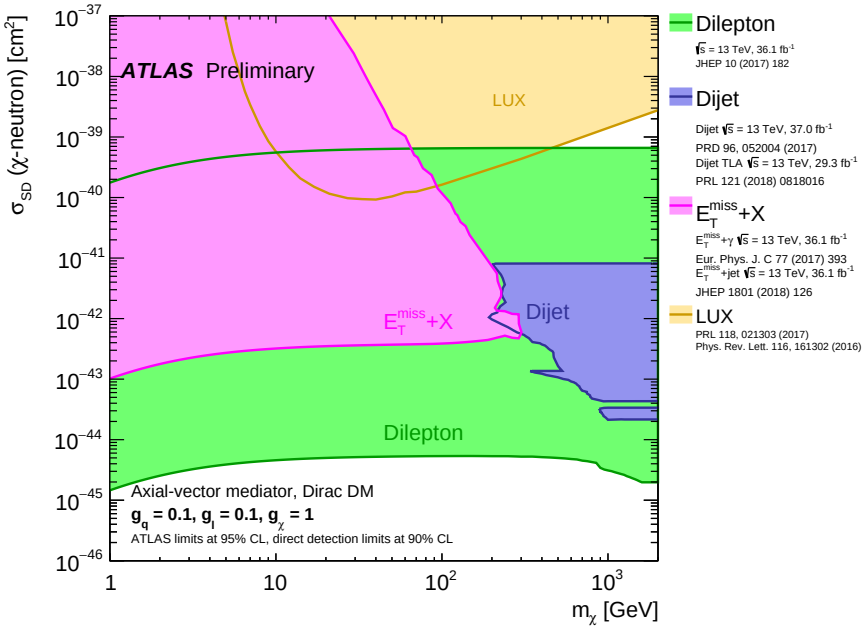

(b)

Figure 20: A comparison of the inferred limits to the constraints from direct detection experiments on the spin-independent WIMP-nucleon (spin-dependent WIMP-neutron) scattering cross-section in the context of the Z'-like simplified model with leptophilic vector (a) or axial-vector (b) couplings. The results from this analysis, excluding the region to the left of the contour, are compared with limits from the direct detection experiments. LHC limits are shown at 95% CL and direct detection limits at 90% CL. The comparison is valid solely in the context of this model, assuming a mediator width fixed by the dark matter mass and the coupling values highlighted in each figure. LHC searches and direct detection experiments exclude the shaded areas. Exclusions of smaller scattering cross-sections do not imply that larger scattering cross-sections are also excluded. The resonance and $E_{\mathrm{T}}^{\mathrm{miss}}$+X exclusion region represents the union of exclusions from all analyses of that type.

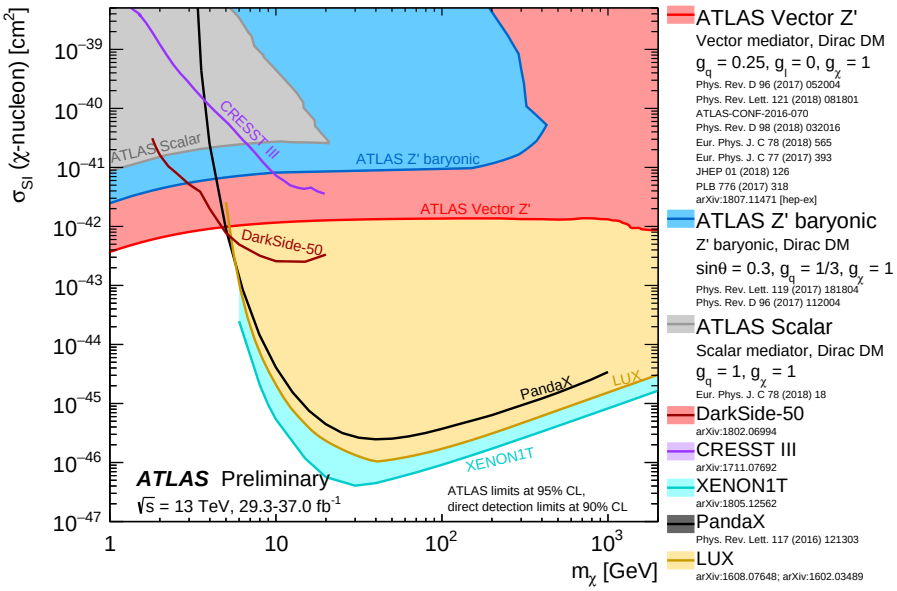

Figure 21: A comparison of the inferred limits to the constraints from direct detection experiments on the spin-independent WIMP-nucleon scattering cross-section. The results from ATLAS analyses, excluding the shaded regions, are compared with limits from direct detection experiments. LHC limits are shown at 95% CL and direct detection limits at 90% CL. The comparison is valid solely in the context of this model, assuming a mediator width fixed by the dark matter mass and coupling values $g_q = 0.25$, $g_l = 0$ or $g_q = 0.1$, $g_l = 0.01$ for the neutral-mediator model and coupling $g_q = 0.33$ for the baryon-charged mediator. The coupling to the DM particle g_χ, is set to unity in all cases. LHC searches and direct detection experiments exclude the shaded areas. Exclusions of smaller scattering cross-sections do not imply that larger scattering cross-sections are also excluded. The single dijet and X+$E_{\mathrm{T}}^{\mathrm{miss}}$ exclusion region represents the union of exclusions from all analyses of that type.

C Additional material

Definitions and values of parameters in the 2HDM+a model		
Symbol	Definition	Value
α	mixing angle of the two neutral CP-even weak eigenstates	$\cos(\beta-\alpha)=0$
θ	mixing angle of the two neutral CP-odd weak eigenstates	varied
$\tan\beta$	ratio of the vacuum expectation values of the two Higgs doublets	varied
v	electroweak vacuum expectation value	246 GeV
λ_{P1}	quartic coupling between the scalar doublets H_1 and the additional pseudo-scalar	$=\lambda_3$
λ_{P2}	quartic coupling between the scalar doublets H_1 and the additional pseudo-scalar	$=\lambda_3$
λ_3	The quartic coupling between the scalar doublets H_1 and H_2	3
y_χ	coupling between the DM and the additional pseudo-scalar	1
m_h	mass of the lightest CP-even mass eigenstate	125 GeV
m_H	mass of the heaviest CP-even mass eigenstate	$=m_A$
m_A	mass of the heaviest CP-odd mass eigenstate	varied
m_a	mass of the lightest CP-odd mass eigenstate	varied
$m_{H^\pm}$	mass of the charged Higgs eigenstate	$=m_A$
m_χ	mass of the DM particle	10 GeV

Table 6: Details of the definition and value assumptions of the main parameters of the 2HDM+a model.

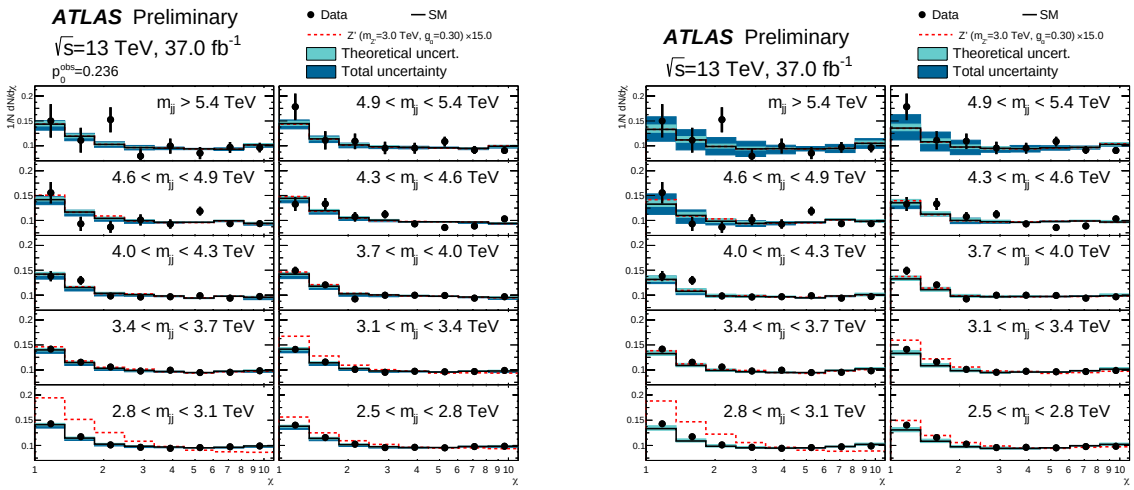

(a) (b)

Figure 22: Reconstructed distributions of the dijet angular variable χ in different regions of the dijet invariant mass m_{jj} for events with $|y^*| < 1.7$, $|y_B| < 1.1$ and $p_{\mathrm{T}} > 440(60)$ GeV for the leading (subleading) jet. The data (black points), Pythia predictions with NLO and electroweak corrections applied (solid lines), and an example of the AV signal ($m_{Z'_A} = 3$ TeV, $g_q = 0.3$), scaled to 15 times its cross-section, are shown. The theoretical uncertainties and the total theoretical and experimental uncertainties in the predictions are displayed as shaded bands around the SM prediction. The SM background prediction and corresponding systematic uncertainty bands are extracted from the best-fit to the data. Data and predictions are normalised to unity in each m_{jj} bin.

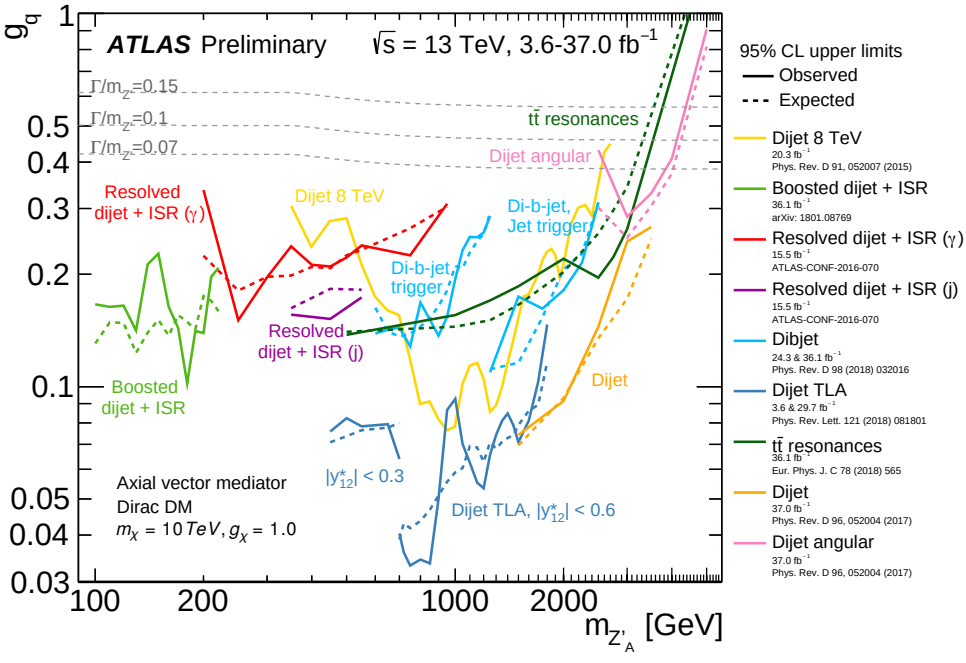

Figure 23: 95% CL upper limits in the coupling-mediator mass plane from di-jet searches on coupling g_q as a function of the resonance mass $m_{Z'}$ for the leptophobic axial-vector Z' model. The expected limits from each search are indicated by dotted curves.

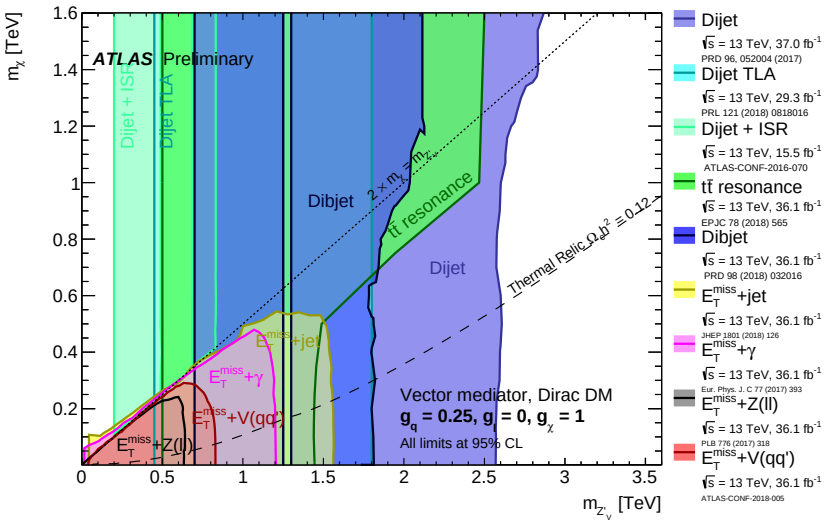

Figure 24: Regions in a DM mass-mediator mass plane excluded at 95% CL by dijet, dilepton and $E_{\mathrm{T}}^{\mathrm{miss}}+X$ searches, for vector mediator simplified models. Exclusion contours from each in each analysis is shown separately. The exclusions are computed for a DM coupling g_χ, quark coupling g_q, universal to all flavours, and lepton coupling g_ℓ as indicated in the canvas. Dashed curves labeled "thermal relic" indicate combinations of DM and mediator mass that are consistent with a DM density of $\Omega h^2 = 0.12$ and a standard thermal history, as computed in MadDM [arXiv:1509.03683,1703.05703]. Between the two curves, annihilation processes described by the simplified model deplete Ωh^2 below 0.12. A dotted curve indicates the kinematic threshold where the mediator can decay on-shell into DM.

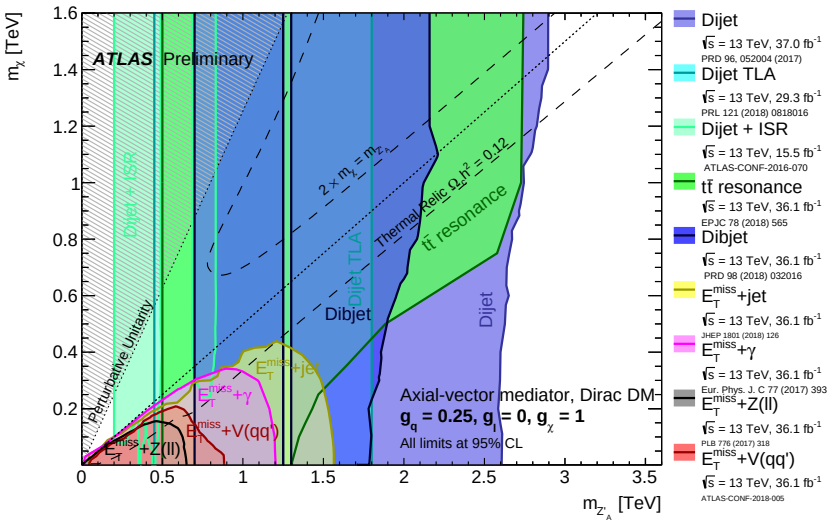

Figure 25: Regions in a DM mass-mediator mass plane excluded at 95% CL by dijet, dilepton and $E_{\mathrm{T}}^{\mathrm{miss}}+X$ searches, for axial vector mediator simplified models. Exclusion contours from each in each analysis is shown separately. The exclusions are computed for a DM coupling g_χ, quark coupling g_q, universal to all flavours, and lepton coupling g_ℓ as indicated in the canvas. Dashed curves labeled "thermal relic" indicate combinations of DM and mediator mass that are consistent with a DM density of $\Omega h^2 = 0.12$ and a standard thermal history, as computed in MadDM [arXiv:1509.03683,1703.05703]. Between the two curves, annihilation processes described by the simplified model deplete Ωh^2 below 0.12. A dotted curve indicates the kinematic threshold where the mediator can decay on-shell into DM. Excluded regions that are in tension with the perturbative unitary considerations of [arXiv:1510.02110] are indicated by shading in the upper left corner.

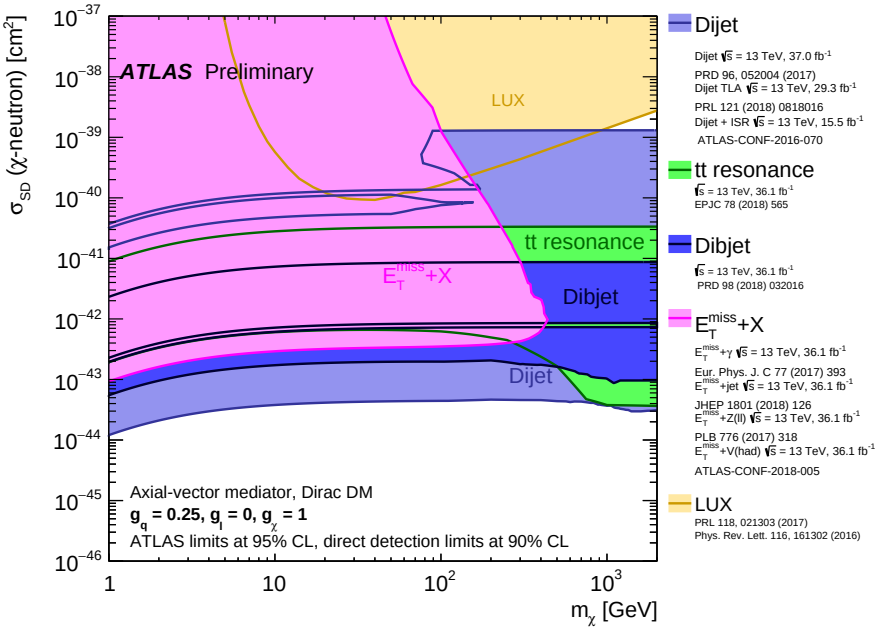

Figure 26: A comparison of the inferred limits to the constraints from direct detection experiments on the spin-dependent WIMP-neutron scattering cross-section in the context of the Z'-like simplified model with axial-vector couplings. The results from this analysis, excluding the region to the left of the contour, are compared with limits from the LUX experiment. LHC limits are shown at 95% CL and direct detection limits at 90% CL. The comparison is valid solely in the context of this model, assuming a mediator width fixed by the dark matter mass and coupling values $g_q = 0.1, g_\ell = 0.1$, and $g_\chi = 1$. LHC searches and direct detection experiments exclude the shaded areas. Exclusions of smaller scattering cross-sections do not imply that larger scattering cross-sections are also excluded. The resonance and $E_{\mathrm{T}}^{\mathrm{miss}}$+X exclusion region represents the union of exclusions from all analyses of that type.

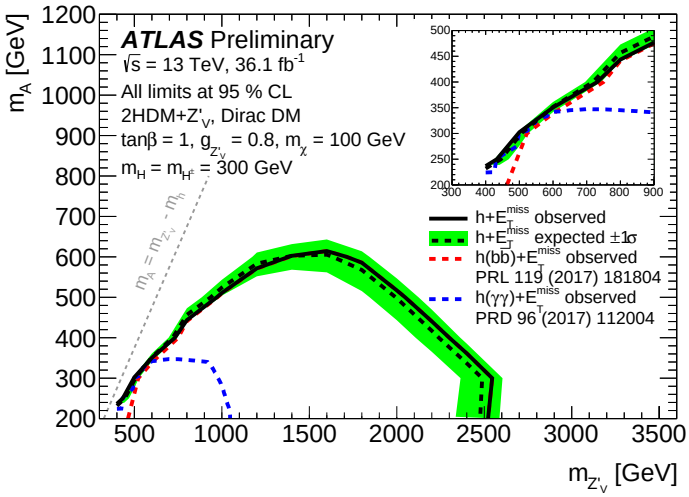

Figure 27: Exclusion contours for the Z'-2HDM scenario in the $(m_{Z'_V}, m_A)$ plane for $\tan\beta = 1$, $g_{Z'_V} = 0.8$ and $m_\chi = 100$ GeV. The dashed red and blue lines indicate the observed exclusion contours from the two separate channels, while the black solid (dashed) line shows the observed (expected) exclusion, for the combined result. The green band around the expected combined contour shows the effect of one σ variation of the total systematic uncertainties. The inset in the top-right side of the panel shows a zoomed version of the result for low $m_{Z'_V}$ masses to highlight the complementarity between the $h(b\bar{b}) + E_{\mathrm{T}}^{\mathrm{miss}}$ and the $h(\gamma\gamma) + E_{\mathrm{T}}^{\mathrm{miss}}$ analyses in this parameter region.

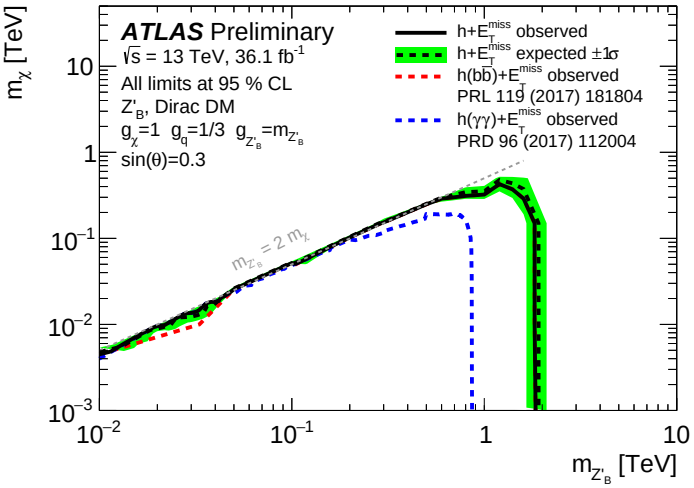

Figure 28: Exclusion contours for the VBC model in the $(m_{Z'_B}, m_\chi)$ plane for $g_q = 1/3$, $g_\chi = 1$ and $\sin\theta = 0.3$. The dashed red and blue line indicates the observed exclusion contours from the two separate channels, while the black solid (dashed) line shows the observed (expected) exclusion, for the combined result. The green band around the expected combined contour shows the effect of one σ variation of the total systematic uncertainties.

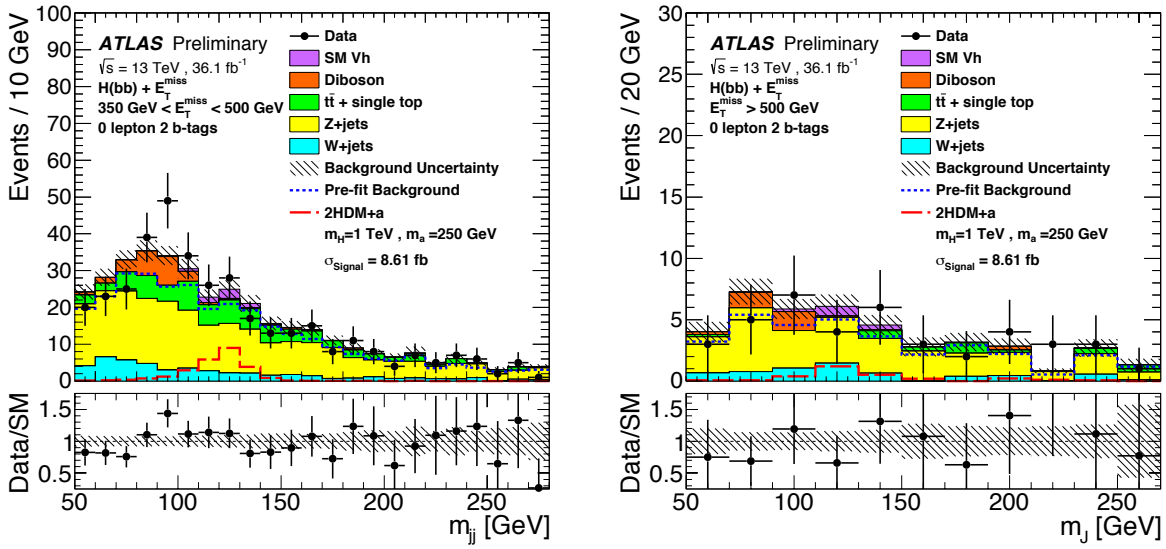

(a) (b)

Figure 29: Observed mass distribution in the $h(b\bar{b}) + E_{\mathrm{T}}^{\mathrm{miss}}$analysis in the 2 b-tag signal regions compared to the background predictions. The error bands show the total statistical and systematic uncertainties on the background predictions. Expected mass distribution for a representative signal model is also shown. This corresponds to a 2HDM+a signal with $m_a = 250$ GeV, $m_A = 1000$ GeV, $\tan\beta = 1.0$, $\sin\theta = 0.35$, $g_\chi = 1.0$ and $m_\chi = 10$ GeV.

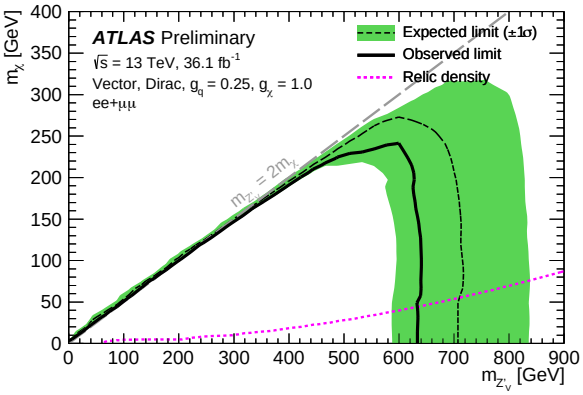

(a) $g_\chi = 1$, $g_q = 0.25$, $g_l = 0$.

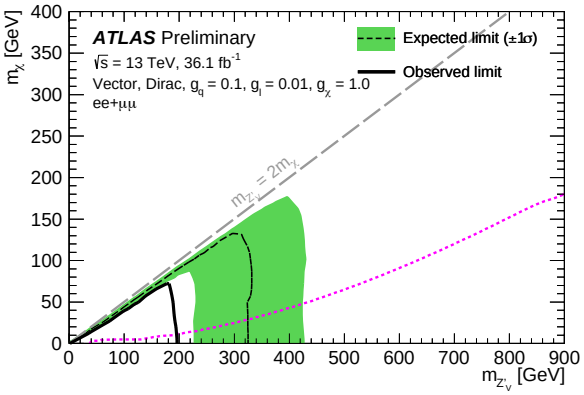

(b) $g_\chi = 1$, $g_q = 0.1$, $g_l = 0.01$.

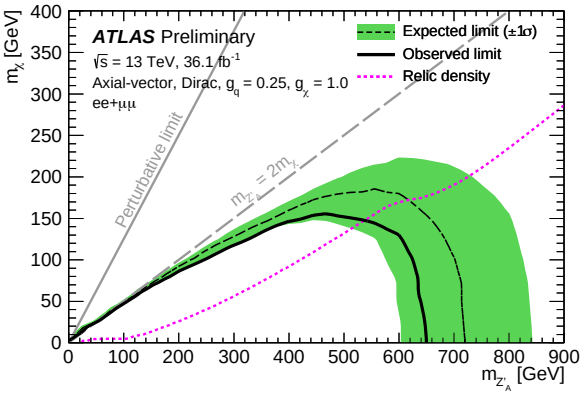

(c) $g_\chi = 1$, $g_q = 0.25$, $g_l = 0$.

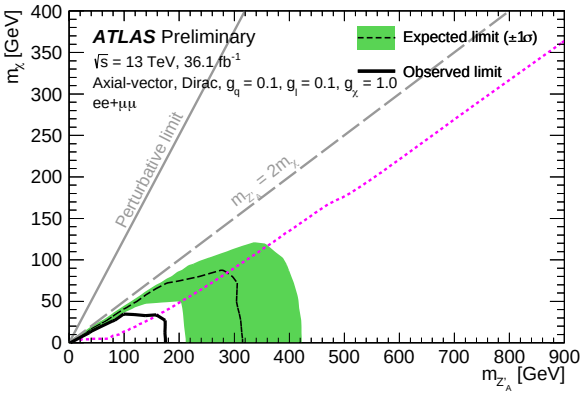

(d) $g_\chi = 1$, $g_q = 0.1$, $g_l = 0.1$.

Figure 30: Regions in a DM mass-mediator mass plane excluded at 95% CL by the $Z(\ell\ell) + E_{\mathrm{T}}^{\mathrm{miss}}$ search, for vector (a, b) or axial-vector (c, d) mediator simplified models described in Sec. 2.1.1. The exclusions are computed for a DM coupling g_χ, quark coupling g_q, universal to all flavours, and lepton coupling g_ℓ as indicated in each case. Dashed curves labeled "relic relic" indicate combinations of DM and mediator mass that are consistent with a DM density of $\Omega h^2 = 0.12$ and a standard thermal history, as computed in MadDM [arXiv:1509.03683,1703.05703]. Between the two curves, annihilation processes described by the simplified model deplete Ωh^2 below 0.12. A dashed curve indicates the kinematic threshold where the mediator can decay on-shell into DM. Excluded regions that are in tension with the perturbative unitary considerations of [arXiv:1510.02110] are indicated by a gray line.

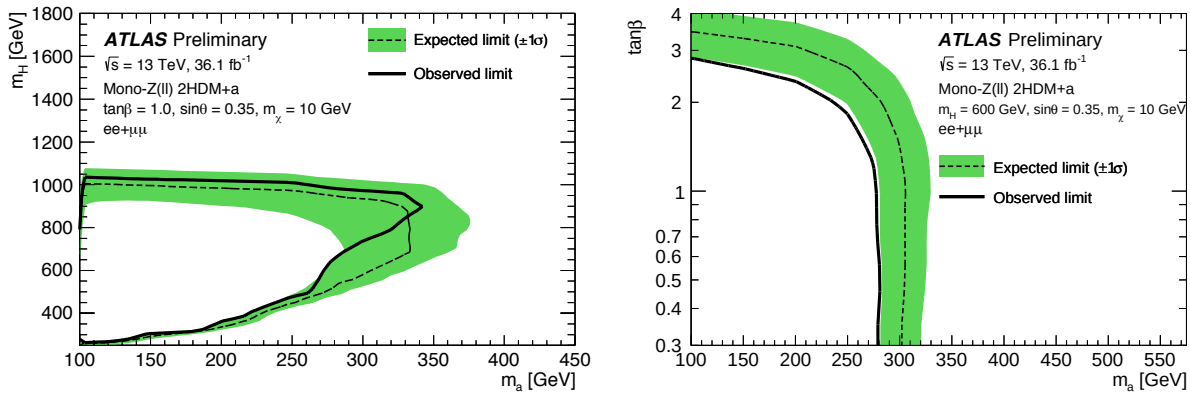

(a) (b)

Figure 31: Regions in a (m_a, m_A) (a) and $(m_a, \tan\beta)$ (b) planes excluded by data at 95% CL by the $Z(\ell\ell) + E_{\mathrm{T}}^{\mathrm{miss}}$ analysis, following the parameter choices of scenarios 1 and 2 of the 2HDM+a model (see note for details). The exclusion limits presented above conservatively neglect the contribution from $b\bar{b}$ initiated production, which might be sizeable for $\tan\beta \geq 3$ for the $Z + E_{\mathrm{T}}^{\mathrm{miss}}$ channel.

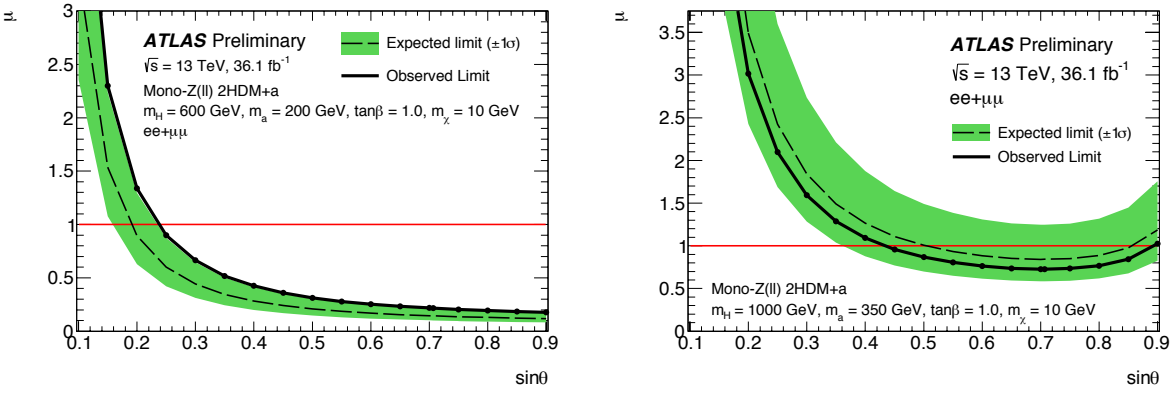

(a) (b)

Figure 32: Observed exclusion limits from the $Z(\ell\ell) + E_{\mathrm{T}}^{\mathrm{miss}}$ analysis for the 2HDM+a model as a function of $\sin\theta$, following the two parameter choices of scenario 3 (see note for details). The limits are calculated at 95% C.L. and are expressed in terms of the ratio of the excluded cross-section to the nominal cross-section of the model.

References

[1] G. Hinshaw et al., *Nine-Year Wilkinson Microwave Anisotropy Probe (WMAP) Observations: Cosmological Parameter Results*, Astrophys. J. Suppl. **208** (2013) 19, arXiv: 1212.5226 [astro-ph.CO].

[2] Y. Akrami et al., *Planck 2018 results. I. Overview and the cosmological legacy of Planck*, (2018), arXiv: 1807.06205 [astro-ph.CO].

[3] V. Trimble, *Existence and Nature of Dark Matter in the Universe*, Ann. Rev. Astron. Astrophys. **25** (1987) 425.

[4] G. Bertone, D. Hooper, and J. Silk, *Particle dark matter: Evidence, candidates and constraints*, Phys. Rept. **405** (2005) 279, arXiv: hep-ph/0404175 [hep-ph].

[5] J. L. Feng, *Dark Matter Candidates from Particle Physics and Methods of Detection*, Ann. Rev. Astron. Astrophys. **48** (2010) 495, arXiv: 1003.0904 [astro-ph.CO].

[6] G. Angloher et al., *Results on light dark matter particles with a low-threshold CRESST-II detector*, Eur. Phys. J. C **76** (2016) 25, arXiv: 1509.01515 [astro-ph.CO].

[7] D. S. Akerib et al., *Results from a search for dark matter in the complete LUX exposure*, Phys. Rev. Lett. **118** (2017) 021303, arXiv: 1608.07648 [astro-ph.CO].

[8] C. Amole et al., *Dark Matter Search Results from the PICO-60 C_3F_8 Bubble Chamber*, Phys. Rev. Lett. **118** (2017) 251301, arXiv: 1702.07666 [astro-ph.CO].

[9] P. A. Amaudruz et al., *First results from the DEAP-3600 dark matter search with argon at SNOLAB*, Phys. Rev. Lett. **121** (2018) 071801, arXiv: 1707.08042 [astro-ph.CO].

[10] X. Cui et al., *Dark Matter Results From 54-Ton-Day Exposure of PandaX-II Experiment*, Phys. Rev. Lett. **119** (2017) 181302, arXiv: 1708.06917 [astro-ph.CO].

[11] E. Aprile et al., *Dark Matter Search Results from a One Tonne×Year Exposure of XENON1T*, (2018), arXiv: 1805.12562 [astro-ph.CO].

[12] E. Aprile et al., *First Dark Matter Search Results from the XENON1T Experiment*, Phys. Rev. Lett. **119** (2017) 181301, arXiv: 1705.06655 [astro-ph.CO].

[13] R. Agnese et al., *Low-mass dark matter search with CDMSlite*, Phys. Rev. D **97** (2018) 022002, arXiv: 1707.01632 [astro-ph.CO].

[14] R. Agnese et al., *Results from the Super Cryogenic Dark Matter Search Experiment at Soudan*, Phys. Rev. Lett. **120** (2018) 061802, arXiv: 1708.08869 [hep-ex].

[15] K. Choi et al., *Search for neutrinos from annihilation of captured low-mass dark matter particles in the Sun by Super-Kamiokande*, Phys. Rev. Lett. **114** (2015) 141301, arXiv: 1503.04858 [hep-ex].

[16] M. G. Aartsen et al., *Search for neutrinos from decaying dark matter with IceCube*, (2018), arXiv: 1804.03848 [astro-ph.HE].

[17] F. Acero et al., *Spectrum and variability of the Galactic Center VHE gamma-ray source HESS J1745-290*, Astron. & Astrophys. **503** (2009) 817, arXiv: 0906.1247.

[18] F. Acero et al., *Localising the VHE gamma-ray source at the Galactic Centre*, Mon. Not. R. Astron. Soc **402** (2010) 1877, arXiv: 0911.1912.

[19] M. Ackermann et al., *The Fermi Galactic Center GeV Excess and Implications for Dark Matter*, Astrophys. J. **840** (2017) 43, arXiv: 1704.03910 [astro-ph.HE].

[20] ATLAS Collaboration, *Search for dark matter in events with a hadronically decaying vector boson and missing transverse momentum in pp collisions at* $\sqrt{s} = 13$ *TeV with the ATLAS detector*, Submitted to: JHEP (2018), arXiv: 1807.11471 [hep-ex].

[21] ATLAS Collaboration, *Search for dark matter at* $\sqrt{s} = 13$ *TeV in final states containing an energetic photon and large missing transverse momentum with the ATLAS detector*, Eur. Phys. J. C **77** (2017) 393, arXiv: 1704.03848 [hep-ex].

[22] ATLAS Collaboration, *Search for dark matter in association with a Higgs boson decaying to two photons at* $\sqrt{s} = 13$ *TeV with the ATLAS detector*, Phys. Rev. D **96** (2017) 112004, arXiv: 1706.03948 [hep-ex].

[23] ATLAS Collaboration, *Search for Dark Matter Produced in Association with a Higgs Boson Decaying to* $b\bar{b}$ *using* 36 fb^{-1} *of pp collisions at* $\sqrt{s} = 13$ *TeV with the ATLAS Detector*, Phys. Rev. Lett. **119** (2017) 181804, arXiv: 1707.01302 [hep-ex].

[24] ATLAS Collaboration, *Search for an invisibly decaying Higgs boson or dark matter candidates produced in association with a Z boson in pp collisions at* $\sqrt{s} = 13$ *TeV with the ATLAS detector*, Phys. Lett. B **776** (2018) 318, arXiv: 1708.09624 [hep-ex].

[25] ATLAS Collaboration, *Search for dark matter produced in association with bottom or top quarks in* $\sqrt{s} = 13$ *TeV pp collisions with the ATLAS detector*, Eur. Phys. J. C **78** (2018) 18, arXiv: 1710.11412 [hep-ex].

[26] ATLAS Collaboration, *Search for dark matter and other new phenomena in events with an energetic jet and large missing transverse momentum using the ATLAS detector*, JHEP **01** (2018) 126, arXiv: 1711.03301 [hep-ex].

[27] ATLAS Collaboration, *Search for top-squark pair production in final states with one lepton, jets, and missing transverse momentum using* 36 fb^{-1} *of* $\sqrt{s} = 13$ *TeV pp collision data with the ATLAS detector*, JHEP **06** (2018) 108, arXiv: 1711.11520 [hep-ex].

[28] ATLAS Collaboration, *Search for a scalar partner of the top quark in the jets plus missing transverse momentum final state at* $\sqrt{s} = 13$ *TeV with the ATLAS detector*, JHEP **12** (2017) 085, arXiv: 1709.04183 [hep-ex].

[29] ATLAS Collaboration, *Constraints on new phenomena via Higgs boson couplings and invisible decays with the ATLAS detector*, JHEP **11** (2015) 206, arXiv: 1509.00672 [hep-ex].

[30] CMS Collaboration, *Search for dark matter produced with an energetic jet or a hadronically decaying W or Z boson at* $\sqrt{s} = 13$ *TeV*, JHEP **07** (2017) 014, arXiv: 1703.01651 [hep-ex].

[31] CMS Collaboration, *Search for associated production of dark matter with a Higgs boson decaying to* $b\bar{b}$ *or* $\gamma\gamma$ *at* $\sqrt{s} = 13$ *TeV*, JHEP **10** (2017) 180, arXiv: 1703.05236 [hep-ex].

[32] CMS Collaboration, *Search for dark matter produced in association with heavy-flavor quark pairs in proton–proton collisions at* $\sqrt{s} = 13$ *TeV*, Eur. Phys. J. C **77** (2017) 845, arXiv: 1706.02581 [hep-ex].

[33] CMS Collaboration,
Search for new physics in the monophoton final state in proton–proton collisions at $\sqrt{s}$ = 13 *TeV*,
JHEP **10** (2017) 073, arXiv: 1706.03794 [hep-ex].

[34] CMS Collaboration, *Search for top squarks and dark matter particles in opposite-charge dilepton final states at* $\sqrt{s}$ = *13 TeV,* 2017, arXiv: 1711.00752 [hep-ex].

[35] M. Roos, *Astrophysical and cosmological probes of dark matter*,
J. of Modern Physics **3** (2012) 1152, arXiv: 1208.3662.

[36] S. Arrenberg et al., *Working Group Report: Dark Matter Complementarity*, 2013,
arXiv: 1310.8621 [hep-ph].

[37] G. Steigman and M. S. Turner,
Cosmological constraints on the properties of Weakly Interacting Massive Particles,
Nucl. Phys. B **253** (1985) 375.

[38] E. W. Kolb and M. S. Turner, *The Early Universe*, Front. Phys. **69** (1990) 1.

[39] D. Abercrombie et al., *Dark Matter Benchmark Models for Early LHC Run-2 Searches: Report of the ATLAS/CMS Dark Matter Forum*, (2015), arXiv: 1507.00966 [hep-ex].

[40] G. Busoni et al., *Recommendations on presenting LHC searches for missing transverse energy signals using simplified s-channel models of dark matter*, (2016), ed. by A. Boveia et al.,
arXiv: 1603.04156 [hep-ex].

[41] A. Albert et al., *Recommendations of the LHC Dark Matter Working Group: Comparing LHC searches for heavy mediators of dark matter production in visible and invisible decay channels*, (2017), arXiv: 1703.05703 [hep-ex].

[42] T. Abe et al., *LHC Dark Matter Working Group: Next-generation spin-0 dark matter models*, (2018), arXiv: 1810.09420 [hep-ex].

[43] S. P. Martin, *A Supersymmetry primer*, Adv. Ser. Direct. High Energy Phys. **18** (1998) 1,
arXiv: hep-ph/9709356.

[44] G. R. Farrar and P. Fayet, *Phenomenology of the Production, Decay, and Detection of New Hadronic States Associated with Supersymmetry*, Phys. Lett. B **76** (1978) 575.

[45] H. Goldberg, *Constraint on the Photino Mass from Cosmology*,
Phys. Rev. Lett. **50** (1983) 1419, Erratum: Phys. Rev. Lett. **103** (2009) 099905.

[46] J. R. Ellis, J. S. Hagelin, D. V. Nanopoulos, K. A. Olive, and M. Srednicki,
Supersymmetric Relics from the Big Bang, Nucl. Phys. B **238** (1984) 453.

[47] ATLAS Collaboration, *Search for the electroweak production of supersymmetric particles in* $\sqrt{s}$ = 8 *TeV pp collisions with the ATLAS detector*, Phys. Rev. D **93** (2016) 052002,
arXiv: 1509.07152 [hep-ex].

[48] ATLAS Collaboration, *Summary of the searches for squarks and gluinos using* $\sqrt{s}$ = 8 *TeV pp collisions with the ATLAS experiment at the LHC*, JHEP **10** (2015) 054,
arXiv: 1507.05525 [hep-ex].

[49] ATLAS Collaboration, *ATLAS Run 1 searches for direct pair production of third-generation squarks at the Large Hadron Collider*, Eur. Phys. J. C **75** (2015) 510,
arXiv: 1506.08616 [hep-ex].

[50] ATLAS Collaboration, *Summary of the ATLAS experiment's sensitivity to supersymmetry after LHC Run 1 — interpreted in the phenomenological MSSM*, JHEP **10** (2015) 134, arXiv: 1508.06608 [hep-ex].

[51] ATLAS Collaboration, *Dark matter interpretations of ATLAS searches for the electroweak production of supersymmetric particles in $\sqrt{s}$ = 8 TeV proton–proton collisions*, JHEP **09** (2016) 175, arXiv: 1608.00872 [hep-ex].

[52] ATLAS Collaboration, *Search for the direct production of charginos and neutralinos in final states with tau leptons in $\sqrt{s}$ = 13 TeV pp collisions with the ATLAS detector*, Eur. Phys. J. C **78** (2018) 154, arXiv: 1708.07875 [hep-ex].

[53] ATLAS Collaboration, *Search for electroweak production of supersymmetric particles in final states with two or three leptons at $\sqrt{s}$ = 13 TeV with the ATLAS detector*, (2018), arXiv: 1803.02762 [hep-ex].

[54] ATLAS Collaboration, *Search for electroweak production of supersymmetric states in scenarios with compressed mass spectra at $\sqrt{s}$ = 13 TeV with the ATLAS detector*, Phys. Rev. D **97** (2018) 052010, arXiv: 1712.08119 [hep-ex].

[55] L. Lee, C. Ohm, A. Soffer, and T.-T. Yu, *Collider Searches for Long-Lived Particles Beyond the Standard Model*, (2018), arXiv: 1810.12602 [hep-ph].

[56] L. Evans and P. Bryant, *LHC Machine*, JINST **3** (2008) S08001.

[57] ATLAS Collaboration, *The ATLAS Experiment at the CERN Large Hadron Collider*, JINST **3** (2008) S08003.

[58] P. J. Fox and E. Poppitz, *Leptophilic Dark Matter*, Phys. Rev. D **79** (2009) 083528, arXiv: 0811.0399 [hep-ph].

[59] S. Cassel, D. M. Ghilencea, and G. G. Ross, *Electroweak and Dark Matter Constraints on a Z-prime in Models with a Hidden Valley*, Nucl. Phys. B **827** (2010) 256, arXiv: 0903.1118 [hep-ph].

[60] Y. Bai, P. J. Fox, and R. Harnik, *The Tevatron at the Frontier of Dark Matter Direct Detection*, JHEP **12** (2010) 048, arXiv: 1005.3797 [hep-ph].

[61] J. Abdallah et al., *Simplified Models for Dark Matter Searches at the LHC*, Phys. Dark Univ. **9-10** (2015) 8, arXiv: 1506.03116 [hep-ph].

[62] M. Beltran, D. Hooper, E. W. Kolb, Z. A. C. Krusberg, and T. M. P. Tait, *Maverick dark matter at colliders*, JHEP **09** (2010) 037, arXiv: 1002.4137 [hep-ph].

[63] J. Goodman et al., *Constraints on Light Majorana dark Matter from Colliders*, Phys. Lett. B **695** (2011) 185, arXiv: 1005.1286 [hep-ph].

[64] J. Goodman et al., *Constraints on Dark Matter from Colliders*, Phys. Rev. D **82** (2010) 116010, arXiv: 1008.1783 [hep-ph].

[65] A. Rajaraman, W. Shepherd, T. M. P. Tait, and A. M. Wijangco, *LHC Bounds on Interactions of Dark Matter*, Phys. Rev. D **84** (2011) 095013, arXiv: 1108.1196 [hep-ph].

[66] P. J. Fox, R. Harnik, J. Kopp, and Y. Tsai, *Missing Energy Signatures of Dark Matter at the LHC*, Phys. Rev. D **85** (2012) 056011, arXiv: 1109.4398 [hep-ph].

[67] A. Alves, A. Berlin, S. Profumo, and F. S. Queiroz,
Dark Matter Complementarity and the Z′ Portal, Phys. Rev. D **92** (2015) 083004,
arXiv: 1501.03490 [hep-ph].

[68] P. Gondolo, P. Ko, and Y. Omura, *Light dark matter in leptophobic Z' models*,
Phys. Rev. D **85** (2012) 035022, arXiv: 1106.0885 [hep-ph].

[69] M. T. Frandsen, F. Kahlhoefer, S. Sarkar, and K. Schmidt-Hoberg,
Direct detection of dark matter in models with a light Z', JHEP **09** (2011) 128,
arXiv: 1107.2118 [hep-ph].

[70] H. An, X. Ji, and L.-T. Wang, *Light Dark Matter and Z′ Dark Force at Colliders*,
JHEP **07** (2012) 182, arXiv: 1202.2894 [hep-ph].

[71] A. Alves, S. Profumo, and F. S. Queiroz, *The dark $Z^{'}$ portal: direct, indirect and collider searches*,
JHEP **04** (2014) 063, arXiv: 1312.5281 [hep-ph].

[72] O. Lebedev and Y. Mambrini, *Axial dark matter: The case for an invisible Z′*,
Phys. Lett. B **734** (2014) 350, arXiv: 1403.4837 [hep-ph].

[73] M. Papucci, A. Vichi, and K. M. Zurek, *Monojet versus the rest of the world I: t-channel models*,
JHEP **11** (2014) 024, arXiv: 1402.2285 [hep-ph].

[74] O. Buchmueller, M. J. Dolan, S. A. Malik, and C. McCabe, *Characterising dark matter searches
at colliders and direct detection experiments: Vector mediators*, JHEP **01** (2015) 037,
arXiv: 1407.8257 [hep-ph].

[75] C. D. Carone and H. Murayama, *Possible light U(1) gauge boson coupled to baryon number*,
Phys. Rev. Lett. **74** (1995) 3122, arXiv: hep-ph/9411256 [hep-ph].

[76] K. Agashe and G. Servant, *Warped unification, proton stability and dark matter*,
Phys. Rev. Lett. **93** (2004) 231805, arXiv: hep-ph/0403143 [hep-ph].

[77] P. Fileviez Perez and M. B. Wise, *Baryon and lepton number as local gauge symmetries*,
Phys. Rev. D **82** (2010) 011901, [Erratum: Phys. Rev.D82,079901(2010)],
arXiv: 1002.1754 [hep-ph].

[78] L. Carpenter et al., *Mono-Higgs-boson: A new collider probe of dark matter*,
Phys. Rev. D **89** (2014) 075017, arXiv: 1312.2592 [hep-ph].

[79] K. Cheung, K. Mawatari, E. Senaha, P.-Y. Tseng, and T.-C. Yuan, *The Top Window for dark matter*,
JHEP **10** (2010) 081, arXiv: 1009.0618 [hep-ph].

[80] U. Haisch, A. Hibbs, and E. Re, *Determining the structure of dark-matter couplings at the LHC*,
Phys. Rev. D **89** (2014) 034009, arXiv: 1311.7131 [hep-ph].

[81] M. R. Buckley, D. Feld, and D. Goncalves, *Scalar Simplified Models for Dark Matter*,
Phys. Rev. D **91** (2015) 015017, arXiv: 1410.6497 [hep-ph].

[82] M. R. Buckley and D. Goncalves, *Constraining the Strength and CP Structure of Dark Production
at the LHC: the Associated Top-Pair Channel*,
Phys. Rev. D **93** (2016) 034003, [Phys. Rev.D93,034003(2016)], arXiv: 1511.06451 [hep-ph].

[83] U. Haisch and E. Re, *Simplified dark matter top-quark interactions at the LHC*,
JHEP **06** (2015) 078, arXiv: 1503.00691 [hep-ph].

[84] M. Backovic et al., *Higher-order QCD predictions for dark matter production at the LHC in
simplified models with s-channel mediators*, Eur. Phys. J. C **75** (2015) 482,
arXiv: 1508.05327 [hep-ph].

[85] C. Arina et al.,
A comprehensive approach to dark matter studies: exploration of simplified top-philic models,
JHEP **11** (2016) 111, arXiv: 1605.09242 [hep-ph].

[86] U. Haisch, P. Pani, and G. Polesello, *Determining the CP nature of spin-0 mediators in associated production of dark matter and $t\bar{t}$ pairs*, JHEP **02** (2017) 131, arXiv: 1611.09841 [hep-ph].

[87] S. Banerjee et al., *Cornering pseudoscalar-mediated dark matter with the LHC and cosmology*,
JHEP **07** (2017) 080, arXiv: 1705.02327 [hep-ph].

[88] J. Andrea, B. Fuks, and F. Maltoni, *Monotops at the LHC*, Phys. Rev. D **84** (2011) 074025,
arXiv: 1106.6199 [hep-ph].

[89] J.-L. Agram, J. Andrea, M. Buttignol, E. Conte, and B. Fuks,
Monotop phenomenology at the Large Hadron Collider, Phys. Rev. D **89** (2014) 014028,
arXiv: 1311.6478 [hep-ph].

[90] I. Boucheneb, G. Cacciapaglia, A. Deandrea, and B. Fuks,
Revisiting monotop production at the LHC, JHEP **01** (2015) 017, arXiv: 1407.7529 [hep-ph].

[91] B. Batell, J. Pradler, and M. Spannowsky, *Dark Matter from Minimal Flavor Violation*,
JHEP **08** (2011) 038, arXiv: 1105.1781 [hep-ph].

[92] P. Agrawal, S. Blanchet, Z. Chacko, and C. Kilic,
Flavored Dark Matter, and Its Implications for Direct Detection and Colliders,
Phys. Rev. D **86** (2012) 055002, arXiv: 1109.3516 [hep-ph].

[93] K. Cheung, K. Mawatari, E. Senaha, P. Y. Tseng, and T. C. Yuan, *Top window for dark matter*,
Int. J. Mod. Phys. D **20** (2011) 1413.

[94] J. Kile, *Flavored Dark Matter: A Review*, Mod. Phys. Lett. A **28** (2013) 1330031,
arXiv: 1308.0584 [hep-ph].

[95] H. An, L.-T. Wang, and H. Zhang,
Dark matter with t-channel mediator: a simple step beyond contact interaction,
Phys. Rev. D **89** (2014) 115014, arXiv: 1308.0592 [hep-ph].

[96] Y. Bai and J. Berger, *Fermion Portal Dark Matter*, JHEP **11** (2013) 171,
arXiv: 1308.0612 [hep-ph].

[97] A. DiFranzo, K. I. Nagao, A. Rajaraman, and T. M. P. Tait,
Simplified Models for Dark Matter Interacting with Quarks,
JHEP **11** (2013) 014, [Erratum: JHEP01,162(2014)], arXiv: 1308.2679 [hep-ph].

[98] B. Batell, T. Lin, and L.-T. Wang, *Flavored Dark Matter and R-Parity Violation*,
JHEP **01** (2014) 075, arXiv: 1309.4462 [hep-ph].

[99] S. Chang, R. Edezhath, J. Hutchinson, and M. Luty, *Effective WIMPs*,
Phys. Rev. D **89** (2014) 015011, arXiv: 1307.8120 [hep-ph].

[100] P. Agrawal, M. Blanke, and K. Gemmler, *Flavored dark matter beyond Minimal Flavor Violation*,
JHEP **10** (2014) 072, arXiv: 1405.6709 [hep-ph].

[101] P. Agrawal, B. Batell, D. Hooper, and T. Lin,
Flavored Dark Matter and the Galactic Center Gamma-Ray Excess,
Phys. Rev. D **90** (2014) 063512, arXiv: 1404.1373 [hep-ph].

[102] M. A. Gomez, C. B. Jackson, and G. Shaughnessy, *Dark Matter on Top*, JCAP **1412** (2014) 025,
arXiv: 1404.1918 [hep-ph].

[103] C. Kilic, M. D. Klimek, and J.-H. Yu, *Signatures of Top Flavored Dark Matter*, Phys. Rev. D **91** (2015) 054036, arXiv: 1501.02202 [hep-ph].

[104] M. Blanke and S. Kast, *Top-Flavoured Dark Matter in Dark Minimal Flavour Violation*, JHEP **05** (2017) 162, arXiv: 1702.08457 [hep-ph].

[105] M. Blanke, S. Das, and S. Kast, *Flavoured Dark Matter Moving Left*, JHEP **02** (2018) 105, arXiv: 1711.10493 [hep-ph].

[106] G. D'Ambrosio, G. F. Giudice, G. Isidori, and A. Strumia, *Minimal flavor violation: An Effective field theory approach*, Nucl. Phys. B **645** (2002) 155, arXiv: hep-ph/0207036 [hep-ph].

[107] J. Charles et al., *CP violation and the CKM matrix: Assessing the impact of the asymmetric B factories*, Eur. Phys. J. C **41** (2005) 1, arXiv: hep-ph/0406184 [hep-ph].

[108] M. Tanabashi et al., *Review of Particle Physics*, Phys. Rev. D **98** (3 2018) 030001.

[109] D. Pinna, A. Zucchetta, M. R. Buckley, and F. Canelli, *Single top quarks and dark matter*, Phys. Rev. D **96** (2017) 035031, arXiv: 1701.05195 [hep-ph].

[110] P. Pani and G. Polesello, *Dark matter production in association with a single top-quark at the LHC in a two-Higgs-doublet model with a pseudoscalar mediator*, Phys. Dark Univ. **21** (2018) 8, arXiv: 1712.03874 [hep-ph].

[111] T. Plehn, J. Thompson, and S. Westhoff, *Dark Matter from Electroweak Single Top Production*, Phys. Rev. **D98** (2018) 015012, arXiv: 1712.08065 [hep-ph].

[112] G. Brooijmans et al., *Les Houches 2017: Physics at TeV Colliders New Physics Working Group Report*, 2018, arXiv: 1803.10379 [hep-ph].

[113] P. Fayet, *Supersymmetry and Weak, Electromagnetic and Strong Interactions*, Phys. Lett. B **64** (1976) 159.

[114] P. Fayet, *Spontaneously Broken Supersymmetric Theories of Weak, Electromagnetic and Strong Interactions*, Phys. Lett. B **69** (1977) 489.

[115] ATLAS Collaboration, *Search for dark matter in events with heavy quarks and missing transverse momentum in pp collisions with the ATLAS detector*, Eur. Phys. J. C **75** (2015) 92, arXiv: 1410.4031 [hep-ex].

[116] S. Ipek, D. McKeen, and A. E. Nelson, *A Renormalizable Model for the Galactic Center Gamma Ray Excess from Dark Matter Annihilation*, Phys. Rev. D **90** (2014) 055021, arXiv: 1404.3716 [hep-ph].

[117] J. M. No, *Looking through the pseudoscalar portal into dark matter: Novel mono-Higgs and mono-Z signatures at the LHC*, Phys. Rev. D **93** (2016) 031701, arXiv: 1509.01110 [hep-ph].

[118] D. Goncalves, P. A. N. Machado, and J. M. No, *Simplified Models for Dark Matter Face their Consistent Completions*, Phys. Rev. D **95** (2017) 055027, arXiv: 1611.04593 [hep-ph].

[119] N. F. Bell, G. Busoni, and I. W. Sanderson, *Self-consistent Dark Matter Simplified Models with an s-channel scalar mediator*, JCAP **1703** (2017) 015, arXiv: 1612.03475 [hep-ph].

[120] M. Bauer, U. Haisch, and F. Kahlhoefer,
Simplified dark matter models with two Higgs doublets: I. Pseudoscalar mediators,
JHEP **05** (2017) 138, arXiv: 1701.07427 [hep-ph].

[121] M. Bauer, M. Klassen, and V. Tenorth, *Universal Properties of Pseudoscalar Mediators*, (2017),
arXiv: 1712.06597 [hep-ph].

[122] U. Haisch and A. Malinauskas, *Let there be light from a second light Higgs doublet*,
JHEP **03** (2018) 135, arXiv: 1712.06599 [hep-ph].

[123] G. Arcadi, M. Lindner, F. S. Queiroz, W. Rodejohann, and S. Vogl,
Pseudoscalar Mediators: A WIMP model at the Neutrino Floor, JCAP **1803** (2018) 042,
arXiv: 1711.02110 [hep-ph].

[124] N. F. Bell, G. Busoni, and I. W. Sanderson, *Two Higgs Doublet Dark Matter Portal*,
JCAP **1801** (2018) 015, arXiv: 1710.10764 [hep-ph].

[125] J. F. Gunion and H. E. Haber,
The CP conserving two Higgs doublet model: The Approach to the decoupling limit,
Phys. Rev. D **67** (2003) 075019, arXiv: hep-ph/0207010 [hep-ph].

[126] A. Berlin, T. Lin, and L.-T. Wang, *Mono-Higgs Detection of Dark Matter at the LHC*,
JHEP **06** (2014) 078, arXiv: 1402.7074 [hep-ph].

[127] G. C. Branco et al., *Theory and phenomenology of two-Higgs-doublet models*,
Phys. Rept. **516** (2012) 1, arXiv: 1106.0034 [hep-ph].

[128] ATLAS Collaboration, *Search for dark matter produced in association with a Higgs boson decaying to two bottom quarks in pp collisions at* $\sqrt{s} = 8$ *TeV with the ATLAS detector*,
Phys. Rev. D **93** (2016) 072007, arXiv: 1510.06218 [hep-ex].

[129] ATLAS Collaboration,
Luminosity determination in pp collisions at $\sqrt{s} = 8$ *TeV using the ATLAS detector at the LHC*,
Eur. Phys. J. C **76** (2016) 653, arXiv: 1608.03953 [hep-ex].

[130] ATLAS Collaboration, *The ATLAS Simulation Infrastructure*, Eur. Phys. J. C **70** (2010) 823,
arXiv: 1005.4568 [physics.ins-det].

[131] S. Agostinelli et al., *GEANT4: A simulation toolkit*, Nucl. Instrum. Meth. A **506** (2003) 250.

[132] ATLAS Collaboration,
The simulation principle and performance of the ATLAS fast calorimeter simulation FastCaloSim,
ATL-PHYS-PUB-2010-013, 2010, URL: https://cds.cern.ch/record/1300517.

[133] ATLAS Collaboration, *Proposal for particle-level object and observable definitions for use in physics measurements at the LHC*, ATL-PHYS-PUB-2015-013, 2015,
URL: https://cds.cern.ch/record/2022743.

[134] C. Degrande et al., *UFO - The Universal FeynRules Output*,
Comput. Phys. Commun. **183** (2012) 1201, arXiv: 1108.2040 [hep-ph].

[135] DM Forum repository, *DMV UFO model*, URL: https://svnweb.cern.ch/cern/wsvn/LHCDMF/trunk/models/Monojet_DMV/?#ae98247b340ee12c1e7b0139c2062d807.

[136] S. Alioli, P. Nason, C. Oleari, and E. Re, *A general framework for implementing NLO calculations in shower Monte Carlo programs: the POWHEG BOX*, JHEP **06** (2010) 043,
arXiv: 1002.2581 [hep-ph].

[137] T. Sjöstrand, S. Mrenna, and P. Z. Skands, *A brief introduction to PYTHIA 8.1*, Comput. Phys. Commun. **178** (2008) 852, arXiv: 0710.3820 [hep-ph].

[138] DMSimp Repository, *DMSimp UFO model*, URL: http://feynrules.irmp.ucl.ac.be/wiki/DMsimp.

[139] J. Alwall et al., *The automated computation of tree-level and next-to-leading order differential cross sections, and their matching to parton shower simulations*, JHEP **07** (2014) 079, arXiv: 1405.0301 [hep-ph].

[140] ATLAS Collaboration, *Search for New Phenomena in Dijet Angular Distributions in Proton–Proton Collisions at $\sqrt{s}$ = 8 TeV Measured with the ATLAS Detector*, Phys. Rev. Lett. **114** (2015) 221802, arXiv: 1504.00357 [hep-ex].

[141] ATLAS Collaboration, *Search for heavy particles decaying into top-quark pairs using lepton-plus-jets events in proton–proton collisions at $\sqrt{s}$ = 13 TeV with the ATLAS detector*, Eur. Phys. J. C **78** (2018) 565, arXiv: 1804.10823 [hep-ex].

[142] DM Forum repository, *Higgs_scalar UFO model*, URL: https://svnweb.cern.ch/cern/wsvn/LHCDMF/trunk/models/Higgs_scalar_UFO/.

[143] DM Forum repository, *Zp2HDM_UFO UFO model*, URL: https://svnweb.cern.ch/cern/wsvn/LHCDMF/trunk/models/EW_Higgs_2HDM/.

[144] DM Forum repository, *DMS_tloop UFO model*, URL: https://svnweb.cern.ch/cern/wsvn/LHCDMF/trunk/models/Monojet_DMS_tloop/.

[145] DM Forum repository, *DMScalarMed_loop UFO model*, URL: https://svnweb.cern.ch/cern/wsvn/LHCDMF/trunk/models/HF_S%2BPS/.

[146] DM Forum repository, *dmS_T UFO model*, URL: https://svnweb.cern.ch/cern/wsvn/LHCDMF/trunk/models/Monojet_tChannel/contributed_by_Amelia_Brennan/.

[147] DM Forum repository, *DM_Bflavored UFO model*, URL: https://svnweb.cern.ch/cern/wsvn/LHCDMF/trunk/models/HF_singleb/.

[148] DM Forum repository, *Pseudoscalar_2HDM UFO model*, URL: https://svnweb.cern.ch/cern/wsvn/LHCDMF/trunk/models/Pseudoscalar_2HDM/.

[149] ATLAS Collaboration, *Electron efficiency measurements with the ATLAS detector using 2012 LHC proton–proton collision data*, Eur. Phys. J. C **77** (2017) 195, arXiv: 1612.01456 [hep-ex].

[150] ATLAS Collaboration, *Electron efficiency measurements with the ATLAS detector using the 2015 LHC proton–proton collision data*, ATLAS-CONF-2016-024, 2016, URL: https://cds.cern.ch/record/2157687.

[151] ATLAS Collaboration, *Muon reconstruction performance of the ATLAS detector in proton–proton collision data at $\sqrt{s}$ = 13 TeV*, Eur. Phys. J. C **76** (2016) 292, arXiv: 1603.05598 [hep-ex].

[152] ATLAS Collaboration, *Measurement of the photon identification efficiencies with the ATLAS detector using LHC Run-1 data*, Eur. Phys. J. C **76** (2016) 666, arXiv: 1606.01813 [hep-ex].

[153] ATLAS Collaboration, *Topological cell clustering in the ATLAS calorimeters and its performance in LHC Run 1*, Eur. Phys. J. C **77** (2017) 490, arXiv: 1603.02934 [hep-ex].

[154] ATLAS Collaboration, *Properties of jets and inputs to jet reconstruction and calibration with the ATLAS detector using proton–proton collisions at $\sqrt{s}$ = 13 TeV*, ATL-PHYS-PUB-2015-036, 2015, URL: https://cds.cern.ch/record/2044564.

[155] ATLAS Collaboration,
Electron identification measurements in ATLAS using $\sqrt{s}$ = 13 TeV data with 50 ns bunch spacing,
ATL-PHYS-PUB-2015-041, 2015, URL: https://cds.cern.ch/record/2048202.

[156] ATLAS Collaboration,
Electron and photon energy calibration with the ATLAS detector using LHC Run 1 data,
Eur. Phys. J. C **74** (2014) 3071, arXiv: 1407.5063 [hep-ex].

[157] M. Cacciari, G. P. Salam, and G. Soyez, *The anti-k_t jet clustering algorithm*, JHEP **04** (2008) 063,
arXiv: 0802.1189 [hep-ph].

[158] M. Cacciari, G. P. Salam, and G. Soyez, *FastJet user manual*, Eur. Phys. J. C **72** (2012) 1896,
arXiv: 1111.6097 [hep-ph].

[159] ATLAS Collaboration, *Performance of b-jet identification in the ATLAS experiment*,
JINST **11** (2016) P04008, arXiv: 1512.01094 [hep-ex].

[160] ATLAS Collaboration, *Optimisation of the ATLAS b-tagging performance for the 2016 LHC Run*,
ATL-PHYS-PUB-2016-012, 2016, URL: https://cds.cern.ch/record/2160731.

[161] ATLAS Collaboration, *Performance of missing transverse momentum reconstruction with the ATLAS detector using proton–proton collisions at $\sqrt{s}$ = 13 TeV*, (2018),
arXiv: 1802.08168 [hep-ex].

[162] J. M. Lindert et al., *Precise predictions for V+jets dark matter backgrounds*, (2017),
arXiv: 1705.04664v1 [hep-ph].

[163] ATLAS Collaboration, *Search for invisible decays of a Higgs boson using vector-boson fusion in pp collisions at $\sqrt{s}$ = 8 TeV with the ATLAS detector*, JHEP **01** (2016) 172,
arXiv: 1508.07869 [hep-ex].

[164] ATLAS Collaboration, *Search for invisible Higgs boson decays in vector boson fusion at $\sqrt{s}$ = 13 TeV with the ATLAS detector*, (2018), arXiv: 1809.06682 [hep-ex].

[165] ATLAS Collaboration, *Search for new phenomena in dijet events using 37 fb^{-1} of pp collision data collected at $\sqrt{s}$ = 13 TeV with the ATLAS detector*, Phys. Rev. D **96** (2017) 052004,
arXiv: 1703.09127 [hep-ex].

[166] T. Aaltonen et al., *Global Search for New Physics with 2.0 fb^{-1} at CDF*,
Phys. Rev. D **79** (2009) 011101, arXiv: 0809.3781 [hep-ex].

[167] ATLAS Collaboration, *Search for new phenomena in the dijet mass distribution using pp collision data at $\sqrt{s}$ = 8 TeV with the ATLAS detector*, Phys. Rev. D **91** (2015) 052007,
arXiv: 1407.1376 [hep-ex].

[168] Z. Nagy, *Three jet cross-sections in hadron hadron collisions at next-to-leading order*,
Phys. Rev. Lett. **88** (2002) 122003, arXiv: hep-ph/0110315 [hep-ph].

[169] Z. Nagy, *Next-to-leading order calculation of three jet observables in hadron hadron collision*,
Phys. Rev. **D68** (2003) 094002, arXiv: hep-ph/0307268 [hep-ph].

[170] ATLAS Collaboration, *Search for low-mass dijet resonances using trigger-level jets with the ATLAS detector in pp collisions at $\sqrt{s}$ = 13 TeV*, (2018), arXiv: 1804.03496 [hep-ex].

[171] ATLAS Collaboration,
Search for new light resonances decaying to jet pairs and produced in association with a photon or a jet in proton–proton collisions at $\sqrt{s}$ = 13 TeV with the ATLAS detector,
ATLAS-CONF-2016-070, 2016, URL: https://cds.cern.ch/record/2206221.

[172] ATLAS Collaboration,
Search for light resonances decaying to boosted quark pairs and produced in association with a photon or a jet in proton–proton collisions at $\sqrt{s}$ = 13 TeV with the ATLAS detector, (2018), arXiv: 1801.08769 [hep-ex].

[173] J. Thaler and K. Van Tilburg, *Identifying Boosted Objects with N-subjettiness*, JHEP **03** (2011) 015, arXiv: 1011.2268 [hep-ph].

[174] ATLAS Collaboration, *Search for resonances in the mass distribution of jet pairs with one or two jets identified as b-jets in proton–proton collisions at $\sqrt{s}$ = 13 TeV with the ATLAS detector*, (2018), arXiv: 1805.09299 [hep-ex].

[175] ATLAS Collaboration, *Search for new high-mass phenomena in the dilepton final state using 36 fb^{-1} of proton–proton collision data at $\sqrt{s}$ = 13 TeV with the ATLAS detector*, JHEP **10** (2017) 182, arXiv: 1707.02424 [hep-ex].

[176] ATLAS Collaboration, *Search for new phenomena in a lepton plus high jet multiplicity final state with the ATLAS experiment using $\sqrt{s}$ = 13 TeV proton–proton collision data*, JHEP **09** (2017) 088, arXiv: 1704.08493 [hep-ex].

[177] J. Butterworth et al., *PDF4LHC recommendations for LHC Run II*, J. Phys. **G43** (2016) 023001, arXiv: 1510.03865 [hep-ph].

[178] A. L. Read, *Presentation of search results: the CL_S technique*, J. Phys. G **28** (2002) 2693.

[179] M. Backovic, A. Martini, K. Kong, O. Mattelaer, and G. Mohlabeng,
MadDM: New dark matter tool in the LHC era, AIP Conf. Proc. **1743** (2016) 060001, arXiv: 1509.03683 [hep-ph].

[180] F. Kahlhoefer, K. Schmidt-Hoberg, T. Schwetz, and S. Vogl,
Implications of unitarity and gauge invariance for simplified dark matter models, JHEP **02** (2016) 016, arXiv: 1510.02110 [hep-ph].

[181] ATLAS Collaboration, *Search for heavy Higgs bosons A/H decaying to a top quark pair in pp collisions at $\sqrt{s}$ = 8 TeV with the ATLAS detector*, Phys. Rev. Lett. **119** (2017) 191803, arXiv: 1707.06025 [hep-ex].

[182] A. Djouadi, M. Drees, and J.-L. Kneur,
Neutralino dark matter in mSUGRA: Reopening the light Higgs pole window, Phys. Lett. B **624** (2005) 60, arXiv: hep-ph/0504090 [hep-ph].

[183] E. A. Bagnaschi et al., *Supersymmetric Dark Matter after LHC Run 1*, Eur. Phys. J. **C75** (2015) 500, arXiv: 1508.01173 [hep-ph].

[184] L. E. Strigari, *Galactic Searches for Dark Matter*, Phys. Rept. **531** (2013) 1, arXiv: 1211.7090 [astro-ph.CO].

[185] LHCb Collaboration, *Search for Higgs-like bosons decaying into long-lived exotic particles*, Eur. Phys. J. C **76** (2016) 664, arXiv: 1609.03124 [hep-ex].

[186] LHCb Collaboration, *Search for Dark Photons Produced in 13 TeV pp Collisions*, Phys. Rev. Lett. **120** (2018) 061801, arXiv: 1710.02867 [hep-ex].

[187] A. A. Aguilar-Arevalo et al., *Dark Matter Search in Nucleon, Pion, and Electron Channels from a Proton Beam Dump with MiniBooNE*, (2018), arXiv: 1807.06137 [hep-ex].